

Influence of Ice Crystal Habit and Cirrus Spatial Inhomogeneities on the Retrieval of Cirrus Optical Thickness and Effective Radius

DISSERTATION

zur Erlangung des akademischen Grades

Doktor der Naturwissenschaften

(Dr. rer. nat)

Heike Kalesse

Johannes Gutenberg-Universität Mainz
Fachbereich 08 für Physik, Mathematik und Informatik

vorgelegt von

Heike Kalesse, geb. Eichler

geboren in Mühlhausen / Thüringen

Mainz, 16.12.2009

Summary

This PhD thesis investigates the influence of ice crystal habit and cirrus spatial inhomogeneities on the retrieval of cirrus optical thickness and effective ice particle radius. For this purpose airborne spectral solar radiation measurements as well as solar and thermal infrared radiative transfer simulations are conducted. Airborne spectral upwelling radiance data are obtained with the Spectral Modular Airborne Radiation measurement system (SMART-Albedometer) within the frame of the CIRrus CLOUD Experiment-2 (CIRCLE-2) in May 2007. Based on these radiance data a cloud retrieval algorithm is employed to derive cirrus optical thickness and particle effective radius from one-dimensional (1D) radiative transfer calculations. The influence of ice particle shape on retrieved properties is evaluated by variation of the ice particle single-scattering properties in the retrieval. Also, the impact of ice particle habit on cirrus radiative forcing is studied by radiative transfer simulations. The question of relative importance of cirrus spatial heterogeneity and ice particle shape is addressed via three-dimensional (3D) and independent pixel approximation (IPA) cirrus radiative transfer calculations. This analysis is based on an exemplarily model cloud generated from data collected during the National Aeronautics and Space Administration (NASA) Tropical Composition, Cloud, and Climate Coupling (TC⁴) experiment in summer 2007 in Costa Rica. For this specific case it is found that locally both - shape effects and 3D effects - can be of the same magnitude (up to about 40–60 % over- and underestimation of cirrus optical thickness and effective radius). However, on domain average, ice particle shape effects bias the retrievals more strongly than 3D effects.

Zusammenfassung

Diese Dissertation untersucht den Einfluss von Eiskristallform und räumlicher Inhomogenität von Zirren auf das Retrieval von optischer Wolkendicke und effektivem Eispartikelradius. Zu diesem Zweck werden flugzeuggetragene spektrale Messungen solarer Strahlung sowie solare und langwellige Strahlungstransfersimulationen durchgeführt. Flugzeuggetragene spektrale aufwärtsgerichtete Radianzen (Strahldichten) sind mit dem SMART-Albedometer (Spectral Modular Airborne Radiation measurement sysTem) während des CIRCLE-2 (CIRrus CLOUD Experiment-2) Feldexperiments im Mai 2007 gemessen worden. Basierend auf diesen Radianzdaten werden mittels eines Wolkenretrievalalgorithmus optische Wolkendicken und effektive Eispartikelradien anhand von eindimensionalen Strahlungstransferrechnungen bestimmt. Die Auswirkung der Annahme unterschiedlicher Eiskristallformen auf die retriervten Parameter wird durch Variation der Einfachstreueigenschaften der Eispartikel untersucht. Darüber hinaus wird mittels Strahlungstransferrechnungen auch der Einfluss der Eiskristallform auf den Strahlungsantrieb von Eiswolken ermittelt. Die Frage nach dem relativen Einfluss von räumlicher Wolkeninhomogenität und Eiskristallform wird anhand von dreidimensionalen und independent pixel approximation (IPA) Strahlungssimulationen untersucht. Die Analyse basiert auf einer Modelleiswolke, die aus Daten des NASA (National Aeronautics and Space Administration) TC⁴ (Tropical Composition, Cloud, and Climate Coupling) Feldexperiments im Sommer 2007 in Costa Rica erzeugt wurde. Lokal gesehen können beide Effekte - Eiskristallform und räumliche Eiswolkeninhomogenität - die gleiche Größenordnung haben und zu einer Unter- bzw. Überschätzung der retriervten Parameter um 40–60 % führen. Gemittelt über die ganze Wolke ist jedoch der Einfluss der Eiskristallform viel bedeutender als der von räumlichen Inhomogenitäten.

Contents

1	Introduction	1
1.1	Occurrence, Formation, and Properties of Cirrus	1
1.2	Influence of Cirrus on the Radiative Energy Budget	5
1.3	Remote Sensing of Cirrus	7
1.4	Objectives	10
2	Definitions	11
2.1	Radiative Quantities	11
2.2	Optical and Microphysical Cirrus Properties	13
2.2.1	Single-scattering Properties	14
2.2.2	Microphysical Properties	18
2.2.3	Volumetric Optical Properties	18
2.3	Radiative Transfer Equation	19
3	Experimental	21
3.1	The SMART-Albedometer	21
3.1.1	Setup	21
3.1.2	Radiometric Calibration	23
3.1.3	Measurement Uncertainties	27
3.2	The CIRCLE-2 Experiment	28
3.2.1	Overview	28
3.2.2	Radiation Measurements	30
3.2.3	Additional Instrumentation	31
3.2.4	Case Study of May 22, 2007	32
4	Retrieval Methodology	36
4.1	Radiative Transfer Model	36
4.1.1	Basic Model Input	36
4.1.2	Spectral Surface Albedo	37
4.1.3	Measured and Modelled Clear-Sky Radiance Spectra	38
4.1.4	Optical and Microphysical Cirrus Properties	38
4.2	Bispectral Reflectance Technique	41
5	Ice Crystal Shape Effects	46
5.1	Impact of Ice Crystal Habit on Retrieved Properties	46
5.1.1	Cirrus Optical Thickness	46
5.1.2	Ice Particle Effective Radius	49

5.1.3	Influence of Surface Albedo and Retrieval Mesh Density	51
5.1.4	Influence of Wavelengths Used in the Retrieval	51
5.2	Impact of Ice Crystal Habit on Cirrus Radiative Forcing	53
5.2.1	Solar Radiative Forcing	53
5.2.2	Thermal Infrared Radiative Forcing	59
5.2.3	Broadband Net Radiative Forcing	61
6	Cirrus Spatial Heterogeneity Versus Crystal Shape Effects	65
6.1	The TC ⁴ Experiment	65
6.1.1	Overview	65
6.1.2	Input Cloud Generation	66
6.2	Methodology	69
6.2.1	Strategy	69
6.2.2	Radiative Transfer Modelling and Cirrus Retrieval	71
6.2.3	Consistency Check	74
6.2.4	Uncertainties	74
6.3	Cloud Retrieval Results	75
6.3.1	3D Effects	75
6.3.2	Ice Particle Shape Effects	78
6.3.3	3D versus Shape Effects	82
7	Summary, Conclusions, and Outlook	86
7.1	Summary and Conclusions	86
7.1.1	Ice Particle Shape Effects	86
7.1.2	Relative Importance of Ice Particle Shape and 3D Cloud Structure . .	88
7.2	Outlook	89
7.2.1	Sensitivity Studies	89
7.2.2	Validation of Satellite Retrievals	90
7.2.3	Tandem Measurement Platform	90
	Bibliography	93
	List of Symbols	107
	List of Abbreviations	110
	List of Figures	112
	List of Tables	114
	Index	115
	Curriculum Vitae	115

1 Introduction

One of the most challenging problems of current climate research programs is in understanding the impact of clouds on the global radiation energy budget. In that context, so-called cloud retrievals have been developed to infer macro- and microphysical cloud properties from satellite data. In a presentation at the "GlobCloud Workshop" in March 2009 in Berlin, Ralf Bennartz (University of Wisconsin) ascertained that cirrus are still the big unknown in cloud retrievals because they consist of non-spherical ice crystals with a variety of shapes and sizes which make remote sensing and in situ characterization difficult. In addition, the effects of cirrus spatial inhomogeneities are ignored in current ice cloud retrievals. The objective of this work is to shed some light on these issues and to quantify the influence of ice crystal shape and cirrus spatial heterogeneity on cirrus remote sensing for specific case studies.

1.1 Occurrence, Formation, and Properties of Cirrus

As described by the morphological cloud classification of the World Meteorological Organisation (WMO) cirrus are clouds in the form of filaments, narrow bands, patches, or hooks that are composed of ice crystals (WMO, 1987). The International Satellite Cloud Climatology Project (ISCCP) that collects global cloud datasets with operational weather satellites defines cirrus as high-level clouds with cloud top pressures below 440 mb [i.e., above approximately 6 km altitude, (Rossow et al., 1996)]. However, the maximum altitude is modulated by the height of the tropopause thus leading to latitudinal cloud top height variations between 4–20 km (Dowling and Radke, 1990).

Global satellite observations show that cirrus clouds are not confined to a particular latitude or season but are globally widespread (e.g., Wylie et al., 1994; Jin et al., 1996; Sassen and Wang, 2008). The reported mean global cirrus cloud cover ranges between 13 % (Chen et al., 2000) and 27 % (Stubenrauch et al., 2006) with most recent studies stating 17 % (Sassen and Wang, 2008). Satellite climatologies of cloud cover show a minimum of cirrus over the polar latitudes, the subtropical high pressure belt, and marine stratiform clouds (Jin et al., 1996; Sassen and Wang, 2008). With values of 45 % the relative abundance of cirrus is highest in the Tropics (Stubenrauch et al., 2006). This large cirrus coverage is a result of anvils produced by deep convection in the Intertropical Convergence Zone (ITCZ) and in tropical regions associated with monsoons (Mace et al., 2006b). Cirrus in midlatitudes are mostly formed in connection with frontal and low-pressure systems and jet streams (Lynch et al., 2002). Thus significant cirrus cloud amounts are present in the midlatitude storm track regions. Mountain wave updraft is recognized as another cirrus formation mechanism. Additionally, cirrus can develop from the spreading of aircraft condensation trails (contrails) caused by air traffic in the upper troposphere (Schumann, 2005;

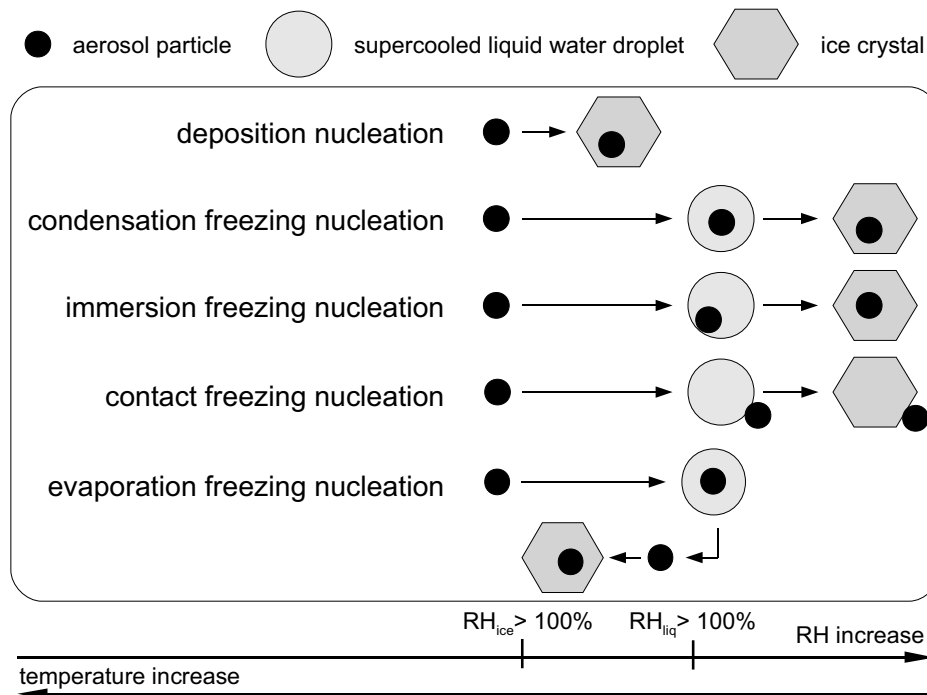


Figure 1.1: Schematic of heterogeneous ice nucleation processes. Directions of temperature and relative humidity (RH) increase as well as thresholds at which supersaturation with respect to solid ice and liquid water (liq) are indicated.

Stubenrauch and Schumann, 2005). Cirrus genesis is also caused by moisture supply from thunderstorms to the high and cold tropical tropopause leading to so-called cold-trap cirrus which is thin-to-subvisual (Winker and Trepte, 1998).

Ice particle formation in the troposphere is realized by two different processes: homogeneous or heterogeneous ice nucleation. The former process describes the spontaneous freezing of pure or highly diluted supercooled cloud droplets at temperatures below approximately -36°C – -40°C . At higher temperatures ice particle formation can only be triggered by the presence of aerosol particles acting as ice nuclei (heterogeneous ice nucleation). Besides these two primary ice particle formation mechanisms so-called secondary or ice multiplication processes will be described subsequently.

Liquid water can exist in the form of supercooled droplets down to temperatures of about -40°C (Pruppacher, 1995) where supersaturations (relative humidities $> 100\%$) with respect to ice are considerable (on the order of several 10 %, Koop et al. (2000)) thus providing conditions for the formation of stable ice clusters.

Homogeneous freezing point temperatures can be decreased by substances dissolved in the supercooled liquid water droplets (Hoffer, 1961). Heymsfield and Miloshevich (1995) report that homogeneous freezing does play a role in the formation of orographic wave cloud cirrus where very high supersaturations are reached due to strong vertical motions and high adiabatic temperature changes.

Heterogeneous freezing sets in at lower supersaturations and higher temperatures (Peter et al., 2006) and requires the availability of insoluble aerosol particles. Several path-

ways to heterogeneously form ice particles are known, they are illustrated in Figure 1.1. *Deposition nucleation* is a process in which water molecules from the gas phase directly deposit on existing ice nuclei provided that supersaturation with respect to ice is reached. The other processes only occur when saturation with respect to liquid water is exceeded (cf. Figure 1.1). During *condensation freezing nucleation* aerosol particles act as condensation nuclei for liquid water droplets which become supercooled droplets when temperatures fall below 0°C . If temperatures are sufficiently low, the aerosol particles (within the droplets) act as ice nuclei and trigger the freezing of the newly formed supercooled droplets. Aerosol particles that encounter existing supercooled droplets can be immersed in the droplets and can then act as ice nuclei. This mechanism is named *immersion freezing nucleation*. During *contact freezing nucleation* freezing is triggered by the collision of a supercooled droplet with an ice nucleus. It is a stochastic process which depends on the collision rate between aerosol particles and droplets which is high in downdrafts and entrainment zones (regions with evaporating drops). The *evaporation freezing nucleation* mechanism was discovered by Rosinski and Morgan (1991). They found that the residual aerosol particles left after the evaporation of droplets in decreasing relative humidity conditions can become ice nuclei. Under such conditions ice crystals are then formed instantaneously via deposition nucleation.

The described primary ice formation mechanisms can only insufficiently explain ice particle concentrations observed in natural cirrus (Meyers et al., 1992). Ice particle concentrations often exceed the concentrations of measured ice nuclei by orders of magnitude (e.g., Hobbs, 1969; Hobbs and Rangno, 1985). Processes that might explain this discrepancy include the so-called Hallett-Mossop process (Hallett and Mossop, 1974). It describes the splintering of ice crystals caused by freezing of supercooled droplets on the crystals. The mechanism was found to be restricted to temperatures between -3°C – -8°C , vertical velocities of at least 1.4 m s^{-1} , and the availability of large supercooled droplets (diameters $>23\text{ }\mu\text{m}$). Vardiman (1978) states that mechanical fracturing during crystal-crystal collision in clouds with sufficiently strong turbulence can also lead to the production of secondary ice crystals. These secondary ice formation processes strongly depend on cloud dynamics, turbulence increases the efficiency of these mechanisms. The so-called seeder-feeder mechanism (Rutledge and Hobbs, 1983) in contrast does not depend on strong turbulences. It describes the triggering of ice formation when ice particles from a high "seeder" cloud fall through a lower-level "feeder" cloud containing supercooled droplets.

Once ice particles are formed their growth can be realized in different ways. At a given temperature the water vapor pressure over a plane ice surface is smaller than over a plane water surface. Thus, water vapor saturation over ice is reached easier than over water. In cloud conditions with concurrent ice supersaturation and water subsaturation the water vapor evaporates from the supercooled liquid water droplets and deposits onto the ice crystals. This process is known as Wegener-Bergeron-Findeisen process (Wegener, 1911; Bergeron, 1935; Findeisen, 1938). Riming, the capturing of supercooled liquid water droplets by ice crystals which is followed by a freezing of the droplets onto the surface of the ice particles also leads to ice particle growth. However, this process is only effective in mixed-phase clouds (coexistence of cloud droplets and ice particles) with high droplet number concentrations (for example cumulonimbus). Existing ice crystals can also collide and then freeze onto each

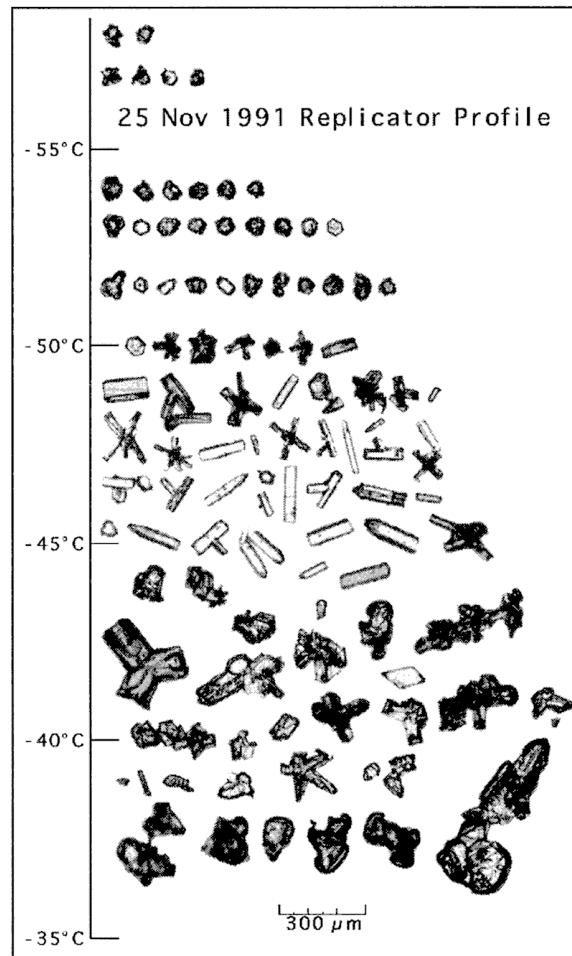


Figure 1.2: Vertical profile of ice particle size and shape. Figure is taken from Heymsfield and Miloshevich (2003). Data is based on balloon-borne replicator measurements in a cirrus on 25 Nov 1991, near Coffeyville, KS, during the NASA FIRE-II experiment.

other, a process known as aggregation. It depends on temperature, ice particle shape, and terminal velocity of the ice crystals. When ice particles growth to a certain size buoyancy and friction forces are not sufficient anymore so the ice crystals start to settle gravitationally (e.g., Heymsfield et al., 2002).

As emphasized by Sassen et al. (2008), cirrus properties depend on temperature, updraft strengths, and available supply of ice particle forming nuclei. Due to the complex formation phenomena (see above), there is a big natural variation of cirrus properties with regard to spatial extent and cloud structure, ice particle number concentrations, sizes and shapes (Dowling and Radke, 1990). Baran (2009) for example summarizes that ice crystal sizes in cirrus range from $\leq 10 \mu\text{m}$ to several thousand micrometers. Ice particle sizes in synoptically generated cirrus in midlatitudes range between approximately $10\text{--}4000 \mu\text{m}$ (Baran, 2009) but due to relatively low updraft velocities largest crystals are typically less than $1500 \mu\text{m}$ (Baum et al., 2005a). Due to growth processes and gravitational settling smallest crystals are observed at cloud top, largest towards cloud base (e.g., Francis et al., 1998; Gayet et al., 2004). In tropical cirrus associated with deep convection and strong updrafts, larger

crystals can exist at cloud top close to the convective core (Heymsfield and Miloshevich, 2003), particles up to centimeters in size are reported (Baum et al., 2005a). During cirrus anvil outflow these large crystals settle gravitationally so that at cloud top small crystals are observed (Garrett et al., 2003) and crystal sizes increase towards cloud base (Heymsfield and Miloshevich, 2003). In optically thin tropical cirrus small crystals of only a few micrometer in size are common (McFarquhar and Heymsfield, 1996). However, it is important to note that in situ measurements of ice particle sizes and number concentrations are technically difficult and a number of instrumental uncertainties exist, especially in the detection of small ice crystals (Gayet et al., 2002). In situ measurements are affected by shattering of the ice crystals on the microphysical probes which leads to an overestimation of the number concentration of small crystals (Heymsfield, 2007).

Not only does ice crystal size generally increase from cloud top to cloud base but also the complexity of ice crystal shape. This fact is illustrated in Figure 1.2 showing a profile of replicator images of cirrus ice particles. It was sampled in midlatitudes on 25 Nov, 1991, near Coffeyville, Kansas, USA during the National Aeronautics and Space Administration (NASA) First ISCCP Regional Experiment II (FIRE-II). Despite the large variability of observed crystal shapes which are influenced by dynamic and thermodynamic processes, some general findings can be summarized. At low temperatures and dynamically undisturbed regions at cirrus cloud tops small and pristine crystals in the form of hexagonal plates, bullets and bullet-rosettes are most common (e.g., Heymsfield and Platt, 1984; Heymsfield and Miloshevich, 2003). Under these conditions deposition nucleation is the dominant ice particle formation process. Hexagonal shapes are favored because such structures maximize attraction forces and minimize repellent forces. Ice crystals with a maximum dimension smaller than about $30\ \mu\text{m}$ are often of quasi-spherical shape (Korolev and Isaac, 2003). They are named droxtals (artificial word based on *droplet* and *crystal*). They are believed to form either when supercooled liquid droplets freeze so rapidly that hexagonal planes cannot build up or when hexagonally shaped ice crystals start to melt from the edge. In midlatitudinal cirrus, the most typical ice crystal shapes are bullet-rosettes and non-symmetric aggregates while hexagonal plates and columns are observed less frequently (Korolev et al., 2000; Gayet et al., 2004; Lawson et al., 2006). For tropical anvil cirrus, planar crystals, rosettes, and irregulars that sometimes build chain-like aggregates are reported (Baran, 2009). Here, turbulences lead to uncoordinated crystal growth.

With their long persistence of several hours after convection has ceased, high tropical cirrus clouds are of particular interest for further studies from a chemical, water-cycle and radiative energy budget point of view (Edwards et al., 2007). Sedimentation of ice crystals leads to a dehydration of the air and might thus explain the observed low relative humidities in the tropical stratosphere (e.g., Hartmann et al., 2001; Holton and Gettelman, 2001).

1.2 Influence of Cirrus on the Radiative Energy Budget

Cirrus are globally widespread and play an important role in the Earth-atmosphere system. They are linked to weather patterns often associated with precipitation and thereby modulate

the Earth's water budget (Sassen and Wang, 2008). More importantly, cirrus clouds have a strong effect on the Earth-atmosphere radiative energy balance (e.g., Liou, 1986; Cess et al., 1993) which is defined by the difference of incoming solar (wavelength range: 0.2–5 μm) and outgoing thermal infrared (IR; wavelength range: 5–100 μm) radiant flux densities. Cirrus influence the radiation energy budget by reflecting and absorbing solar radiation as well as by absorbing and emitting IR radiation (e.g., Liou, 1986; Chen et al., 2000; Lynch et al., 2002).

On the one hand, backscattering of solar radiation by cirrus reduces the amount of it reaching the Earth's surface and increases the amount that is reflected back to space. This results in a solar cooling of the surface and atmosphere below the cirrus. On the other hand, cirrus absorb thermal IR radiation emitted by the surface and lower (warmer) atmosphere and emit thermal IR radiation in upward and downward direction. Since cirrus are situated at high altitudes they emit at much lower temperatures than the surface. Consequently, thermal IR emission to space is reduced by cirrus which leads to an IR warming. The combined solar and thermal IR radiative effect of cirrus may either be warming or cooling, depending on the optical and microphysical properties of the ice cloud (Stephens et al., 1990; Zhang et al., 1999; McFarquhar et al., 2002).

Besides vertical position (temperature), ice water content (*IWC*), and ice crystal size (effective radius R_{eff}), the ice crystal shape is an important factor influencing the radiative properties of cirrus (e.g., Macke and Francis, 1998; Wyser, 1999; Wendisch et al., 2005, 2007). This owes to the fact that the single-scattering properties of non-spherical ice crystals may differ substantially from those of spheres (Kinne and Liou, 1989; Takano and Liou, 1989; Macke, 1993). In numerous field experiments (e.g., Heymsfield and Miloshevich, 2003; Garrett et al., 2003; Lawson et al., 2006; Schmitt and Heymsfield, 2007), a variety of ice crystal sizes and shapes ranging from pristine crystals to irregular aggregates were observed.

Contrarily, in numerical weather prediction models and global climate models (GCM) cirrus are often represented by a fixed ice particle shape (mostly hexagonal prisms) and a size (R_{eff}) that is dependent on cirrus temperature or *IWC* (Garrett et al., 2003). Until recently, ice crystals were even treated as spherical particles with a fixed size of $R_{\text{eff}} = 30 \mu\text{m}$ (Edwards et al., 2007). However, it is known that accurate representation of the single-scattering properties of ice crystals in GCM is of great importance in order to reduce some of the uncertainties in climate predictions as highlighted by Baran (2009). Over recent years, progress in parameterizing the scattering behaviour of ice crystals in GCM has been made (e.g., Kristjansson et al., 2000; Edwards et al., 2007) and first attempts to use an ensemble of ice crystal shapes are made. Lately, it was realized that in order to properly describe cirrus solar radiative transfer it is necessary to seek models which are not only able to predict the scattering properties of cirrus but also its bulk macrophysical properties (Baran and Labonnote, 2007).

1.3 Remote Sensing of Cirrus

To improve the parameterizations of cirrus in GCM, continuous global space-based measurements of cirrus are of great value. Over the past decades, a significant amount of work has been accomplished both in understanding the physics of ice clouds and in estimating global distributions of ice cloud properties from satellite-based instruments (Cooper et al., 2006). Since April 2006, a suite of Earth-orbiting satellites - the so-called A-train (Stephens and Vane, 2007) - is collecting a variety of cloud information with very high temporal resolution. The A-train combines active radio detection and ranging (radar) and light detection and ranging (lidar) systems with passive radiometric measurements and is used to produce global cirrus coverage maps (Sassen and Wang, 2008) and climatologies of cirrus properties (Hong et al., 2007).

With extending capabilities of space- or ground-based remote sensing measurements, various algorithms to study (cirrus) cloud characteristics were introduced. An overview of these active and passive cloud remote sensing retrieval algorithms is given in (Comstock et al., 2007) and (Stephens and Kummerow, 2007). However, extracting information about cirrus from satellite data is difficult because of variations in background, similarities to other cloud types, and the fact that cirrus are often semitransparent (Lynch et al., 2002; Davis et al., 2009). Depending on the physical processes involved, remote sensing retrieval algorithms are grouped into three classes: scattering, emission, and transmission techniques. The former method makes use of the wavelength-dependent reflectance of solar radiation by cloud particles and is thus limited to daytime application. The second technique is applicable to night- and day conditions because it is based on radiation emitted by clouds in the thermal IR and/or microwave wavelength range. The transmission approach is based on the attenuation of a defined source of radiation (as for example the sun). In addition, the use of active systems such as lidar and radar is becoming more sophisticated and enables to gain information on vertical cloud structure.

Parameters that can be derived from remote sensing methods include areal coverage, cloud top and -base temperature and altitude, liquid/ice water content (LWC/IWC), as well as cloud optical thickness (τ) and cloud particle effective radius (R_{eff}) (Lynch et al., 2002). τ determines how much incident solar radiation is transmitted through the cloud and reflected back to space whereas R_{eff} can be understood as mean particle size for characterizing a cloud particle number size distribution in radiative transfer calculations. Errors made when determining cloud parameters from remote sensing are two-fold. As emphasized by Cooper et al. (2006); Stephens and Kummerow (2007), the uncertainties result from both the measurements themselves and from the forward model assumptions used in relating observational and retrieval space.

Cirrus cloud remote sensing is more complicated compared to the retrieval of microphysical properties of liquid water clouds not only because of the different genesis and resulting different spatial distribution and dimensions of ice clouds, but also because they consist of ice crystals that are difficult to characterize (in situ or via remote sensing) and to parameterize in radiative transfer calculations. The various crystal habits that occur in cirrus add a degree of freedom to the retrievals. For this reason, a-priori assumptions about the single-scattering

properties of ensembles of ice crystals are made in most operational cirrus retrievals. A similar, long-standing difficulty in liquid water and ice cloud remote sensing are spatial cloud heterogeneities over various scales. As yet, no practical solution has been proposed to resolve this issue, partly because these effects are so multi-faceted that there is no reasonable way to correct for them with a single method.

The classical scattering retrieval technique to derive cloud optical thickness (τ) and effective radius (R_{eff}) of liquid water clouds was introduced by Twomey and Seton (1980) and Nakajima and King (1990). Later, it has been adapted to cirrus retrievals (Ou et al., 1993). The retrieval is based on measured cloud top reflectance (r_c) in two different wavelength ranges; one in the visible to very near-infrared (450–1000 nm), where ice is practically non-absorbing, and one in the near-infrared range (1500–2100 nm) where ice crystals (and liquid water) absorb solar radiation. Reflectance at the non-absorbing wavelength depends on cirrus τ . Reflectance at the near-infrared wavelength provides information on particle size R_{eff} . With radiative transfer calculations at both wavelengths reflectance values are pre-calculated for a number of pairs of τ and R_{eff} , and observed reflectance values are matched with these lookup tables (LUT). In liquid water clouds, the two-dimensional reflectance space spanned by τ and R_{eff} can be determined with radiative transfer modelling in which the single-scattering properties are determined by Mie theory because their constituents are spherical.

For cirrus, in contrast, the retrieved microphysical products based on remote sensing measurements depend on the assumption of ice crystal shape (Nasiri et al., 2002). Different crystal shapes exhibit different optical properties as a function of size, and wavelength. Modelled single-scattering properties (cf. Section 2.2.1) of non-spherical ice crystals are very diverse, (e.g., Takano and Liou, 1989; Macke, 1993) and result in substantially different lookup tables (Eichler et al., 2009). For example, the operational ice cloud procedures used for the Moderate Resolution Imaging Spectroradiometer (MODIS, Platnick et al. (2003)) Collection-5 retrievals (King et al., 2006) were based on a different set of ice crystal optical properties (Baum et al., 2005b) than those for Collection-4. This change caused significant differences in the retrieved crystal effective radius of up to three μm (Yang et al., 2007).

Although progress in microphysical retrieval algorithms is reported, difficulties in the retrieval of ice crystal shape and size distribution are ascertained especially for optically thin cirrus (Comstock et al., 2007). The effect of ice crystal surface roughness and inhomogeneities such as inclusions of air bubbles within the ice crystals on retrieval results were discussed by Labonnote et al. (2000) and Yang et al. (2008). Yang et al. (2008) reported that the dominant effect of surface roughness on cloud property retrievals is to decrease the retrieved τ and to increase the retrieved R_{eff} compared with their counterparts in the case of smooth ice particles. To complicate matters further, the ice crystal orientation has an influence on the radiative properties of cirrus (Klotzsche and Macke, 2006). Evoked by the significant shape effects, methods were devised to detect ice crystal habit from imaging radiometer data (McFarlane et al., 2005). Multiangle satellite measurements of cloud top reflectance (Chepfer et al., 2002) as well as polarized bidirectional radiances in the visible wavelength range (Chepfer et al., 2001) can be used to infer ice particle shape.

The question of the influence of ice crystal shape on the remote sensing of τ and R_{eff}

was addressed in several previous studies (e.g., Francis et al., 1998; McFarlane et al., 2005; McFarlane and Marchand, 2008). Francis et al. (1998) presented retrieval results from airborne measurements for five cirrus cases over a water surface and compared them with in situ measurements. Retrieved R_{eff} and τ depended strongly on assumed particle habit, differences in retrieval results of up to 60 % were found. The assumption of plates and spheres gave highest τ and smallest R_{eff} . Polycrystals were found to give the most consistent agreement with the in situ measurements. The work of McFarlane et al. (2005) focuses on the retrieval of cloud phase and dominant crystal habit. Seven crystal habits (hexagonal plates, solid and hollow columns, rough and smooth aggregates, spatial and planar rosettes) as well as spherical liquid water droplets were considered. The introduced shape retrieval is based on differences in the scattering phase function (cf. Section 2.2.1) of various particle shapes as a function of scattering angle observed under the nine viewing angles of the Multiangle Imaging Spectroradiometer (MISR) onboard the Terra satellite. This study refers to two cirrus cases observed over land. Depending on the assumed crystal shape, retrieved τ and R_{eff} differed by up to 50 % and 30 %, respectively. In McFarlane and Marchand (2008), statistics of retrieved cloud phase and ice crystal habit based on the algorithm introduced in McFarlane et al. (2005) are presented for a dataset of five years collected at the Atmospheric Radiation Measurement (ARM) Program’s Southern Great Plains (SGP) site. Strongest differences were found between the assumptions of rough aggregates and plates. Statistical analysis showed that 50 % of the cirrus were classified as consisting of mostly rough aggregates.

Further complication in the retrieval of τ and R_{eff} is introduced by horizontal heterogeneities in the microphysical cloud properties. The "cloud albedo-bias" which is discussed mainly for liquid water clouds (e.g., Cahalan et al., 1994; Barker, 1996; Carlin et al., 2002; Oreopoulos et al., 2007), for example, is due to the non-linear convex (concave) dependence of cloud top reflectance in the non-absorbing (absorbing) wavelength on cloud τ (R_{eff}). It causes a systematic underestimation of τ or R_{eff} if cloud variability is not resolved within a pixel (e.g., Marshak et al., 2006). Increasing imager resolution can only partly remedy the problem: In the standard lookup table technique, the individual pixels are implicitly assumed to be independent of each other (independent pixel approximation, IPA). However, with increasing resolution, this assumption does not hold true because pixel-to-pixel horizontal transport of photons becomes important. This effect leads to so-called radiative smoothing or roughening. Smoothing was first discovered in the Landsat satellite scale break (200 m were reported in a study by Cahalan and Snider (1989)). It leads to a suppression of variability on small scales. The characteristic length of horizontal photon transport in a cloud depends on τ and cloud geometrical thickness (Marshak et al., 1995). Less well-known is the fact that horizontal photon displacement is wavelength-dependent (Platnick, 2001; Kassianov and Kogan, 2002). Photons that incur even weak absorption have considerably shorter horizontal path lengths. Apart from radiative smoothing, roughening is observed for special Sun-cloud geometries. For example, near-horizon Sun angles in conjunction with high cloud top variability lead to an increase in illumination contrasts and may cause overestimation of τ or R_{eff} (Marshak et al., 2006). Since the cloud albedo bias decreases with resolution while horizontal photon transport and illumination effects (smoothing and roughening) increase, it is generally assumed that optimum spatial resolution is at around 1 km (Zinner and Mayer (2006), based on measured boundary-layer clouds). Vertical cloud struc-

ture is of special importance for R_{eff} retrievals Platnick (2000). Multi-layer clouds can be detected with spectral imagery (Wind et al., 2009) but remain a challenge because they enhance cloud horizontal variability effects considerably.

1.4 Objectives

This work concentrates on two issues that complicate the reflectance-based retrieval of τ and R_{eff} , the ice particle shape effect and the influence of cirrus spatial inhomogeneities.

In contrast to the publications by Francis et al. (1998); McFarlane et al. (2005); and McFarlane and Marchand (2008), the first part of this work will present τ and R_{eff} over two different surface types - land and open water. Data are based on airborne upwelling spectral radiance measurements collected with the Spectral Modular Airborne Radiation measurement sysTem (SMART)-Albedometer during the CIRrus CLoud Experiment-2 (CIRCLE-2). The influence of the assumed ice particle shape on the retrieved values of τ and R_{eff} for two case studies will be quantified. For that purpose, the parameterizations of bulk ice cloud optical properties for seven individual crystal habits (hexagonal plates, solid and hollow columns, rough aggregates, spatial and planar rosettes, and ice spheres) as well as for a mixture of particle habits will be used in the retrieval.

It is known that neglecting either cirrus spatial variability or crystal shape leads to biases in remote sensing products. However, their relative importance under different cloud conditions has not been studied systematically so far. It is unknown which effects dominate the error in standard cirrus retrievals, and which cloud parameters (τ , R_{eff} , cloud variability) determine the relative contributions. Such an assessment is the objective of the second part of this study. Data from a specific cloud case from the NASA Tropical Composition, Cloud, and Climate Coupling (TC⁴) experiment (Toon et al., 2009) was used to examine the impact of cirrus spatial variability and ice crystal single-scattering properties in heterogeneous cirrus clouds on remote sensing products (τ and R_{eff}).

The outline of this thesis is as follows: In Chapter 2 the terminology used in this work is explained. After introducing the working principle and the calibration methods of the SMART-Albedometer, an overview of the measurements made at the CIRCLE-2 field experiment is given in Chapter 3. In Chapter 4, the used radiative transfer model as well as the bispectral reflectance technique used to determine cirrus properties is described. The impact of ice particle shape assumption on the cirrus retrieval results for two CIRCLE-2 case studies is presented in Chapter 5. Additionally, the influence of ice crystal habit on the cirrus radiative forcing of these two case studies is analyzed in Chapter 5. The relative importance of ice crystal shape and 3D effects of spatially inhomogeneous cirrus on the remote sensing of τ and R_{eff} is addressed in Chapter 6. The thesis finishes with a summary, conclusions and outlook in Chapter 7.

2 Definitions

This chapter introduces the terminology used in this thesis. The subsequent definitions follow the explanations of several textbooks on the topic such as Bohren and Clothiaux (2006) and Petty (2006).

2.1 Radiative Quantities

The radiant energy flux Φ (in units of W) is the energy of electromagnetic (EM) radiation E_{rad} (in units of W s) emitted or received per unit time dt :

$$\Phi = \frac{dE_{\text{rad}}}{dt}. \quad (2.1)$$

Based on Φ , radiance and irradiance - the two major radiative quantities to measure quantitatively the strength of the EM radiation field - are derived.

The radiant energy flux density or **irradiance** F (in units of W m^{-2}) is a measure of radiant energy flux incident on a plane surface with unit area dA and orientation \vec{n} :

$$F = \frac{d\Phi}{dA}. \quad (2.2)$$

The orientation of the reference plane can be random but for describing radiative transfer in the atmosphere it is considered to be horizontal (cf. Figure 2.1). F is weighted with the cosine of the angle of incidence θ (zenith angle) on the horizontal surface with $\theta = 0^\circ$ referring to perpendicular incidence.

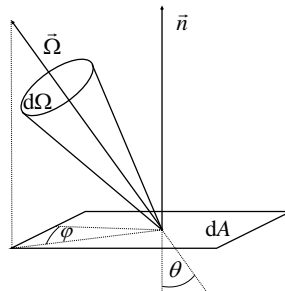


Figure 2.1: Geometry to define radiance and irradiance.

While F describes Φ propagating through a plane unit surface from all possible directions of a hemisphere, the **radiance** I (in units of $\text{W m}^{-2} \text{sr}^{-1}$) refers to a certain direction. $I(\vec{\Omega})$ is defined as radiant energy flux Φ transported through a plane unit area dA within the solid angle element $d\Omega$ centered around the direction of propagation of the EM radiation $\vec{\Omega}$ (cf. Figure 2.1):

$$I(\vec{\Omega}) = \frac{d^2\Phi}{\cos\theta dA d\Omega}. \quad (2.3)$$

The solid angle element $d\Omega$ is expressed in terms of the two directional angles θ (zenith angle) and φ (azimuth angle) and defined as $d\Omega = \sin\theta d\theta d\varphi$ (in units of sr).

On the basis of Eqs. 2.2 and 2.3, the integration of $I(\vec{\Omega})$ over $d\Omega$ yields F :

$$F = \iint_{4\pi \text{ sr}} I(\vec{\Omega}) \cdot \cos\theta d\Omega = \int_0^{2\pi} \int_0^\pi I(\theta, \varphi) \cdot \cos\theta \cdot \sin\theta d\theta d\varphi. \quad (2.4)$$

Separate consideration of the lower ($\theta = (\pi/2 \dots \pi)$ rad, $\varphi = (0 \dots 2\pi)$ rad) and upper hemisphere ($\theta = (0 \dots \pi/2)$ rad, $\varphi = (0 \dots 2\pi)$ rad) which are divided by the horizontally oriented surface, leads to upwelling (\uparrow) and downwelling (\downarrow) irradiance components defined as:

$$F^\downarrow = + \int_0^{2\pi} \int_0^{\pi/2} I(\theta, \varphi) \cdot \cos\theta \cdot \sin\theta d\theta d\varphi \quad (2.5)$$

$$F^\uparrow = - \int_0^{2\pi} \int_{\pi/2}^\pi I(\theta, \varphi) \cdot \cos\theta \cdot \sin\theta d\theta d\varphi. \quad (2.6)$$

As shown in Eqs. 2.5 and 2.6, radiance determines irradiance. In the case of an isotropic field of radiation radiance is independent of direction ($I(\vec{\Omega}) = I_{\text{iso}}$) and it follows that

$$F_{\text{iso}}^\downarrow = F_{\text{iso}}^\uparrow = I_{\text{iso}} \cdot \pi \text{ sr}. \quad (2.7)$$

The downwelling irradiance F^\downarrow propagating through the atmosphere consists of a direct ($F_{\text{dir}}^\downarrow$) and an indirect component ($F_{\text{diff}}^\downarrow$):

$$F^\downarrow = F_{\text{dir}}^\downarrow + F_{\text{diff}}^\downarrow \quad (2.8)$$

$F_{\text{dir}}^\downarrow$ refers to the solar radiation which has not encountered scattering processes in the atmosphere yet. $F_{\text{diff}}^\downarrow$ describes the part of the radiation which has been scattered/absorbed/emitted by atmospheric molecules and particles or was reflected from the surface back into the atmosphere. The upwelling irradiance is diffuse only: $F^\uparrow \equiv F_{\text{diff}}^\uparrow$.

The **actinic flux density** F_{act} is defined as unweighted integral of radiance over solid angle and represents the energy flux on a unit sphere. It is important for photochemical studies where it is used to estimate the radiant energy that can be absorbed by an air molecule.

$$F_{\text{act}} = \int_0^{2\pi} \int_0^\pi I(\theta, \varphi) \cdot \sin \theta \, d\theta \, d\varphi. \quad (2.9)$$

Irradiance is the relevant quantity for radiative energy budget calculations. The difference between down- and upwelling irradiances are called **net** irradiances. The **radiative forcing** ΔF of clouds at a certain altitude z is defined as the difference of the net irradiances in the presence of clouds (index "cloudy") and clear sky conditions (index "clear"):

$$\Delta F(z) = \left[F^\downarrow(z) - F^\uparrow(z) \right]_{\text{cloudy}} - \left[F^\downarrow(z) - F^\uparrow(z) \right]_{\text{clear}} \quad (2.10)$$

ΔF can be positive or negative. The former implies a warming (energy gain) of the surface and atmosphere below the altitude z , the latter a cooling (energy loss). ΔF is mostly considered separately for the solar (ΔF^{sol}) and thermal infrared (ΔF^{IR}) spectral ranges. The sum of both is called **net** radiative forcing ΔF^{net} .

Relating the radiative quantities to an infinitesimal wavelength interval $[\lambda, \lambda + d\lambda]$, results in spectral quantities such as spectral radiances $I_\lambda(\vec{\Omega})$ ($\text{W m}^{-2} \text{sr}^{-1} \text{nm}^{-1}$) and spectral irradiances F_λ ($\text{W m}^{-2} \text{nm}^{-1}$). By integrating the spectral quantities over a wavelength interval, broadband quantities are obtained. The following definitions are valid for both broadband or spectral quantities.

The **reflectance** r and the **albedo** ρ at a certain altitude z are defined as

$$r(z) = \frac{I^\uparrow(z)}{F^\downarrow(z)} \cdot \pi \text{ sr} \quad (2.11)$$

$$\rho(z) = \frac{F^\uparrow(z)}{F^\downarrow(z)} \quad (2.12)$$

respectively, with $I^\uparrow(z)$ denoting the upwelling radiance in nadir direction ($\theta = \pi$ rad). In the case of an isotropic radiation field, $r(z)$ and $\rho(z)$ are identical (cf. Eq.2.7). While values of r can be larger than 1, values of ρ range between 0 and 1 to ensure the conservation of radiant energy. Subsequently, **cloud top reflectances** r_c will be of importance. They are defined for $z \geq z_{\text{top}}$ with z_{top} being the cloud top. The **surface albedo** $\rho_{\text{surf}} = \rho(z = 0)$ describes how much of the incident irradiance is reflected by the surface with the extremes of 0 and 1 referring to no reflection and total reflection, respectively. The amount that is not reflected ($1 - \rho_{\text{surf}}$) is absorbed by the surface. The surface albedo strongly depends on surface type (*e.g.* land/sea) and wavelength.

2.2 Optical and Microphysical Cirrus Properties

EM radiation propagating through the atmosphere is absorbed/scattered/emitted by gas molecules, aerosol particles, and cloud particles. In the case of liquid water clouds, the cloud

particles are spherical droplets, in ice clouds - which this work focuses on - nonspherical ice crystals are present. The interactions between EM radiation and individual particles in the atmosphere are described by three single-scattering properties: the extinction cross section C_{ext} , the single-scattering albedo $\tilde{\omega}$, and the scattering phase function \mathcal{P} . These properties depend on the cross-section area, and surface or volume, the refractive index, and also on the shape and orientation of individual crystals.

2.2.1 Single-scattering Properties

The **extinction cross section** C_{ext} (m^2) is a measure of how much radiation that incidences on an ice crystal is extinguished, either due to scattering or absorption. It is defined as sum of the scattering cross section C_{sca} (m^2) and the absorption cross section C_{abs} (m^2):

$$C_{\text{ext}} = C_{\text{sca}} + C_{\text{abs}}. \quad (2.13)$$

The dimensionless **single-scattering albedo** $\tilde{\omega}$ is defined as relative measure of scattering versus absorption:

$$\tilde{\omega} = \frac{C_{\text{sca}}}{C_{\text{ext}}} = \frac{C_{\text{sca}}}{C_{\text{sca}} + C_{\text{abs}}}, \quad (2.14)$$

and ranges from 0 for a purely absorbing ice crystal to 1 for a purely scattering ice crystal, respectively. It is related to the imaginary part of the refractive index \tilde{n}_i of ice, a wavelength-dependent optical constant which is also a measure of absorption. Both spectral quantities are shown as function of wavelength in Figure 2.2. The spectral pattern of \tilde{n}_i between $\lambda = 450\text{--}2200$ nm (cf. Figure 2.2a) reveals that ice is almost non-absorbing for $\lambda < 1400$ nm and exhibits two absorption maxima around 1500 nm and 2000 nm. These spectral features cause the characteristic pattern of $\tilde{\omega}$ shown in Figure 2.2b. This plot also clearly illustrates that $\tilde{\omega}$ increases with increasing ice crystal size (R_{eff} , explained subsequently, cf. Eq. 2.25). Moreover, it strongly depends on ice crystal shape. Hexagonal plates with twice the R_{eff} of solid columns have the same $\tilde{\omega}$.

The dimensionless **scattering phase function** $\mathcal{P}(\vartheta, \varphi)$ describes the probability that photons which are incident on an ice crystal are scattered in particular directions which differ from the direction of incidence by the scattering angle ϑ . φ denotes the azimuth angle. The integral of $\mathcal{P}(\vartheta, \varphi)$ over all solid angles is required to satisfy the normalization condition:

$$\iint_{4\pi \text{ sr}} \mathcal{P}(\vartheta, \varphi) \, \text{d}\Omega = \int_0^{2\pi} \int_0^\pi \mathcal{P}(\vartheta, \varphi) \sin \vartheta \, \text{d}\vartheta \, \text{d}\varphi = 4\pi \text{ sr}. \quad (2.15)$$

For randomly oriented ice crystals, the azimuthal dependence vanishes, so that the scattering phase function is only a function of scattering angle and can be expressed as $\mathcal{P}(\cos \vartheta)$. It is used in the definition of the **asymmetry parameter** g , which is the mean cosine of the scattering angle:

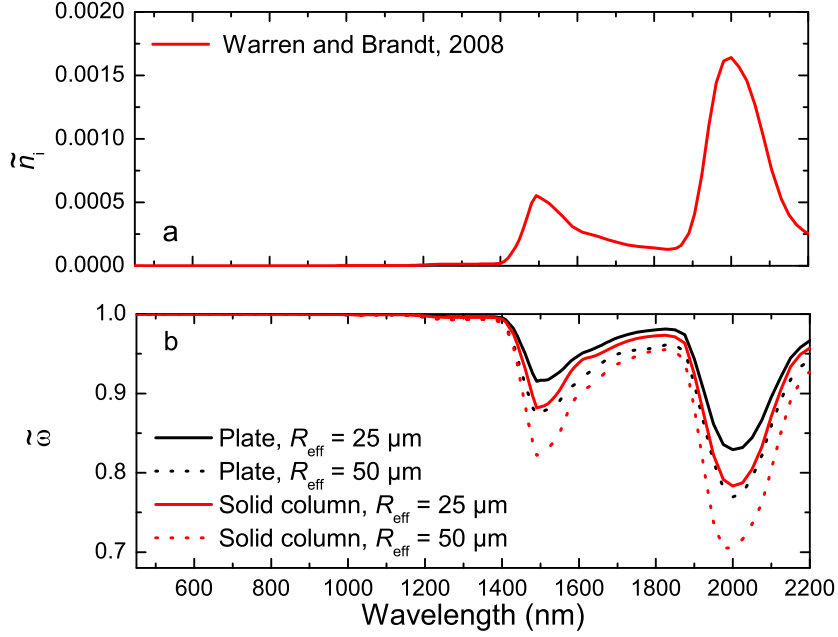


Figure 2.2: a) Imaginary part of the spectral refractive index of ice (\tilde{n}_i) and b) spectral single-scattering albedo $\tilde{\omega}$ for ice crystals with different habit and different effective radius R_{eff} .

$$g := \langle \cos \vartheta \rangle = \frac{1}{4\pi \text{ sr}} \iint_{4\pi \text{ sr}} \mathcal{P}(\vartheta) \cdot \cos \vartheta \, d\Omega = \frac{1}{2} \int_{-1}^{+1} \cos \vartheta \cdot \mathcal{P}(\cos \vartheta) \, d \cos \vartheta. \quad (2.16)$$

g is a measure of the anisotropy of the scattering phase function and ranges between -1 (total backward scattering) and +1 (total forward scattering). $g=0$ describes equal scattering in the forward and backward hemisphere.

As illustrated in Figure 2.3, $\mathcal{P}(\vartheta)$ is a function of ice crystal habit. $\mathcal{P}(\vartheta)$ of pristine ice crystals exhibit a strong forward scattering peak near $\vartheta = 0^\circ$. Plates exhibit the strongest forward scattering peak, rough aggregates the smoothest $\mathcal{P}(\vartheta)$. In comparison to spherical liquid water droplets (not shown), ice crystals have enhanced sideward and backward scattering. In addition, halo structures at $\vartheta = 22^\circ$ and 46° are a characteristic feature of $\mathcal{P}(\vartheta)$.

$\mathcal{P}(\cos \vartheta)$ of ice crystals is very asymmetric and thus cannot be expressed analytically. Different approximations for $\mathcal{P}(\cos \vartheta)$ exist. Depending on the required accuracy in the representation of $\mathcal{P}(\cos \vartheta)$, often either a series of Legendre polynomials or a (double) Henyey-Greenstein function is used as approximation.

Expanding $\mathcal{P}(\cos \vartheta)$ into an infinite series of dimensionless Legendre polynomials yields:

$$\mathcal{P}(\cos \vartheta) = \sum_{n=0}^{\infty} b_n \cdot P_n(\cos \vartheta). \quad (2.17)$$

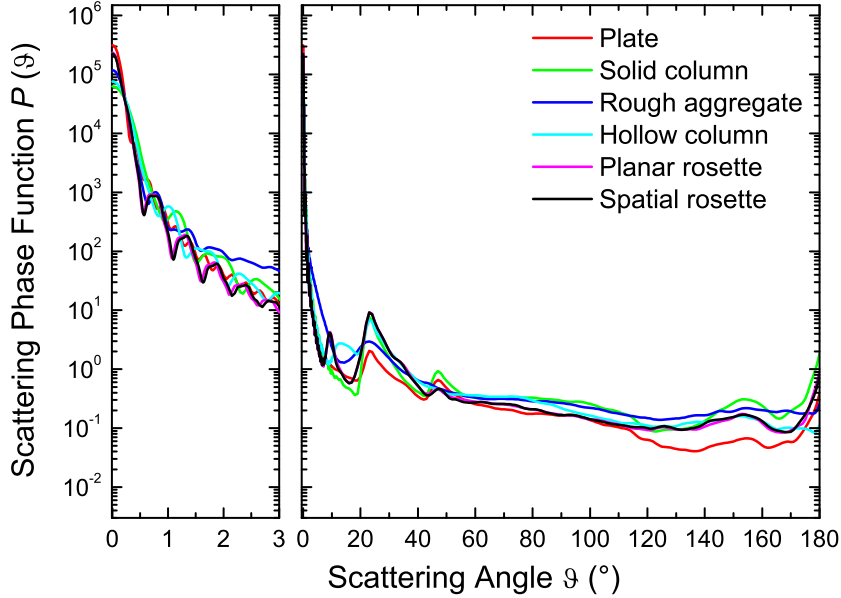


Figure 2.3: Scattering phase function $\mathcal{P}(\vartheta)$ of different ice crystals habits with an effective radius of $25\ \mu\text{m}$ at $670\ \text{nm}$ wavelength. The left hand panel is a close-up for the scattering angles $\vartheta = 0\text{--}3^\circ$ showing the forward scattering peak.

The Legendre polynomials $P_n(\cos \vartheta)$ are orthogonal basis functions defined by:

$$P_n(\cos \vartheta) = \frac{1}{2^n n!} \frac{d^n}{d \cos^n \vartheta} (\cos^2 \vartheta - 1)^n, \quad (2.18)$$

and the dimensionless coefficients b_n represent the contribution of each Legendre polynomial to the Legendre expansion. They are derived from

$$b_n = \frac{2n+1}{2} \int_{-1}^{+1} \mathcal{P}(\cos \vartheta) \cdot P_n(\cos \vartheta) d \cos \vartheta. \quad (2.19)$$

In practice, only a finite number Λ of Legendre polynomials is used in the expansion. The value of Λ is chosen based on the required accuracy of the features of $\mathcal{P}(\cos \vartheta)$. The computing time needed for the calculation of the Legendre coefficients is a limiting factor for Λ .

Another option to approximate $\mathcal{P}(\cos \vartheta)$ is via the Henyey-Greenstein (HG) scattering phase function which is based on the asymmetry parameter g and defined as:

$$\mathcal{P}_{\text{HG}}(\cos \vartheta) = \frac{1 - g^2}{(1 + g^2 - 2 \cdot g \cdot \cos \vartheta)^{3/2}}. \quad (2.20)$$

For $g > 0$, $\mathcal{P}_{\text{HG}}(\cos \vartheta)$ reproduces the forward scattering peak reasonably well but it does not capture backscattering properly. A way to remedy this problem is by using the double Henyey-Greenstein function:

$$\mathcal{P}_{\text{dHG}}(\cos \vartheta) = f \cdot \mathcal{P}_{\text{HG}}(\cos \vartheta; g_1) + (1 - f) \cdot \mathcal{P}_{\text{HG}}(\cos \vartheta; g_2), \quad (2.21)$$

g_1 and g_2 represent forward and backward peaks, respectively ($g_1 > 0$, $g_2 < 0$). Here, g_1 is the same as g in Eq. 2.20 and f is a fractional value between [0,1].

$\mathcal{P}_{\text{dHG}}(\cos \vartheta)$ captures the asymmetry of real phase functions well but not the higher order features such as halos. As reported by Fu and Takano (1994), the differences between $\mathcal{P}_{\text{dHG}}(\cos \vartheta)$ and $\mathcal{P}(\cos \vartheta)$ of real ice particles are a function of cloud optical thickness and solar zenith angle.

In atmospheric applications, the forward scattering peak around $\vartheta = 0^\circ$ is often considered as being unscattered and thus added to the direct (transmitted) radiation, a method referred to as *truncation* approximation (Potter, 1970). It is used to optimize the computational effort needed for an appropriate representation of $\mathcal{P}(\cos \vartheta)$ because it reduces the number of required Legendre coefficients Λ . When truncating the numerical expansion of $\mathcal{P}(\cos \vartheta)$ at Λ , Eq. 2.17 yields:

$$\mathcal{P}(\cos \vartheta) = \sum_{n=0}^{\Lambda-1} b_n \cdot P_n(\cos \vartheta). \quad (2.22)$$

Truncation increases the fraction of direct radiation and by the same amount decreases the fraction of scattered radiation. Thus, to maintain energy conservation, the single-scattering properties have to be scaled accordingly with f_{tr} , the fraction of energy within the truncated forward peak.

With the scaled scattering cross section C'_{sca} defined by $C'_{\text{sca}} = (1 - f_{\text{tr}}) \cdot C_{\text{sca}}$ and an unchanged absorption cross section $C'_{\text{abs}} = C_{\text{abs}}$, the extinction cross section C_{ext} and the single-scattering albedo $\tilde{\omega}$ are scaled accordingly by,

$$C'_{\text{ext}} = (1 - f_{\text{tr}} \tilde{\omega}) \cdot C_{\text{ext}} \quad (2.23)$$

and

$$\tilde{\omega}' = \frac{1 - f_{\text{tr}}}{1 - f_{\text{tr}} \tilde{\omega}} \cdot \tilde{\omega}. \quad (2.24)$$

Practical approaches for the truncation of the forward scattering peak are introduced by Joseph et al. (1976), Wiscombe (1977), and Hu et al. (2000).

Assuming spherical ice crystals, Mie-theory (Mie, 1908; Bohren and Huffman, 1998) can be used to derive the single-scattering optical properties. Parameterizations of the spectral single-scattering properties of nonspherical individual ice crystals derived from various accurate and approximate computational methods are given by Takano and Liou (1989, 1995); Iaquinta et al. (1995); Yang and Liou (1996); Macke et al. (1996); Macke and Francis (1998); Yang et al. (2000). These in combination with either theoretical or observational ice crystal number size distributions led to parameterizations of bulk ice cloud optical properties (*e.g.*, Fu, 1996; Mitchell et al., 1996; Chou et al., 2002; Key et al., 2002; Baum et al., 2005b). In this work, the parameterizations of Key et al. (2002) for six individual crystal habits, and

Baum et al. (2005b) for a particle-size dependent mixture of particle habits are employed (cf. Section 4.1.4).

2.2.2 Microphysical Properties

The **effective radius** R_{eff} (μm) is an area-weighted mean radius characterizing a crystal size distribution in radiative transfer calculations. It can be understood as the representative distance a photon travels through a particle without internal reflections or refraction occurring. It thereby is the relevant dimension for the interaction of a single particle with EM radiation (Mitchell, 2002). Depending on the applied ice cloud radiative parameterization scheme, different definitions of R_{eff} are given. A detailed review on that issue is made in McFarquhar and Heymsfield (1998). This work follows Yang et al. (2000) and Key et al. (2002), who define R_{eff} of nonspherical ice crystals as:

$$R_{\text{eff}} = \frac{3}{4} \frac{\int V(\tilde{D}) \cdot \frac{dN}{d\tilde{D}}(\tilde{D}) d\tilde{D}}{\int A(\tilde{D}) \cdot \frac{dN}{d\tilde{D}}(\tilde{D}) d\tilde{D}} \quad (2.25)$$

with D (μm) being the maximum dimension of an ice crystal, $\frac{dN}{dD}(D)$ being the number of ice crystals with maximum dimension D , V and A being the volume and projected area of the particles, respectively. V and A are based on the spherical diameter with equivalent volume and the spherical diameter with equivalent projected area, respectively. The terms equivalent volume/projected area refer to spheres having the same volume/projected area as the non-spherical ice crystals (Grenfell and Warren, 1999; Yang et al., 2000).

The **ice water path** IWP (g m^{-2}) is the vertical integral of the ice water content IWC (g m^{-3}):

$$IWP = \int_{z_{\text{base}}}^{z_{\text{top}}} IWC(\tilde{z}) d\tilde{z}, \quad (2.26)$$

with the **ice water content** IWC (g m^{-3}) defined as mass concentration of the ice crystals in the cloud volume:

$$IWC = \varrho_{\text{ice}} \int V(\tilde{D}) \cdot \frac{dN}{d\tilde{D}}(\tilde{D}) d\tilde{D}. \quad (2.27)$$

Integration limits are not indicated, they theoretically extend from 0 to ∞ but are practically set to a finite upper and nonzero lower limit chosen in a way that guarantees integration over the entire size spectrum.

2.2.3 Volumetric Optical Properties

The optical properties of a cloud volume are obtained by integration of the single-scattering optical properties weighted by the number size distribution of the scattering cloud parti-

cles $\frac{dN}{dD}(D)$. The (spectral) **volumetric extinction coefficient** b_{ext} (in units of m^{-1}) is calculated by:

$$b_{\text{ext}} = \int C_{\text{ext}}(\tilde{D}) \cdot \frac{dN}{dD}(\tilde{D}) d\tilde{D}. \quad (2.28)$$

The volumetric absorption- and scattering coefficient (b_{abs} and b_{sca} , both in units of m^{-1}) are derived by replacing C_{ext} in Equation 2.28 with C_{abs} and C_{sca} , respectively.

The dimensionless **volumetric single-scattering albedo** $\langle \tilde{\omega} \rangle$ is obtained by

$$\langle \tilde{\omega} \rangle = \frac{1}{b_{\text{ext}}} \int \tilde{\omega}(\tilde{D}) \cdot C_{\text{ext}}(\tilde{D}) \cdot \frac{dN}{dD}(\tilde{D}) d\tilde{D}. \quad (2.29)$$

In a similar way, the **volumetric scattering phase function** $\langle \mathcal{P}(\cos \vartheta) \rangle$ is derived:

$$\langle \mathcal{P}(\cos \vartheta) \rangle = \frac{1}{b_{\text{sca}}} \int \mathcal{P}(\cos \vartheta, \tilde{D}) \cdot C_{\text{sca}}(\tilde{D}) \cdot \frac{dN}{dD}(\tilde{D}) d\tilde{D}. \quad (2.30)$$

The integral of the volumetric extinction coefficient of a cloud with cloud base z_{base} and cloud top z_{top} over geometric height z is defined as cloud **optical thickness** τ (dimensionless).

$$\tau(z) = \int_{z_{\text{base}}}^{z_{\text{top}}} b_{\text{ext}}(\tilde{z}) d\tilde{z}. \quad (2.31)$$

τ can be estimated from the microphysical cloud properties effective radius (R_{eff}) and ice water path (IWP) using the approximation:

$$\tau = \frac{3 IWP}{2 \rho_{\text{ice}} R_{\text{eff}}} \quad (2.32)$$

with ρ_{ice} being the density of ice (0.9167 g cm^{-3}).

2.3 Radiative Transfer Equation

With all the necessary radiative quantities and optical- as well as microphysical ice cloud properties defined, the attenuation of direct solar radiance I_{dir} in the (cloudy) atmosphere along τ as vertical coordinate can be described via the Law of Beer, Lambert, and Bouguer:

$$I_{\text{dir}}(\tau, \mu_0, \varphi_0) = \frac{S_0}{4\pi \text{ sr}} \cdot \exp \left[-\frac{\tau}{\mu_0} \right]. \quad (2.33)$$

S_0 is the solar constant (the extraterrestrial irradiance incidenting at the top of the atmosphere), $\mu_0 = \cos \theta_0$ and φ_0 define the position of the sun. Interpreting Eq. 2.33 shows that I_{dir} decreases exponentially along τ . Thus, I_{dir} is strongly attenuated in the presence of

clouds, allowing to describe the solar radiative transfer in clouds by the diffuse radiance I_{diff} only. The one-dimensional (1D) **radiative transfer equation** (RTE) assuming a plane-parallel, horizontally homogeneous atmosphere thus is (Chandrasekhar, 1950):

$$\mu \frac{dI_{\text{diff}}(\tau, \mu, \varphi)}{d\tau} = I_{\text{diff}} - (J_{\text{dir}} + J_{\text{diff}} + J_{\text{emi}}). \quad (2.34)$$

with J_{dir} and J_{diff} describing the amount of radiation that is scattered into the viewing direction, either from the direct solar beam (J_{dir} , single-scattering term) or from diffuse radiation (J_{diff} , multiple-scattering term). In the solar spectral range (which will subsequently be considered, wavelength range $\lambda = 0.2\text{--}5\ \mu\text{m}$), thermal emission can be neglected: $J_{\text{emi}} = 0$. The viewing direction (or direction of propagation of I_{diff}) is characterized by $\mu = \cos \theta$, the cosine of the zenith angle θ , and the azimuth angle φ . J_{dir} and J_{diff} depend on $\tilde{\omega}$ and \mathcal{P} and are defined as:

$$J_{\text{dir}} = \frac{\tilde{\omega}(\tau)}{4\pi \text{ sr}} \cdot S_0 \cdot \exp\left[-\frac{\tau}{\mu_0}\right] \cdot \mathcal{P}(\tau, [-\mu_0, \varphi_0] \rightarrow [\mu, \varphi]) \quad (2.35)$$

$$J_{\text{diff}} = \frac{\tilde{\omega}(\tau)}{4\pi \text{ sr}} \int_0^{2\pi} \int_{-1}^1 I_{\text{diff}}(\tau, \mu', \varphi') \cdot \mathcal{P}(\tau, [\mu', \varphi'] \rightarrow [\mu, \varphi]) \, d\mu' \, d\varphi'. \quad (2.36)$$

3 Experimental

Solar spectral radiation data used for the determination of cirrus properties (cf. Section 5.1) was obtained with the Spectral Modular Airborne Radiation measurement system (SMART)-Albedometer (Wendisch et al., 2001) during the CIRrus CLoud Experiment-2 (CIRCLE-2) in May 2007. Section 3.1 introduces the instrument, in Section 3.2 the CIRCLE-2 field experiment is described.

3.1 The SMART-Albedometer

3.1.1 Setup

The SMART-Albedometer was developed at the Leibniz-Institute for Tropospheric Research (IfT), Leipzig, Germany in collaboration with the company *enviscope* GmbH, Frankfurt/Main, Germany. The instrument was designed for airborne measurements of spectral radiometric quantities in the solar spectral range. This is realized by connecting specific optical inlets which are pointing in upward or downward direction to a set of up to six grating spectrometers which in turn are coupled to a computer control system. Depending on the scientific question, the optical inlets which determine the measured radiometric quantities can be chosen.

Originally, the SMART-Albedometer was used to measure upwelling and downwelling irradiances in order to determine the surface albedo (cf. Section 2.1) (*e.g.*, Wendisch et al., 2001; Wendisch and Mayer, 2003; Wendisch et al., 2004) - hence the name *Albedometer*. For that application an active stabilization system keeping the optical inlets in horizontal position during aircraft attitude changes of up to $\pm 6^\circ$ from the horizontal plane was developed to obtain credible irradiance measurements (Wendisch et al., 2001). Jäkel et al. (2005) used commercial isotropic optical inlets to measure actinic flux densities. Ehrlich et al. (2008) developed optical inlets for radiance measurements. The original spectral range covered by the SMART-Albedometer was 290–1000 nm. It was extended by Bierwirth (2008) to 2200 nm thus covering approximately 97% of the entire solar spectrum. Initially, the SMART-Albedometer was configured for measurements at low altitude with unpressurized aircraft (*e.g.*, the POLAR-2 and the Partenavia D-GERY flying maximum altitudes of 3000 m). Data presented in this work was obtained by first measurements of the SMART-Albedometer on high-altitude, pressurized aircraft. Thus, proper evacuation of the optical inlets which were mounted on the boundary between pressurized cabin and the outside had to be assured. For that reason, the radiance inlet was evacuated to 90 mbar in order to be able to use it under low atmospheric pressure conditions in 9–12 km height.

Table 3.1: Characteristics of the two spectrometers of the SMART-Albedometer used for this work.

Name	Type	Spectral Range (nm)	Spectral resolution ($FWHM$, nm)	Number of PDA pixels
VIS	MCS 55 UV/NIR	200–1000	2–3	1024
NIR	PGS 2.2	900–2200	16	256

The path of photons entering an optical inlet is as follows (cf. Figure 3.1a): Via bifurcated optical fibers, photons are directed to a set of two grating spectrometers. Incoming photons are spectrally dispersed by a grating and then detected by a single-line photodiode array (PDA). The resulting electric signal is recorded by computers (PC). Different types of spectrometers manufactured by (*Carl Zeiss Jena GmbH*, Jena, Germany) are used in the SMART-Albedometer. The Multi Channel Spectrometer (MCS 55 UV/NIR) with a 1024 pixel PDA and a spectral resolution (Full Width at Half Maximum, $FWHM$) of 2–3 nm covers the 200–1000 nm region including the entire visible (VIS) wavelength range (380–700 nm) and is thus named VIS subsequently. The PGS 2.2 (Plane Grating Spectrometer 2.2) operating in the near infrared wavelength range (900–2200 nm, from now on called NIR) has a 256 pixel PDA and a $FWHM$ of 16 nm. The characteristics of the two types of spectrometers are listed in Table 3.1. Measurements in the NIR wavelength range require realtime acquisition of the so-called dark signal, a thermally induced current, which needs to be subtracted from the signal. This is realized by alternating measurements of radiation and dark signal via plugging a mechanical shutter in the optical path. For the VIS spectrometer, the situation is more simple. In the atmosphere, there is no natural radiation below 280 nm so the corresponding signal measured at 200–280 nm can be used as an estimate of the dark signal. This technique can not be applied for the NIR where natural radiation might be encountered at any of the covered wavelengths.

Even though the VIS and NIR spectrometers cover the wavelength range 200–1000 nm, and 900–2200 nm, respectively, reliable data can only be acquired in the range 350–2150 nm due to limitations in the transmittivity of the optical fibers, the sensitivity of the PDA, the calibration lamp characteristics as well as the upper limit of the integration time T_{int} (6.5 s / 1.5 s for the VIS/NIR). T_{int} describes the accumulation time of the electric signal from the PDA by an integrating circuit.

A sketch of the setup of the SMART-Albedometer applied during the CIRCLE-2 field experiment is shown in Figure 3.1a. Due to operational constraints of the aircraft (a Falcon 20 operated by DLR, the German Aerospace Center), only one downward-looking radiance inlet to measure I_{λ}^{\uparrow} could be installed. An active stabilization of optical inlets is only necessary for the measurement of F and was therefore not mounted. Instead, the attitude of the radiance inlet was obtained from measurements of the aircraft attitude angles.

The construction and characterization of the radiance optical inlet is described by Ehrlich (2009). As illustrated in Figure 3.1b the inlet consists of a collimator lens acting as entrance optic for the photons. The lens is mounted inside a cylindrical black plastic housing. For stray light reduction, an aperture was placed directly in front of the collimator lens. In order

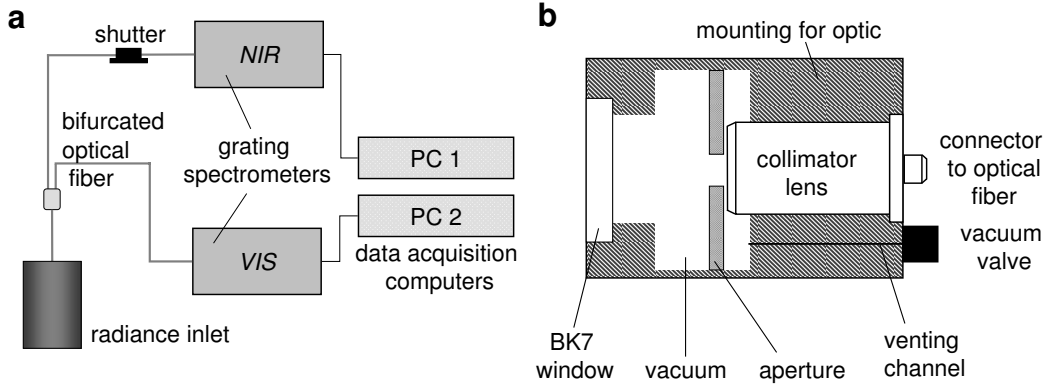


Figure 3.1: a) Sketch of a) the SMART-Albedometer setup during the CIRCLE-2 experiment and b) of the radiance inlet.

to be able to evacuate the radiance inlet, a BK7 glass cover and a vacuum valve were installed in the front and the back of the housing, respectively. The optical fiber can be connected to the back of the lens by a SMA connector. The opening angle of the radiance inlet Δ depends on the collimator lens and the optical fiber connected to it. In laboratory tests an opening angle of 2.1° was determined for the configuration used in this work.

$$d_i = 2z \cdot \arctan \frac{\Delta}{2}. \quad (3.1)$$

Δ controls the instantaneous footprint diameter d_i of the radiance inlet (cf. Figure 3.2a). With increasing distance between the surface and the radiance inlet (mounted on an aircraft) d_i increases according to Eq. 3.1. Flying in 100 m/1000 m/10000 m above ground, results in d_i of 3.7 m/37 m/370 m, respectively. For remote sensing measurements during CIRCLE-2, the Falcon aircraft was flying several hundred meters above the cirrus, so that d_i was on the order of 3–15 m (cf. Figure 3.2b). However, the spatial resolution of the measurement also depends on aircraft velocity and the set T_{int} . During CIRCLE-2 the temporal resolution of the I_λ^\uparrow measurement was set to 0.5 s leading to an averaging of 100 m along flight track at an aircraft velocity of 200 m s^{-1} .

3.1.2 Radiometric Calibration

Via calibration against a certified source of diffuse radiation, the measured digital signal of the SMART-Albedometer $G(\lambda)$ is converted into spectral radiance. Ideally, a single radiation source covering the complete reliable wavelength range (350–2150 nm) is used. Alternatively, two techniques were tested and compared. Firstly, a certified integrating sphere manufactured by *Gigahertz-Optik* GmbH, Puchheim, Germany was used. The integrating sphere (model UMBB-500) emits EM radiation in the wavelength range 380–2500 nm. Secondly, measurements with a 1000 W irradiance standard in combination with a reflectance panel to cover the smaller wavelengths (350–380 nm) were made.

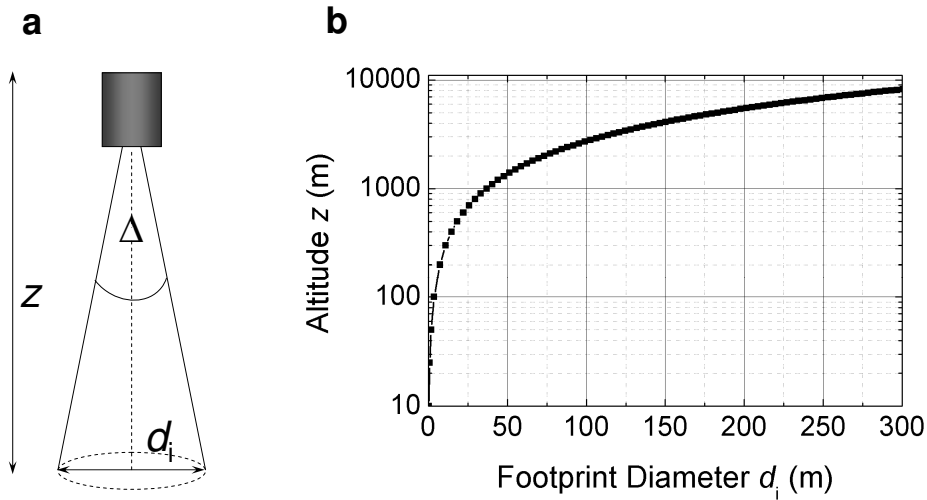


Figure 3.2: Illustration of a) the instantaneous footprint diameter d_i of the radiance optical inlet and b) of d_i as function of altitude.

Figure 3.3a illustrates the setup for the calibration with the integrating sphere. The radiance inlet is placed in front of the exit aperture of the sphere. The inside of the sphere is coated with barium sulfate acting as Lambertian reflector. At the side of the sphere a lamp is mounted in a ventilated housing. A baffle is placed in such a way that radiation cannot directly reach the exit port. The integrating sphere has a diameter of 50 cm to minimize geometric effects of the lamp and baffle. The radiation emitted by the lamp is reflected by the barium sulfate coating leading to isotropic diffuse radiation. Through the exit aperture, spectral radiance $I_{\lambda,S}$ is emitted and then received by the radiance inlet. $I_{\lambda,S}$ is certified via a calibration traceable to standards of the German Calibration Service. The calibration factor $K_{\lambda,S}$ obtained with the integrating sphere is calculated as:

$$K_{\lambda,S} = \frac{I_{\lambda,S}}{G(\lambda)}. \quad (3.2)$$

For each spectrometer pixel (i.e., for each wavelength), $G(\lambda)$ is determined by subtracting the dark signal from the measured digital signal (both normalized to $T_{\text{int}} = 1$ s). $G(\lambda)$ is also referred to as net photon counts (Bierwirth, 2008).

The radiometric calibration made with the reflectance panel (manufactured by *Gigahertz-Optik GmbH*) is presented in Figure 3.3b. The measurement setup was placed inside a black metal housing to minimize stray light. The defined irradiance $F_{\lambda,L}$ emitted by a 1000 W irradiance standard is reflected by the panel made of Spectralon[®] material. This material acts as Lambertian surface thus guaranteeing that the reflected radiation is diffuse. The panel reflectance $r_P(\lambda)$ is certified by a calibration traceable to the National Institute of Standards and Technology (NIST) standards. In the calibration certificate, an angle of 8° between the incident $F_{\lambda,L}$ and the panel surface normal is required. For practical reasons the distance between the irradiance standard and the panel was set to $l = 71.5$ cm instead of $l_0 = 50$ cm for which the irradiance standard is certified. With the given configuration, the calibration factor $K_{\lambda,P}$ is determined by:

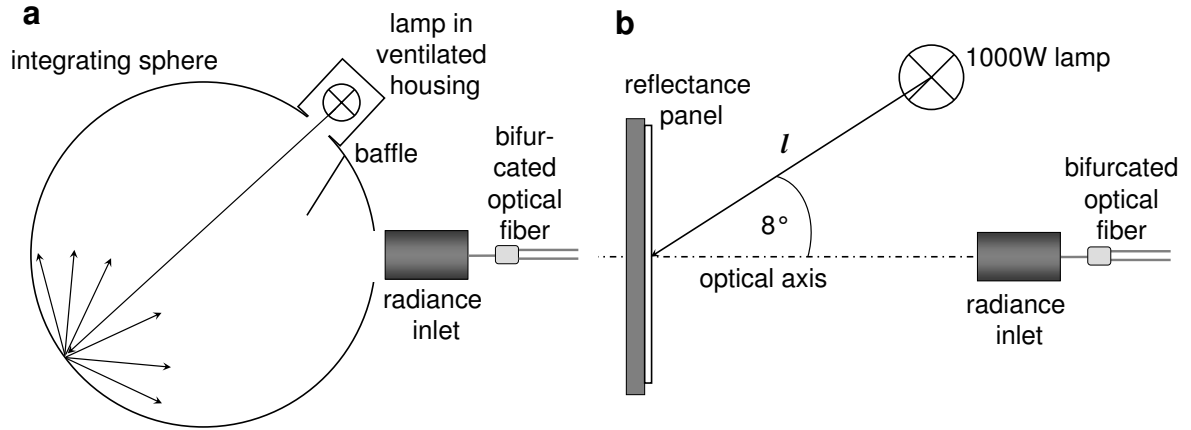


Figure 3.3: Radiance calibration setup using (a) an integrating sphere and b) a reflectance panel.

$$K_{\lambda,P} = \frac{l^2}{l_0^2} \cdot \frac{F_{\lambda,L}}{\pi_{SF} \cdot r_P(\lambda)} \cdot \frac{1}{G(\lambda)}. \quad (3.3)$$

In Figure 3.4a, $K_{\lambda,S}$ and $K_{\lambda,P}$ obtained for the VIS spectrometer for the CIRCLE-2 experiment are shown. The strong spectral dependence of the calibration factors is attributed to the spectral output of the radiation sources, the spectrometer characteristics (with lowest sensitivities at the lowest and largest pixel numbers, i.e., wavelengths), absorption of radiation by the BK7 glass used in the radiance inlet and within the optical fiber. $K_{\lambda,S}$ increases significantly for short wavelengths because the integrating sphere only emits radiation at wavelengths $\lambda \geq 380$ nm. For $\lambda = 400\text{--}700$ nm, $K_{\lambda,S}$ and $K_{\lambda,P}$ agree to within 3%. The discrepancy of both types of calibration factors for wavelengths larger than 700 nm is due to stray light in the NIR wavelength range in the panel calibration setup. Thus, $K_{\lambda,P}$ is not trustworthy for $\lambda \geq 700$ nm. For later experiments, the amount of stray light was reduced by painting the housing of the setup with highly absorbing paint resulting in agreement of $K_{\lambda,S}$ and $K_{\lambda,P}$ to within 2% for the wavelength range 400–1000 nm (not shown). For the VIS spectrometer, the calibration factor was merged from both calibration methods using $K_{\lambda,P}$ for $\lambda \leq 405$ nm and $K_{\lambda,S}$ for $\lambda \geq 405$ nm. Calibration factors were determined for different T_{int} . However, it was found that for the VIS spectrometer, $K_{\lambda,S}$ and $K_{\lambda,P}$ are independent of T_{int} .

Due to the mentioned stray light problem in the calibration with the panel, the calibration factor of the radiance measurements with the NIR spectrometer was determined using the integrating sphere only. Unlike to the VIS spectrometer, $K_{\lambda,S}$ determined for the NIR spectrometer depends on T_{int} as illustrated in Figure 3.4b. With increasing T_{int} , $K_{\lambda,S}$ exhibits more pronounced peaks. This behaviour can be attributed to the non-linear dark signal dependence on T_{int} for the NIR spectrometer (Bierwirth, 2008). As a consequence, for each T_{int} used in the NIR wavelength range in the field experiment, a calibration factor $K_{\lambda,S}$ was determined according to Eq. 3.2. The spectral dependence of $K_{\lambda,S}$ is explained by the absorption of radiation in the optical fiber, the decrease of spectral output of the integrating sphere

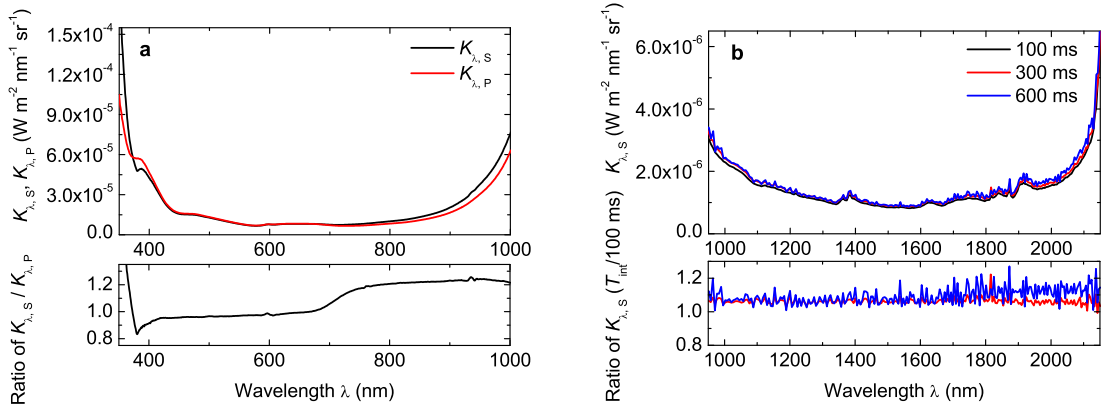


Figure 3.4: Calibration factors for radiance measurements with a) the VIS spectrometer obtained from calibration with a reflectance panel $K_{\lambda,P}$ and an integrating sphere $K_{\lambda,S}$ and b) the NIR spectrometer obtained at different integration times ($T_{\text{int}} = 100$ ms, 300 ms, 600 ms) using the integrating sphere.

($I_{\lambda,S}$) with increasing wavelength, and the decrease of sensitivity of the NIR spectrometer at the lowest and largest pixel numbers (i.e., wavelengths).

When the SMART-Albedometer is transported and installed on an airplane the optical fibers need to be disconnected from the spectrometers. Each reconnection results in changed transmission properties between the optical fibers and the spectrometers since the connection and alignment of the optical fibers is not perfectly reproducible. These changes in sensitivity of the measurement system are accounted for by a transfer calibration made with a portable barium-sulfate coated integrating sphere (manufactured by *LOT-Oriel GmbH*, Darmstadt, Germany) with constant radiance output. The output of this integrating sphere was measured in the laboratory ($G_{\text{lab}}(\lambda)$) and in the field during CIRCLE-2 ($G_{\text{fld}}(\lambda)$), thus the transfer calibration factors were determined as:

$$K_{\lambda,T} = \frac{G_{\text{lab}}(\lambda)}{G_{\text{fld}}(\lambda)}. \quad (3.4)$$

The output of the portable integrating sphere was measured six times during CIRCLE-2. Resulting $K_{\lambda,T}$ are displayed in Figure 3.5. For most part of the wavelength range covered by the VIS and the NIR spectrometer, $K_{\lambda,T}$ is greater than unity meaning that during CIRCLE-2 the transmission (and thus the digital signal G_{fld}) of the measurement setup was lower than in the laboratory (G_{lab}). Depending on wavelength, $K_{\lambda,T}$ vary by approximately 1–4% for the VIS spectrometer. For the NIR spectrometer, the temporal variability in $K_{\lambda,T}$ amounts to only 1–2%. Thus, the temporal drift of the NIR spectrometer is less than that of the VIS spectrometer.

The digital signal $G(\lambda)$ measured during the experiment flights of CIRCLE-2 was converted into values of I_{λ}^{\uparrow} by multiplication with the radiometric calibration factor and the transfer calibration factor:

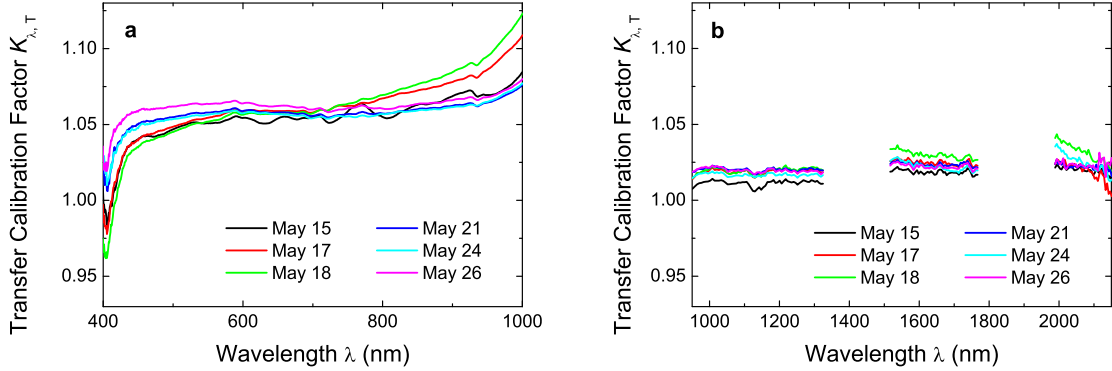


Figure 3.5: Transfer calibration factors $K_{\lambda,T}$ for measurements of I_{λ}^{\uparrow} during CIRCLE-2 determined for a) the VIS spectrometer and b) the NIR spectrometer. For regions with water vapor absorption lines, $K_{\lambda,T}$ is not shown.

$$I_{\lambda}^{\uparrow} = G(\lambda) \cdot K_{\lambda,P/S} \cdot K_{\lambda,T}. \quad (3.5)$$

I_{λ}^{\uparrow} obtained with the VIS- and the NIR spectrometer were concatenated resulting in I_{λ}^{\uparrow} spectra covering the wavelength range 350–2150 nm. For wavelengths smaller (larger) than 950 nm, I_{λ}^{\uparrow} measured with the VIS (NIR) spectrometer were used. T_{int} of both spectrometers can be set independently so that the number of measurement scans per time interval differs. Tests in concatenating both parts of the I_{λ}^{\uparrow} -spectrum proved that a maximum time lag between I_{λ}^{\uparrow} from the VIS- and the NIR spectrometer of 1 s is reasonable.

3.1.3 Measurement Uncertainties

Several parameters add to the total uncertainty of the I_{λ}^{\uparrow} measurements. The individual measurement uncertainties are assumed to be random and therefore independent of each other. Thus, the composite relative uncertainty (in %) can be determined with Gaussian error propagation.

The relevant measurement uncertainties are:

- Calibration lamp uncertainties,
- Wavelength accuracy of the spectrometers,
- Dark signal fluctuations, and
- Transfer calibration uncertainties.

These wavelength-dependent uncertainties are listed in Table 3.2. For wavelengths $\lambda \leq 405$ nm, calibration lamp uncertainties are related to the reflectance panel and the 1000 W irradiance standard. Their calibration uncertainties are specified by the manufacturer and amount to 0.8% and 5%, respectively. Applying Gaussian error propagation to

Table 3.2: Sources of error contributing to the measurement uncertainty of I_{λ}^{\uparrow} . The total error (%) was determined with Gaussian error propagation.

Wavelength range (nm)	Calibration lamp	Dark signal fluctuation	Wavelength accuracy	Transfer calibration	Total error
350–405	5.1 %	< 0.7 %	0.7 %	1.6 %	5.4 %
405–450	7 %	< 0.7 %	0.6 %	1.2 %	7.2 %
450–800	6 %	< 0.7 %	0.2 %	0.8 %	6.1 %
800–1850	9 %	< 1.5 %	0.2 %	1.6 %	9.3 %
1850–1950	9 %	< 1.5 %	0.6 %	1.6 %	9.3 %
1950–2200	10 %	< 1.5 %	0.2 %	1.6 %	10.2 %

these two uncertainties results in a calibration lamp uncertainty of 5.1%. For wavelengths $\lambda \geq 405$ nm, the integrating sphere was used as radiation standard, its calibration certificate states wavelength-dependent uncertainties of 6–10%. The wavelength-to-pixel relationship of the spectrometers was determined from emission lines of noble gas lamps as reported by Bierwirth (2008). The *FWHM* of the spectrometers was determined by the broadening of the measured emission lines. The accuracy of the wavelength-to-pixel relationship is reduced by the *FWHM* resulting in an uncertainty of the wavelength accuracy of 0.2–0.7%.

Fluctuations in the dark signal were also estimated by Bierwirth (2008). For the VIS spectrometer, the digital signal measured at $\lambda = 200$ –280 nm (where no photons should be detected) is used as estimate of the dark signal for the entire VIS wavelength range ($\lambda = 350$ –950 nm). This assumption of spectral independence of the dark signal was found to cause an error of < 0.7%. Since the dark signal (i.e., the digital signal at $\lambda = 200$ –280 nm) is measured at the same time as the rest of the spectrum, no temporal fluctuation of the dark signal needs to be considered for the VIS spectrometer. The dark signal of the NIR spectrometer is the digital signal that is observed when the shutter is plugged in the optical path. Thus, for NIR spectrometer the wavelength dependence of the dark signal is known. However, temporal fluctuations of the dark signal were found to result in errors of < 1.5%. The transfer calibration uncertainty ranging between 0.8–1.6% determined by the standard deviation σ of all six transfer calibrations performed during CIRCLE-2. Applying Gaussian error propagation to the listed uncertainties results in wavelength-dependent total errors of 5.4–10.2% for measured I_{λ}^{\uparrow} as shown in Table 3.2.

3.2 The CIRCLE-2 Experiment

3.2.1 Overview

Data presented in this section were obtained during the CIRCLE-2 field campaign in May 2007. This experiment focused on the airborne measurement of radiative and microphysical properties of cirrus to validate retrieval algorithms based on satellite measurements, in particular of Meteosat Second Generation (MSG) and CALIPSO/CloudSat of the A-Train (Stephens et al., 2002). Airborne measurements were conducted with two research

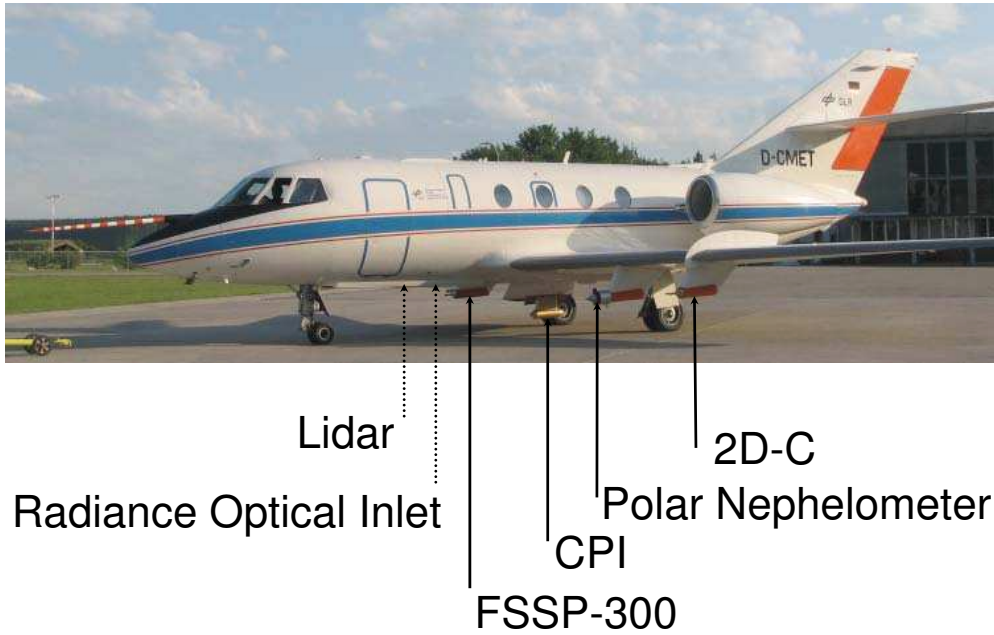


Figure 3.6: Instrumentation of the German Falcon aircraft during CIRCLE-2. Dotted arrows indicate the approximate position of the lidar and the radiance optical inlet on the fuselage. In this work, the 2D optical array probe 2D-C and the polar nephelometer were not considered and are only labeled here for completeness.

aircraft: a German Falcon 20 operated by DLR and a French Falcon 20 operated by SAFIRE (Service des Avions Français Instrumentés pour la Recherche en Environnement). Both aircraft were equipped with lidars in nadir looking configuration. In addition, in situ cloud and aerosol properties as well as upwelling spectral radiances (I_{λ}^{\uparrow}) were measured onboard the German Falcon while the French Falcon also carried a radar system. The instrumentation of the German Falcon aircraft is illustrated in Figure 3.6.

20 flights were performed over continental Europe, the North Sea, and the Atlantic Ocean as summarized in Table 3.3. The time period of the aircraft operation was limited to two weeks. Thus, a rather large operational area was required in order to meet the best possible meteorological situations for cirrus observations, combined with the location of the daytime CALIPSO/CloudSat overpass tracks and restrictions imposed by air traffic control (ATC) in different European countries. The preferred meteorological conditions were single-layer cirrus clouds over water surfaces. At the same time, the cirrus cloud tops should be low enough for the aircraft to fly above the cirrus for the lidar and reflectance measurements. It turned out to be quite difficult to meet all meteorological and operational conditions at the same time. For flight planning and go/no-go decisions, customized products of ECMWF (European Centre for Medium-Range Weather Forecasts) forecast data as well as MSG images were used.

During three missions (cf. Table 3.3) both Falcon aircraft were flying in close coordination. While the French Falcon was flying above clouds for lidar and radar observations, the German Falcon was positioned below the French Falcon for in situ measurements inside the cirrus clouds. However, in the specific cases investigated in this study, the German Falcon was operating separately. The flight strategy in this case was to first fly above the cirrus for the

Table 3.3: Overview of flights performed during the CIRCLE-2 field experiment in May 2007. Cloud type Ci and Sc denote cirrus and strato cumulus, respectively. OP is Oberpfaffenhofen, F refers to the French-, G to the German Falcon aircraft, respectively. Geographical coordinates of the locations are as follows: Bilbao (43.3°N, 2.93°W), Brest (48.45°N, 4.42°W), Creil (49.25°N, 2.5°E), Esbjerg (55.53°N, 8.57°E), Leipzig (51.33°N, 12.38°E), OP (48.08°N, 11.28°E). Flights with concurrent satellite overpasses (CloudSat/CALIPSO) are marked with an X.

May	Route	Cloud type	Aircraft	Satellite
13	Creil - Creil	Convective clouds	F	X
14	OP - Leipzig	Broken Ci	G	X
14	Leipzig - OP	Broken Ci	G	
16	OP - Brest	Frontal Ci	G	
16	Brest - Brest	Frontal Ci	F + G	X
16	Brest - OP	Frontal Ci	G	
17	OP - OP	Sc	G	
20	Creil - Creil	Broken Ci	F	X
20	OP - OP	Outflow Ci	G	
22	OP - Esbjerg	Frontal Ci	G	
22	Esbjerg - OP	Frontal Ci	G	
23	OP - Bilbao	Outflow Ci	G	
23	Bilbao - Bilbao	Outflow Ci	G	X
23	Bilbao - OP	Outflow Ci	G	
25	OP - Brest	Broken Ci	G	
25	Brest - Brest	Ci layer	F + G	X
25	Brest - OP	Outflow Ci	G	
26	Brest - OP	Outflow Ci	F	
26	OP - OP	Outflow Ci	F + G	X
26	OP - Brest	Outflow Ci	F	

remote sensing measurements, then turn around and fly several legs at different altitudes inside the cloud. This procedure typically caused a time delay between roughly collocated remote sensing and in situ measurements in the range of 5–20 min.

As illustrated in Table 3.3, the aircraft cirrus measurements were closely collocated with observations of CALIPSO/CloudSat during several missions. Results of these cases are described by Mioche et al. (2009).

3.2.2 Radiation Measurements

As mentioned in Section 3.1.1, only one optical inlet to measure I_{λ}^{\uparrow} with the SMART-Albedometer was installed during CIRCLE-2 due to operational constraints of the German Falcon aircraft. The I_{λ}^{\uparrow} -inlet was installed next to the lidar on the fuselage in approximately nadir direction (deviation from nadir 4–5°) as indicated in Figure 3.6. Via bifurcated optical fibers, the inlet was connected to two plane grating spectrometers (a VIS and a NIR spectrometer, cf. Figure 3.1a) thus allowing well-calibrated spectral radiance measurements in the wavelength range of $\lambda = 350\text{--}2150\text{ nm}$.

3.2.3 Additional Instrumentation

With WALES (WATER vapor Lidar Experiment in Space), the multi-wavelength water vapor differential absorption lidar operated by DLR onboard the German Falcon, lidar signal backscatter ratios at 1064 nm wavelength were measured (Wirth et al., 2009). An extinction correction of the data was applied assuming a vertically constant backscatter-to-extinction-ratio of 20 sr which is a typical value for cirrus in the northern hemisphere at this wavelength. The *Klett*-inversion method (Klett, 1981) was used to determine τ from the lidar data. Due to the exponential increase of the error for cirrus with increasing τ , lidar-derived τ were reliable for optically thin clouds only. For optically thin cirrus with $\tau < 2$, uncertainties in derived τ are estimated as 20–30 %.

Onboard the DLR Falcon aircraft, microphysical in situ measurements were made. Ice particle number size distributions and ice particle concentrations were obtained by a Forward Scattering Spectrometer Probe (FSSP-300, Baumgardner et al. (1992)) and a Cloud Particle Imager (CPI, Lawson et al. (2001)). The former was operated by DLR, the latter by the Laboratoire de Météorologie Physique, Université Blaise Pascal (LaMP), Clermont Ferrand, France. The FSSP-300 detects radiation that is scattered by the ice crystals passing through the sample volume where they are illuminated with a Helium-Neon laser (emitting radiation at $\lambda = 632$ nm). The intensity of the scattered radiation is proportional to the size of the scattering particles. From this relation ice crystal sizes are obtained assuming that the particles are spherical. The FSSP-300 covers a size range of 3 to 20 μm . The CPI records high-definition digital images of cloud particles and measures their size, shape, and concentration in the size range 20–2300 μm . Using a high-power laser diode, the CPI casts an image of an ice crystal on a Charged-Coupled Device (CCD) camera with one million pixels. Ice crystal shapes were determined in post-processing from the CPI images. Based on these in situ measurements of microphysical properties, R_{eff} in units of μm were obtained from the ratio of IWC (in g m^{-3}) and b_{ext} (in m^{-1}) which are calculated from the particle size distribution:

$$R_{\text{eff}} = \frac{b \cdot IWC}{2 \cdot b_{\text{ext}}} \quad (3.6)$$

with the factor $b = 3 \text{ mm}^3 \text{ g}^{-1}$ (Gayet et al., 2004).

Measurements with microphysical probes mounted on an aircraft are influenced by particle shattering which causes artifacts. For several years, the issue of ice crystal shattering and thus the abundance of small ice crystals has been debated (e.g., Korolev and Isaac, 2005; Heymsfield, 2007; McFarquhar et al., 2007; de Reus et al., 2009; Jensen et al., 2009). In the obtained dataset, artifacts by shattering cannot be excluded. Shattered particles produce fragments that ricochet into the probe’s sensing area leading to a bias. Also, small particles that hit the leading surfaces of a FSSP can bounce into the sampling area. The CPI also experiences shattering. This is often seen as multiple particles in the same CPI frame (image). By rejecting particles which have interarrival times below a certain threshold, shattering can be paid attention to in the data processing. Thus, for the FSSP, uncertainties of b_{ext} and IWC amount to 60 % and 75 %, respectively (Gayet et al., 2004). The uncertainties of the

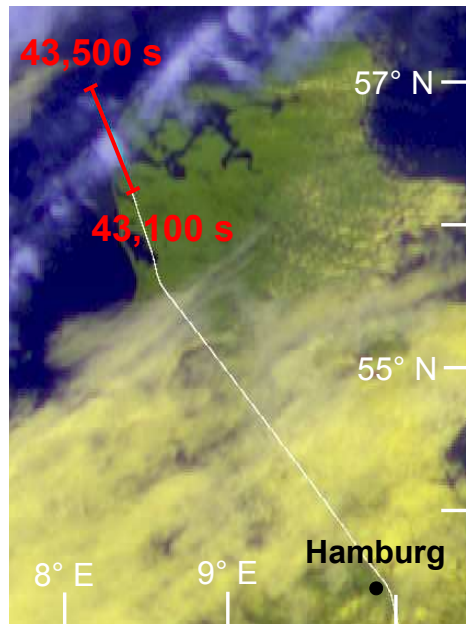


Figure 3.7: False colour composite using MSG-SEVIRI channels 1, 2, 9, and 12 of the west coast of Denmark at 12 UTC on May 22, 2007 with superimposed flight track over probed cirrus.

same quantities based on CPI measurements are 20 % and 30 %, respectively. In total, the uncertainty in R_{eff} determined from the microphysical measurements is estimated to be on the order of 85 % (G. Mioche, personal communication).

3.2.4 Case Study of May 22, 2007

Results from two case studies based on the first flight performed on 22 May 2007 (cf. Table 3.3) are presented. This day was chosen because single-layer cirrus was observed. Frontal cirrus associated with a low pressure system centered over Iceland was advected to Denmark from westerly directions. Only one aircraft (the German Falcon) was operated that day. The flight track led along the West Coast of Jutland, Denmark, where an inhomogeneous, thin and narrow cirrus band was present around 12–12:45 UTC (43,200–45,900 s). The cirrus is evident in the MSG-image (Figure 3.7) as white cloud band in the upper left corner of the map. The vertical profile of the cirrus is displayed in the lidar-obtained time series of attenuated backscatter ratio at 1064 nm wavelength in Figure 3.8.

The measurement strategy was as follows: First, a flight leg above the cirrus for remote sensing measurements at an altitude of 10.7 km with a heading to Northwestern direction was flown. This was followed by in-cloud flight legs for microphysical measurements at different altitudes. These flight legs lasting about 10 min each were conducted at four levels (9.78 km, 8.85 km, 8.22 km, and 7.6 km) with alternating flight directions (Southeast and Northwest). Figure 3.8 shows the uppermost leg at 9.78 km during which the Falcon was flying in a Southeastern direction. The vertical profile as well as the photo presented in Figure 3.9a show that the observed cirrus was spatially inhomogeneous. Areas of geometrically and optically thick cirrus alternated with geometrically and optically thinner parts. The cloud

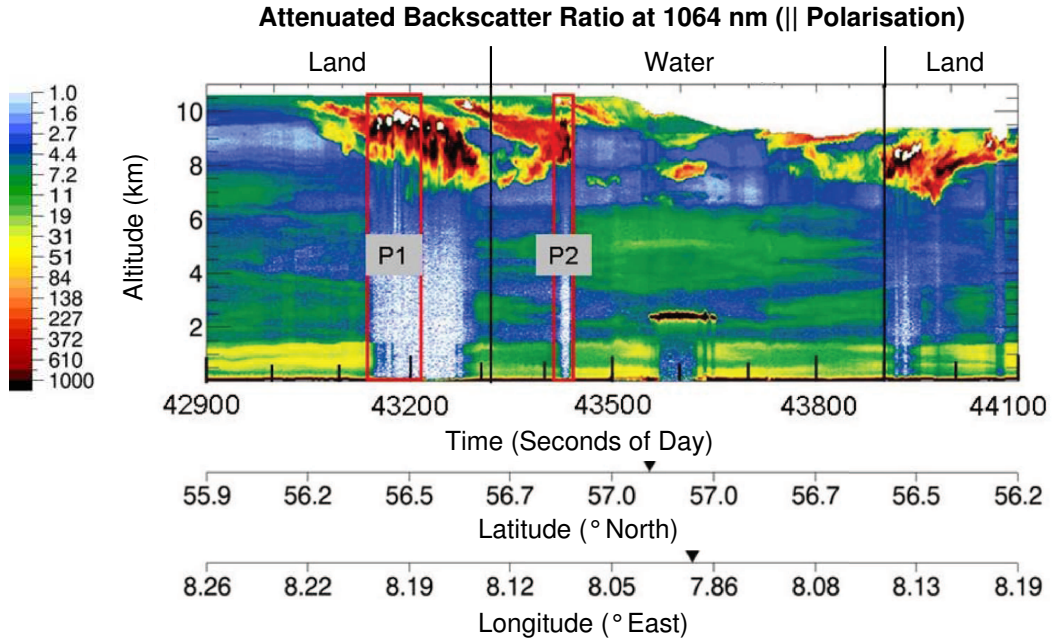


Figure 3.8: Attenuated backscatter ratio at a wavelength of 1064 nm from the DLR-lidar of the first flight on 22 May, 2007 (42,900–44,100 s). The area between the black vertical lines indicate the flight leg over the North Sea, the red boxes show the time spans for which cloud retrievals were made (P1 = 43,146–43,220 s, P2 = 43,419–43,435 s). Latitude and longitude of the flight track are included below the graph, turns are indicated by black triangles.

bottom and cloud top varied between 7–9.5 km and 9.8–10.5 km, respectively.

The retrieval of τ and R_{eff} (cf. to Section 4 for description of the retrieval methodology) was realized for parts of the cirrus over land during which the geometrical thickness of the cirrus was nearly constant (43,146–43,220 s) referred to as period P1 as well as for the cirrus over water denoted as period P2 (43,419–43,435 s). Both periods are marked by red boxes in Figure 3.8. In addition, the flight leg over water is indicated by the area between the black vertical lines. A low level liquid water cloud in about 2 km height was present at 43,580–43,650 s and thus did not overlap with the chosen time periods for the cirrus retrieval.

Timeseries of upwelling radiances measured at three wavelengths (635 nm, 810 nm and 1640 nm) during 43,000–43,500 s (11:56–12:05 UTC) corresponding to the flight leg in nearly 11 km height (above cloud) are presented in Figure 3.10 in which P1 and P2 are indicated as well. The wavelengths 635 nm, and 1640 nm were chosen because they are used for the cirrus retrieval while at 810 nm the influence of surface albedo is illustrated.

In Figure 3.10, the cirrus can be identified by the high values of I_{λ}^{\uparrow} at around 43,120–43,300 s (including P1). This part of the cirrus was situated over land. As obvious in the variations of I_{λ}^{\uparrow} during the cloud-free time before 43,120 s as well as photographs taken during the flight (cf. Figure 3.9b), the surface albedo varied considerably because land use over this part of the Danish West Coast is quite diverse. Over vegetated areas, the surface albedo increases sharply at about 700–800 nm wavelength leading to increased I_{λ}^{\uparrow} for cloud-free times (43,000–43,120 s) at 810 nm. Following the flight leg over land, the aircraft track led

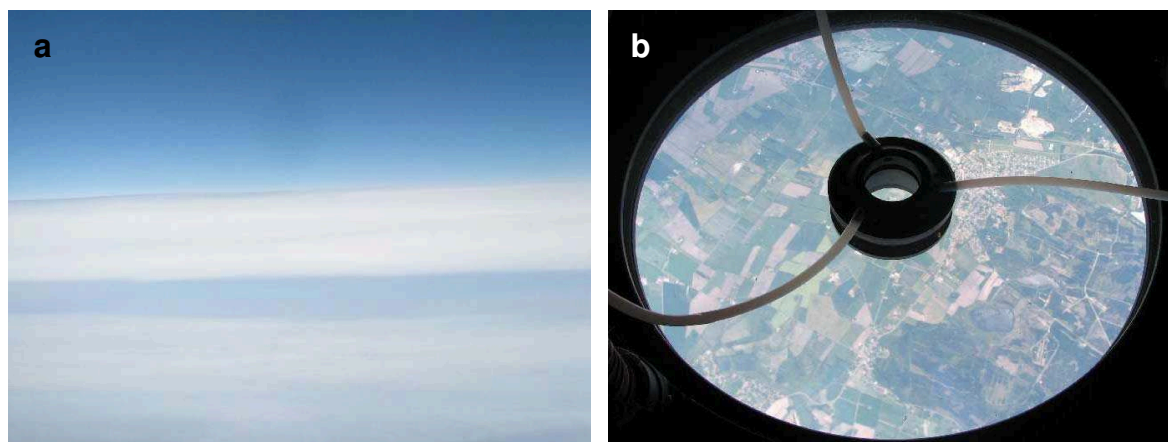


Figure 3.9: Photos of a) the probed cirrus (taken at 43,260 s) and b) of the agriculturally used land on the West Coast of Denmark (taken at 42,950 s) on 22 May, 2007.

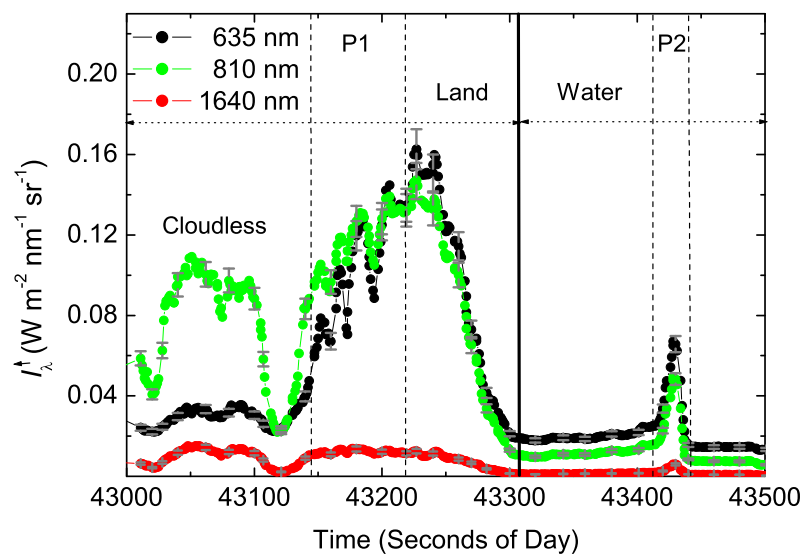


Figure 3.10: Time series of upwelling radiances I_{λ}^{\uparrow} measured with the SMART-Albedometer at different wavelengths for the radiation leg of flight 22 May, 2007 (43,000–43,500 s) over Jutland and the North Sea. Error bars representing measurement- and calibration uncertainties are included. Dashed vertical lines indicate cloud retrieval periods P1 and P2, to the right of the solid black line the aircraft was over the North Sea.

over open water, where the surface albedo is low. Thus I_{λ}^{\uparrow} over an optically very thin cirrus (43,300–43,400 s) is small and does not exceed $0.02 \text{ W m}^{-2} \text{ nm}^{-1} \text{ sr}^{-1}$ at 635 nm wavelength. For a short period over open water for which τ and R_{eff} are retrieved (P2) a thicker patch of cirrus was encountered resulting in a sharp peak in I_{λ}^{\uparrow} .

4 Retrieval Methodology

In this chapter the methodology used for the retrieval of τ and R_{eff} based on measurements of I_{λ}^{\uparrow} at the CIRCLE-2 field experiment is described. In Section 4.1, the radiative transfer model used in combination with the measurements is introduced. The bispectral reflectance technique to determine the cirrus properties is described in Section 4.2.

4.1 Radiative Transfer Model

All spectral radiative calculations in this work were done with the *libRadtran* (*library for Radiative transfer*) radiative transfer package by Mayer and Kylling (2005), using different solvers and options. With *libRadtran*, radiative quantities at user-defined altitudes within the atmosphere are calculated using input data of the extraterrestrial radiation, the (cloudy) atmosphere, and surface properties. If measured input parameters are available, they can be used as input for *libRadtran*, otherwise standard assumptions are applied.

For calculations in the solar spectral range in this part of the study, 1D simulations based on plane-parallel radiative transfer theory were made. The plane-parallel (*i.e.*, horizontally homogeneous) DISORT algorithm by Stamnes et al. (1988a) based on the discrete ordinates method is used as solver of the RTE. The discrete ordinates method uses an even number of discrete "streams" of radiation in each hemisphere, each one representing a different direction (Petty, 2006). The number of streams is constrained by the needed accuracy, it is equal to the number Λ of Legendre polynomials used to describe \mathcal{P} (cf. Section 2.2). In fact, the version 2.0 of DISORT (subsequently referred to as DISORT2) as described in Stamnes et al. (2000) was chosen. This improved algorithm makes use of the forward scattering peak truncation method introduced by Wiscombe (1977) to reduce the required number of streams for accurate radiance calculations to $\Lambda = 16$. For simulations in the IR spectral range the two-stream radiative transfer solver described by Kylling et al. (1995) was used.

4.1.1 Basic Model Input

No radio soundings were available in the vicinity of the probed cirrus. Thus, the midlatitude summer standard atmospheric profiles of temperature, pressure, relative humidity, and trace gas concentrations (ozone, oxygen, carbon dioxide, nitrogen dioxide) from Anderson et al. (1986) were used as meteorological input parameters. The satellite-derived columnar ozone concentration of 335 Dobson Units (DU) obtained from the Ozone Measurement Instrument (OMI) was used to scale the ozone profile. Gas absorption was parameterized by the LOW-TRAN band model (Pierluissi and Peng, 1985) as adopted from SBDART (Ricchiazzi et al.,

1998). Aerosol microphysical properties were described with the model by Shettle (1989). The rural summer aerosol type was chosen for P1 (agricultural area in the west of Denmark) while for P2 (North Sea) the maritime summer aerosol was selected. At $1\ \mu\text{m}$, the rural/-maritime aerosol has an aerosol optical thickness of 0.074/0.11, the respective Ångström exponent α are 0.99/0.63.

As extraterrestrial solar irradiance spectrum the data by Gueymard (2004) was used. The spectral irradiances were interpolated to the wavelength grid of the SMART-Albedometer. The calculated radiation quantities were corrected for the Sun-Earth distance on 22 May, 2007 by specifying this date as Julian day in the *libRadtran* input file. Finally, the option to convolute the output radiative quantities with a normalized Gaussian curve with a FWHM of 3.3 nm to match the spectral resolution of the spectrometer was selected.

4.1.2 Spectral Surface Albedo

The spectral surface albedo is a crucial input to cloud retrieval algorithms which are based on cloud-reflected solar radiation (Rolland et al., 2000), especially for optically thin cirrus above strongly reflecting surfaces. For that reason surface albedo spectra were derived from clear-sky SMART-Albedometer measurements made in the vicinity of the cirrus when possible. As stated in Coddington et al. (2008) the difficulty in deriving surface albedo from aircraft observations lies mainly in the atmospheric correction in which molecular and aerosol scattering and absorption is accounted for. As obvious in Figure 3.8, P1 was preceded by a cloudless part (42,900–43,120 s). For this clear-sky period the mean spectral surface albedo was derived from a nonlinear extrapolation of the surface albedo. The extrapolation algorithm was adapted from Wendisch et al. (2004). While in Wendisch et al. (2004) irradiances were used, here the algorithm was adjusted to spectral radiances I_λ^\uparrow .

As explained in Bierwirth et al. (2009), gas absorption bands in which the measurement signal is strongly attenuated are critical for the surface albedo extrapolation. For that reason, the following bands corresponding to oxygen- and water-vapor absorption bands were excluded from the extrapolation results: 750–775 nm, 890–970 nm, 1080–1170 nm, 1260–1500 nm, 1750–1975 nm. The resulting spectral surface albedo used for the cirrus retrieval simulations of P1 is shown in Figure 4.1. Since no clear-sky period was encountered over water (cf. Figure 3.8), the water albedo for shallow coastal waters with high spectral resolution as determined by Wendisch et al. (2004) was employed in the cirrus retrieval simulations for P2 (cf. Figure 4.1).

In Figure 4.1 the surface albedos derived from seven MODIS bands (Schaaf et al., 2002) at the corresponding locations are also presented. While extrapolated surface albedos are based on short time periods of clear-sky measurements of I_λ^\uparrow , MODIS surface albedo products comprise averages of a 16-day measurement period. Despite this difference, the instantaneous extrapolated spectral surface albedo over land and the MODIS-derived values mostly agree within the error bars of the surface albedo extrapolation. Error bars are based on measurement uncertainty of I_λ^\uparrow . Above open water the MODIS albedo at wavelengths below 1000 nm is smaller than the one with high-spectral resolution. This can partly be explained by windspeed-dependent wave action influencing the surface albedo and by the fact that the

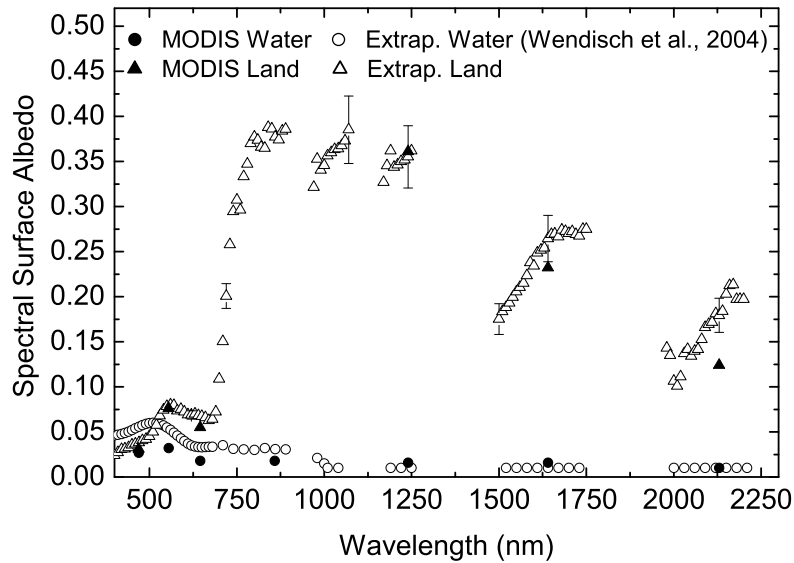


Figure 4.1: Spectral surface albedos of land and water as used in the cloud retrieval for P1 and P2, respectively. Surface albedos obtained from MODIS are also presented.

albedo measurement of Wendisch et al. (2004) was made over the coastal waters of Florida while here the flight track led over the coastal waters of the North Sea. Still, when comparing measured- and modelled I_{λ}^{\uparrow} (above cirrus) assuming the extrapolated water albedo from Wendisch et al. (2004) values were found to agree within the measurement uncertainty of I_{λ}^{\uparrow} and can thereby be used in the cirrus retrieval simulations of P2. In that context, it should be noted that for the wavelength range 600-1650 nm, which is of importance for the cirrus retrieval, the albedo of water is much lower than that of vegetated land surfaces and for that reason less crucial because it contributes much less to I_{λ}^{\uparrow} above the cirrus.

4.1.3 Measured and Modelled Clear-Sky Radiance Spectra

Figure 4.2a shows a one-minute average of measured and modelled I_{λ}^{\uparrow} for the clear-sky part over the land surface before the cirrus encounter. The modelled spectra is based on a *libRadtran* simulation using the extrapolated surface albedo as input. As shown in Figure 4.2b, the agreement between measurement and model simulation is good. percentage differences are mostly less than 1% only at small wavelengths ($\lambda < 500$ nm) as well as in the absorption bands of oxygen and water-vapor they are higher. Besides the absorption band features, the strong increase of I_{λ}^{\uparrow} at wavelengths of 700–800 nm which is typical for vegetated surfaces is obvious in Figure 4.2a.

4.1.4 Optical and Microphysical Cirrus Properties

Ice clouds can be included in the *libRadtran* input by specifying vertical profiles of IWC and R_{eff} . These microphysical properties are converted to optical properties by common

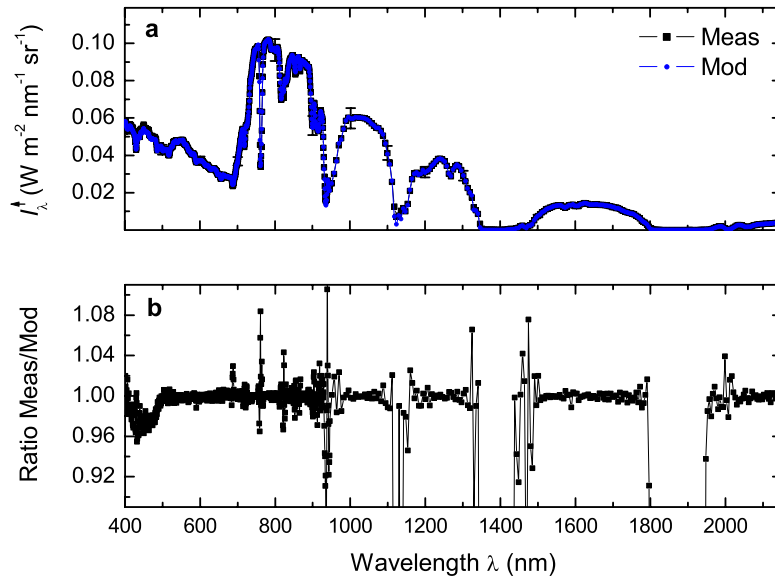


Figure 4.2: (a) Measured (Meas) and modelled (Mod) upwelling radiance spectra for clear-sky conditions over the land surface. The modelled spectrum is based on the retrieved surface albedo. (b) Ratio of measured to modelled spectra.

parameterizations. For calculations made in the solar spectral range, the ice crystal parameterizations (ICP) of Baum et al. (2005b) and Key et al. (2002) were employed. Key et al. (2002) provide single scattering properties for a variety of individual ice crystal habits. Contrarily, Baum et al. (2005b) give optical properties for a size-dependent mixture of crystal habits. However, both determine the shortwave bulk optical properties as function of R_{eff} and IWC .

Ice crystal habits (or shapes) included in the parameterization by Key et al. (2002) are either pristine crystals (hexagonal plates, solid- and hollow columns) or polycrystals (rough aggregates, planar- and spatial rosettes). Aggregates are composed of 2–8 solid hexagonal columns that are attached to each other randomly as shown in Figure 4.3. The parameterization is based on 30 particle number size distributions from midlatitude and tropical cirrus. The database of Key et al. (2002) extends the accurate scattering computations of Yang et al. (2000) that provide an efficient approach to obtain the basic scattering and absorption properties of nonspherical ice crystals. Optical properties of randomly oriented particles are integrated over 56 spectral bands ranging from 0.2–5.0 μm . The scattering phase function $\mathcal{P}(\cos \vartheta)$ is approximated by a double Henyey-Greenstein function. Parameterizations of ice crystal volumetric extinction coefficient b_{ext} , asymmetry parameter g , and single-scattering albedo $\tilde{\omega}$ are provided for each of the mentioned habits. Key et al. (2002) point out that ice clouds are often composed of mixtures of habits and that it would therefore be useful to parameterize the optical properties for mixtures of particle habits. This was realized by Baum et al. (2005b).

The parametrization from Baum et al. (2005b) is a library of optical properties based on more than 1000 particle number size distributions obtained from aircraft in situ measurements in midlatitude and tropical cirrus during various field experiments. Instead of dealing with

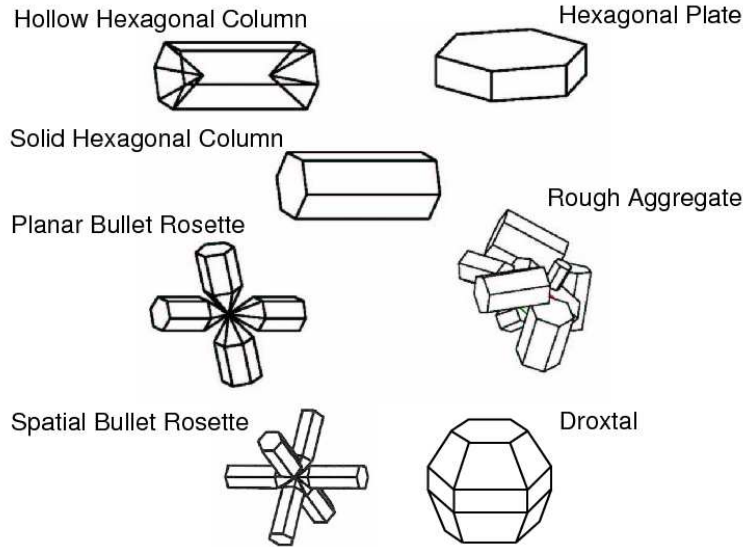


Figure 4.3: Ice crystal habits included in the database of Key et al. (2002) and Baum et al. (2005b).

Table 4.1: Particle habit mix of the cirrus optical property parameterization of Baum et al. (2005b).

Particle maximum dimension D (μm)	Percentage of each habit used
2–60	100 % droxtals
60–1000	15 % spatial bullet rosettes, 50 % solid columns, 35 % plates
1000–2500	45 % hollow columns, 45 % solid columns, 10 % aggregates
2500–9500	97 % spatial bullet rosettes, 3 % aggregates

single particle habits, the optical properties in this parametrization are described for particle-size dependent habit mixtures consisting of droxtals, hexagonal plates, solid columns, hollow columns, aggregates, and spatial bullet rosettes (cf. Figure 4.3). The weight of each habit is based on the particle’s maximum dimension D as presented in Table 4.1. The droxtal has 20 facets and is used to represent small quasi-spherical particles (Yang et al., 2003; Zhang et al., 2004). The library of scattering properties is also based on the scattering calculations of Yang et al. (2000). It covers 234 discrete wavelengths between 0.4 and 13 μm in increments of 0.01 μm /0.05 μm for wavelengths smaller/larger than 2.2 μm . Among others, the database includes properties such as asymmetry parameter g , scattering phase function $\mathcal{P}(\vartheta)$, extinction cross section C_{ext} , and single-scattering albedo $\tilde{\omega}$ over a broad range of particle sizes (maximum dimension $D = 2\text{--}9500 \mu\text{m}$). All properties are averaged over a random orientation of the particle. The operational ice cloud products delivered by MODIS (Platnick et al., 2003) Collection-5 retrievals (King et al., 2006) are based on this ice crystal database. It was recently expanded to the wavelength-range 0.325–100 μm (Baum et al., 2007). However, the far-infrared parameterization is not yet implemented in *libRadtran*.

For radiative transfer calculations in the IR spectral range, the ice crystal optical properties were described using the parameterization by Yang et al. (2005) that covers the wavelength range 3–100 μm . Finally, for reasons of comparison, also spherical ice particles were assumed

Table 4.2: Notations for particle habits. The individual habits that are included in the parameterization of Key et al. (2002) are listed. Mixture refers to the size-dependent mixture of particle habits in the database of Baum et al. (2005b).

Particle habit	Notation
Mixture	<i>mix</i>
Hexagonal plates	<i>plt</i>
Solid columns	<i>scl</i>
Hollow columns	<i>hcl</i>
Rough aggregates	<i>agg</i>
Planar rosettes	<i>rs4</i>
Spatial rosettes	<i>rs6</i>
Ice spheres	<i>sph</i>

in the radiative transfer calculations. The single scattering properties of ice spheres were taken from pre-calculated tables of optical properties based on Mie-theory. They are part of the *libRadtran* software package and are provided for wavelengths between $0.25\ \mu\text{m}$ and $100\ \mu\text{m}$. However, it should be kept in mind that the assumption of large spherical ice particles in natural ice clouds is not realistic. Subsequently, the notations listed in Table 4.2 are used to refer to the different crystal habits.

4.2 Bispectral Reflectance Technique

The classical bispectral reflectance technique was introduced by Twomey and Seton (1980) and Nakajima and King (1990) for the retrieval of cloud optical thickness τ and effective radius R_{eff} of liquid water clouds. A similar approach using measurements of solar radiation reflected by cirrus has been adopted to retrieve cirrus properties (Ou et al., 1993; Rolland et al., 2000; King et al., 2004). This technique is described subsequently.

The retrieval of τ and R_{eff} is based on measured spectral cloud top reflectance r_c at two wavelengths. One wavelength is in the visible to very near-infrared range, where ice is practically non-absorbing ($\tilde{\omega} = 1$), thus r_c is mainly controlled by τ . At this wavelength, r_c increases with τ and asymptotically approaches a value of about unity for optically thick clouds (cf. Figure 4.4a). The other wavelength is positioned in the near-infrared range where ice crystals (and liquid water) absorb solar radiation ($\tilde{\omega} < 1$, cf. Figure 2.2). As illustrated in Figure 4.4b, absorption of solar radiation by solid ice at this wavelength depends strongly on R_{eff} and thus contains information on particle size. r_c at the near-infrared wavelength also increases with τ ; however, its limiting value is significantly less than unity (cf. Figure 4.4a) due to ice (or liquid water) absorption. r_c at the near-infrared wavelength decreases with particle size because $\tilde{\omega}$ increases with particle size (cf. Figure 2.2b). The decrease of r_c at the non-absorbing wavelength with increasing R_{eff} shown in Figure 4.4b is due to the increased forward scattering of larger particles.

The retrieval technique illustrated in Figure 4.5 works as follows: Cloud top reflectance values r_c at both wavelengths are pre-calculated for a number of pairs of τ and R_{eff} for the observed solar geometry and surface albedo. Results are stored in lookup tables (LUT). Measured r_c values are then matched with these LUT. For P1 and P2 timeseries of measured

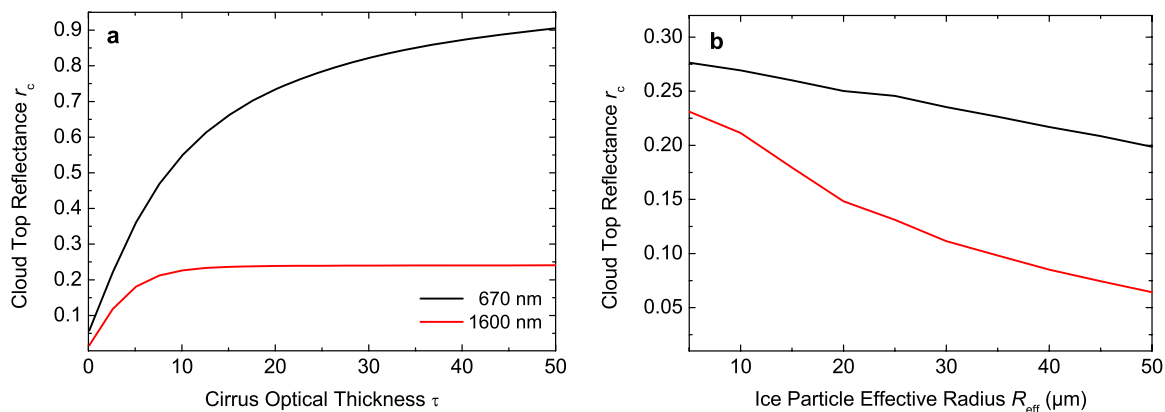


Figure 4.4: Cloud top reflectance r_c versus a) optical thickness τ and b) ice particle effective radius R_{eff} at 670 nm where ice is non-absorbing and 1600 nm where ice absorbs solar radiation. Plots are based on radiative transfer simulations assuming the mixture of ice particle habits (*mix*) which were performed for the general model input of the case study P2 (cf. Table 4.3). In a) calculations were made for $R_{\text{eff}} = 25 \mu\text{m}$, in b) for $\tau = 3$.

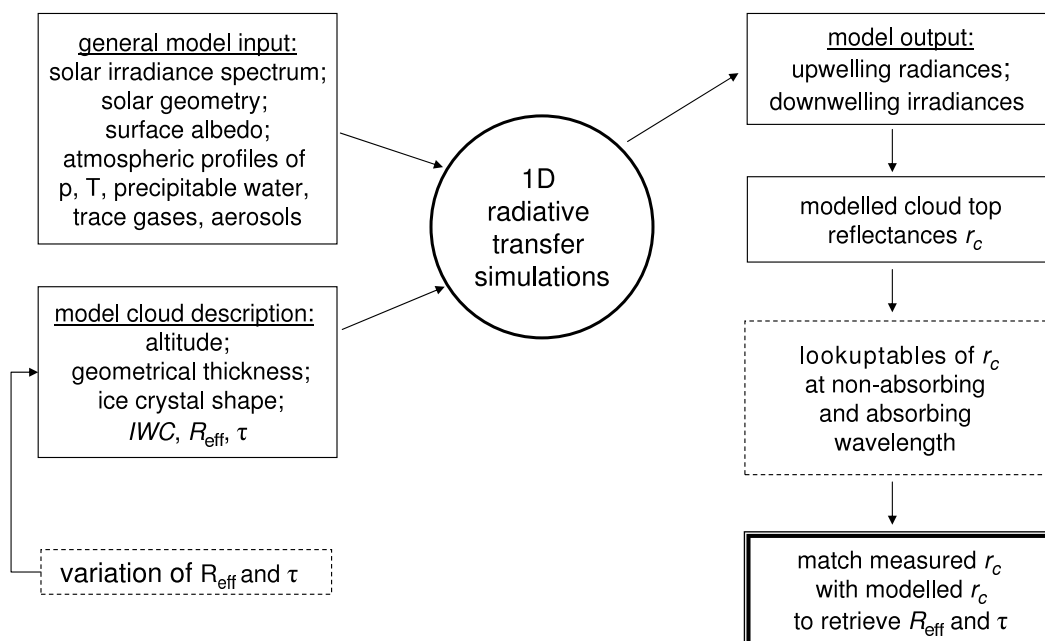


Figure 4.5: Schematic of cirrus retrieval method based on the bispectral reflectance technique.

Table 4.3: Cirrus retrieval input of the two CIRCLE-2 case studies P1 and P2. φ denotes the aircraft heading.

Input parameter	P1	P2
Surface albedo	land (extrapolated)	water
θ_0	36.69°	37.23°
φ_0	14.26°	15.39°
φ	347°	352°
Aerosol profile	rural summer	maritime summer
Cloud base height	8.3 km	8.0 km
Cloud top height	10.4 km	10.6 km
τ	0.1–8.1	0.1–3.6
$\Delta\tau$	0.5	0.5
R_{eff}	5–35 μm	5–35 μm
ΔR_{eff}	5 μm	5 μm

r_c were derived from SMART-Albedometer measurements of I_λ^\uparrow . Therefore, measured I_λ^\uparrow were complemented by calculated downwelling spectral irradiances F_λ^\downarrow at flight level. To quantify the influence of ice particle habit on the retrieval of cirrus τ and R_{eff} , LUTs were calculated separately for each of the ice particle shapes listed in Table 4.2. For P1, LUT calculations were performed for sets of τ ranging from 0.1 to 8.1 and R_{eff} ranging from 5–35 μm (cf. Figure 4.6). LUT for P2 were calculated for sets of $\tau = 0.1$ –3.6 and $R_{\text{eff}} = 5$ –35 μm (cf. Figure 4.7). For both case studies, τ and R_{eff} were varied in steps of $\Delta\tau = 0.5$ and $\Delta R_{\text{eff}} = 5 \mu\text{m}$. An overview of the radiative transfer model input of the two CIRCLE-2 case studies (P1 and P2) is presented in Table 4.3. The model cloud was assumed to be plane parallel and to consist of one cirrus layer.

In the retrieval 0.67 μm was chosen as non-absorbing wavelength and 1.6 μm as absorbing wavelength, these two wavelengths are commonly used in satellite retrievals of cloud properties (Rolland et al., 2000; Platnick et al., 2001). However, in the database of Key et al. (2002), the optical properties are integrated over spectral bands, thus the optical properties are constant for the bands 0.6–0.7 μm and 1.5–1.65 μm . For that reason measured r_c values were also averaged over these two spectral bands for the retrieval.

When varying the ice particle habits while keeping τ and R_{eff} constant, differences of the modelled r_c will result only from differences in the scattering phase function of the applied habits. This effect is illustrated in Figure 4.6 and Figure 4.7 for the LUT assuming *plt*, *scl* and *agg*. The pairs of modelled r_c generate a two-dimensional solution space which is characterized by contours of τ (rather horizontal lines) and R_{eff} (almost vertical lines). Each pair of r_c corresponds to a pair of τ and R_{eff} . Note that the r_c of thin cirrus is influenced by the surface albedo ρ_{surf} and thus influences the shape of the LUT of P1 and P6. Increasing τ (e.g., 0.1–8.1 in Figure 4.6 and 0.1–3.6 in Figure 4.7) results in increasing r_c in the non-absorbing wavelength range 0.6–0.7 μm , while increasing R_{eff} (e.g., 5–35 μm in Figures 4.6 and 4.7) leads to decreasing r_c at the absorbing wavelength range 1.5–1.65 μm . By matching observed r_c value pairs at the non-absorbing and absorbing wavelength range to the best-fitting pair of pre-calculated LUT reflectance pairs time series of τ and R_{eff} were derived. The LUTs were interpolated linearly in order to obtain a finer resolution in τ - and R_{eff} space. Observed r_c are presented by dots in Figures 4.6 and 4.7.

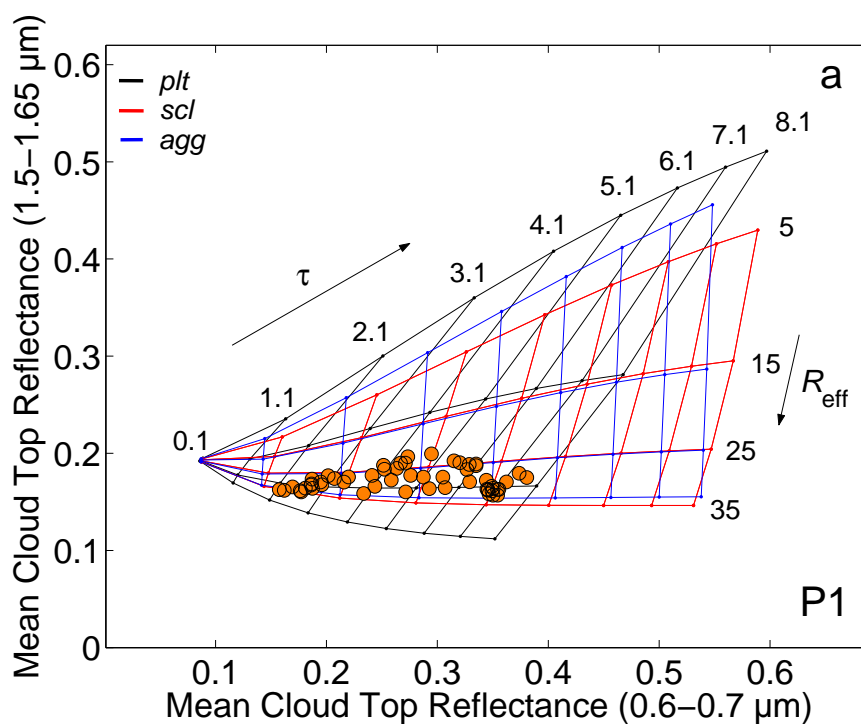


Figure 4.6: Cloud retrieval solution space for three particle habits showing contours of constant τ and R_{eff} (in μm). Observed cloud top reflectances of the first flight on 22 May, 2007 (period 1 (P1), 43,146–43,220 s) over land are represented by dots.

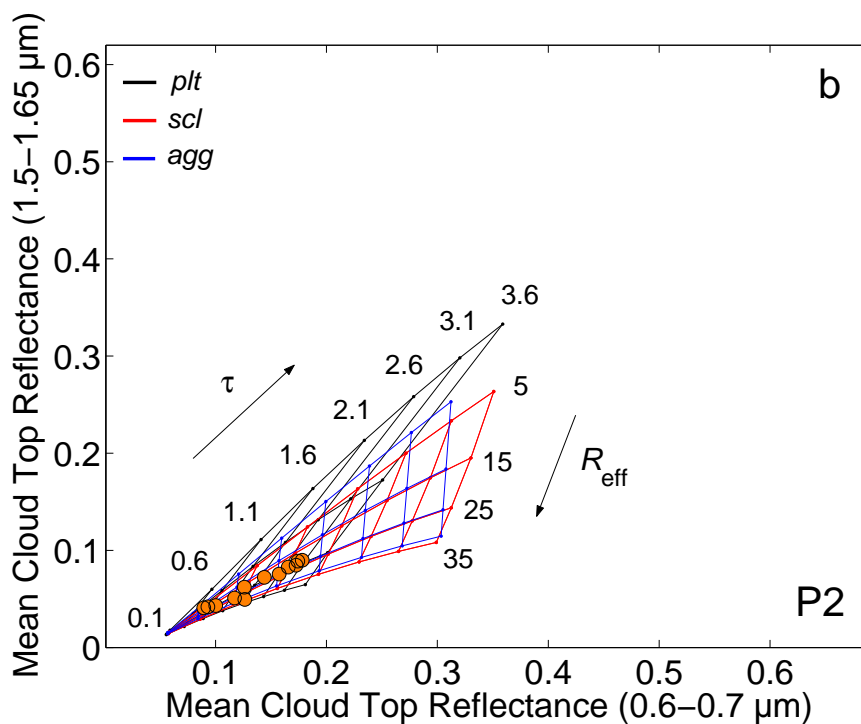


Figure 4.7: Cloud retrieval solution space for three particle habits showing contours of constant τ and R_{eff} (in μm). Observed cloud top reflectances of the first flight on 22 May, 2007 (period 2 (P2), 43,419–43,435 s) above the North Sea are represented by dots.

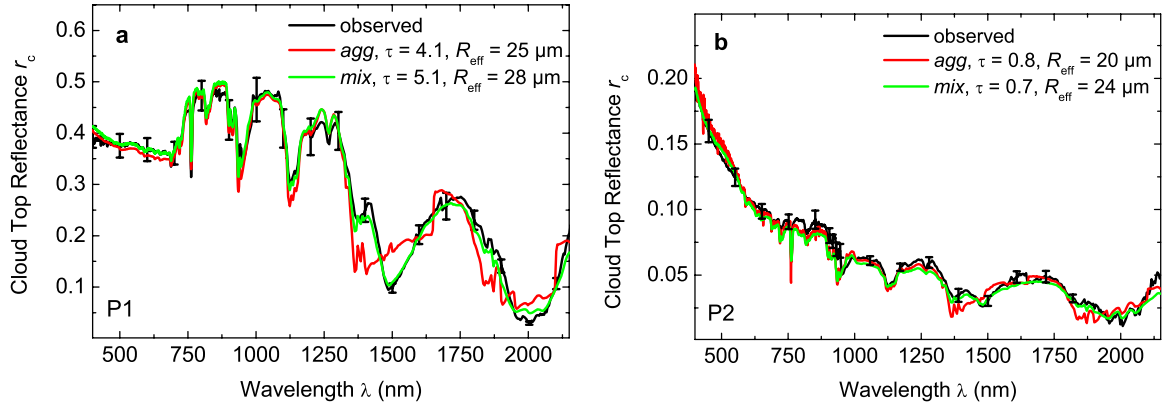


Figure 4.8: Measured and modelled cloud top reflectance r_c versus wavelength. In a) r_c at 43,206 s during P1 is presented while b) shows r_c at 43,420 s during P2. Different y-scales are used.

Figure 4.8 shows measured r_c and their best-fitting modelled counterparts as function of wavelength. Error bars of observed r_c which correspond to errors in measured I_λ^\uparrow (cf. Table 3.2) are indicated. For both of the two case studies, r_c at a certain time is presented (43,206 s for P1, and 43,420 s for P2). Observed r_c are compared to the matched modelled r_c assuming *agg* and *mix*. Compared to P2, the cirrus was optically thicker during P1, thus r_c during P1 is higher than during P2. For the example presented in P1 (cf. Figure 4.8a), a cirrus with $\tau = 4.1$ and $R_{\text{eff}} = 25 \mu\text{m}$ fits best with the observed r_c at 43,206 s when assuming *agg*. Under the assumption of a mixture of particle habits, retrieved τ and R_{eff} amount to 5.1 and $28 \mu\text{m}$, respectively. The observed r_c at 43,420 s during P2 is matched best by a modelled cirrus of $\tau = 0.8$ and $R_{\text{eff}} = 20 \mu\text{m}$ when *agg* are assumed in the model simulations, while using the *mix* leads to a retrieved τ value of 0.7 and a retrieved R_{eff} value of $24 \mu\text{m}$ (cf. Figure 4.8b). The modelled r_c assuming the mixture of particle habits from Baum et al. (2005b) represents the observed r_c well over the entire wavelength range and agrees with the observed r_c within its error bars. Using the ICP of Key et al. (2002) cannot represent all reflectance feature properly (cf. Figure 4.8). This impairment is due to the averaging of the optical properties over wavelength bands in this ice cloud parameterization. However, since the retrieval does not require agreement of measured and simulated r_c over the entire wavelength range, this does not pose a serious problem.

5 Ice Crystal Shape Effects

5.1 Impact of Ice Crystal Habit on Retrieved Properties

In the following, results of the cloud retrieval for the two CIRCLE-2 case studies P1 and P2 are presented. 1D radiative transfer calculations were performed for six different ice crystal shapes described in the ice cloud parameterization by Key et al. (2002), the mixture of ice crystal habits of the parametrization by Baum et al. (2005a), and for ice spheres (cf. Table 4.2).

Statistics and timeseries of the retrieved values are shown in Table 5.2, Table 5.3, and Figure 5.1, respectively. The retrieved results are compared to independent estimates of τ and R_{eff} derived from lidar and microphysical in situ measurements.

The uncertainties of I_{λ}^{\uparrow} are considered in the interpretation of the cloud retrieval results. To estimate the uncertainty of the retrieved values, τ and R_{eff} were retrieved for the I_{λ}^{\uparrow} which was varied in positive and negative direction according to the calibration uncertainty of the I_{λ}^{\uparrow} measurement ($\pm 6\%$ and $\pm 9\%$ at $0.6\text{--}0.7\ \mu\text{m}$ and $1.5\text{--}1.65\ \mu\text{m}$, respectively). As an average over all habits, an error of $\pm 8\%$ and $\pm 9\%$ in τ and R_{eff} , respectively was estimated (cf. Table 5.1).

5.1.1 Cirrus Optical Thickness

The influence of particle habit on cloud top reflectance r_c at non-absorbing wavelengths and thus on retrieved τ as shown in Table 5.2, Table 5.3, and Figure 5.1 can be attributed to differences in the scattering phase functions of different particle shapes. Mean retrieved τ of P1, denoting the part of the cirrus above West Denmark, range from 3.0 for solid columns and rough aggregates to 4.9 for hexagonal plates (cf. Table 5.2). Only spheres yield even larger τ averaging at 5.5. Retrieved τ of all other habits range between the mentioned extreme values. Assuming a mixture of crystal shapes, observed r_c at non-absorbing wavelengths fit best with modelled r_c assuming a cirrus with τ of 3.4 on average. As mentioned in Section 3.2.3, no

Table 5.1: Uncertainties of retrieved τ and R_{eff} due to I_{λ}^{\uparrow} measurement uncertainty and surface albedo variation of 10%.

Induced error in % due to	τ	R_{eff}
I_{λ}^{\uparrow} uncertainty	8	9
Surface albedo variation	3	6

Table 5.2: Retrieved τ and R_{eff} for flight 22 May, 2007 (P1, 43146-43220 s) over land and values derived from lidar- and microphysical measurements (σ , standard deviation).

	τ		$R_{\text{eff}} (\mu\text{m})$	
	Mean	σ	Mean	σ
<i>mix</i>	3.4	1.2	29.7	3.5
<i>plt</i>	4.9	1.7	24.5	1.8
<i>scl</i>	3.0	1.0	29.2	3.4
<i>agg</i>	3.0	1.0	29.7	4.0
<i>hcl</i>	3.7	1.2	23.2	2.4
<i>rs4</i>	3.7	1.2	24.0	2.5
<i>rs6</i>	3.5	1.2	23.6	2.4
<i>sph</i>	5.5	1.9	26.2	3.1
Lidar	(1.9)	(0.4)	-	-
FSSP + CPI	-	-	22	13

Table 5.3: Retrieved τ and R_{eff} for flight 22 May, 2007 (P2, 43419-43435 s) above the North Sea and values derived from lidar- and microphysical measurements (σ , standard deviation).

	τ		$R_{\text{eff}} (\mu\text{m})$	
	Mean	σ	Mean	σ
<i>mix</i>	1.3	0.5	23.2	4.3
<i>plt</i>	2.1	0.8	24.6	3.2
<i>scl</i>	1.2	0.4	20.6	6.1
<i>agg</i>	1.3	0.4	22.6	5.7
<i>hcl</i>	1.6	0.6	18.4	4.7
<i>rs4</i>	1.5	0.5	18.7	4.8
<i>rs6</i>	1.5	0.5	18.4	4.7
<i>sph</i>	2.3	0.9	28.7	3.8
Lidar	1.7	0.6	-	-
FSSP + CPI	-	-	35	15

reliable τ can be derived from lidar measurements for cirrus with $\tau > 2$. For that reason, values are not comparable for P1 where τ derived from r_c are higher than 2.

Comparing retrieved τ values under different crystal shape assumptions for P2 when the cloud was optically thinner leads to similar results as during P1. As presented in Table 5.3, largest values of τ are derived assuming spheres (mean = 2.3), followed by plates (mean = 2.1) while the lower end of the scale of mean τ values is established assuming solid columns (mean = 1.2), rough aggregates, and a mixture of habits (both with means of 1.3). Lidar-derived τ of 1.7 ± 0.6 agree well with the values derived from cloud top reflectance measurements. As a result of the spatial inhomogeneity of the cirrus, the retrieved τ values of one particle habit vary by a factor of about 3–4 during P1 and P2 (cf. Figure 5.1a and b).

With the help of the lidar a crystal shape retrieval might be feasible (cf. Figure 5.1b). During the first half of the short cirrus encounter lidar-derived τ agree with results for solid columns and a mixture of particle habits. During the second half of the timeseries, τ values from lidar measurements are more similar to the assumption of hexagonal plates. Crystal shapes determined from remote sensing methods are only representative for the uppermost cirrus layer where single-scattering dominates. As discussed in Chepfer et al. (2002) and Wendisch et al.

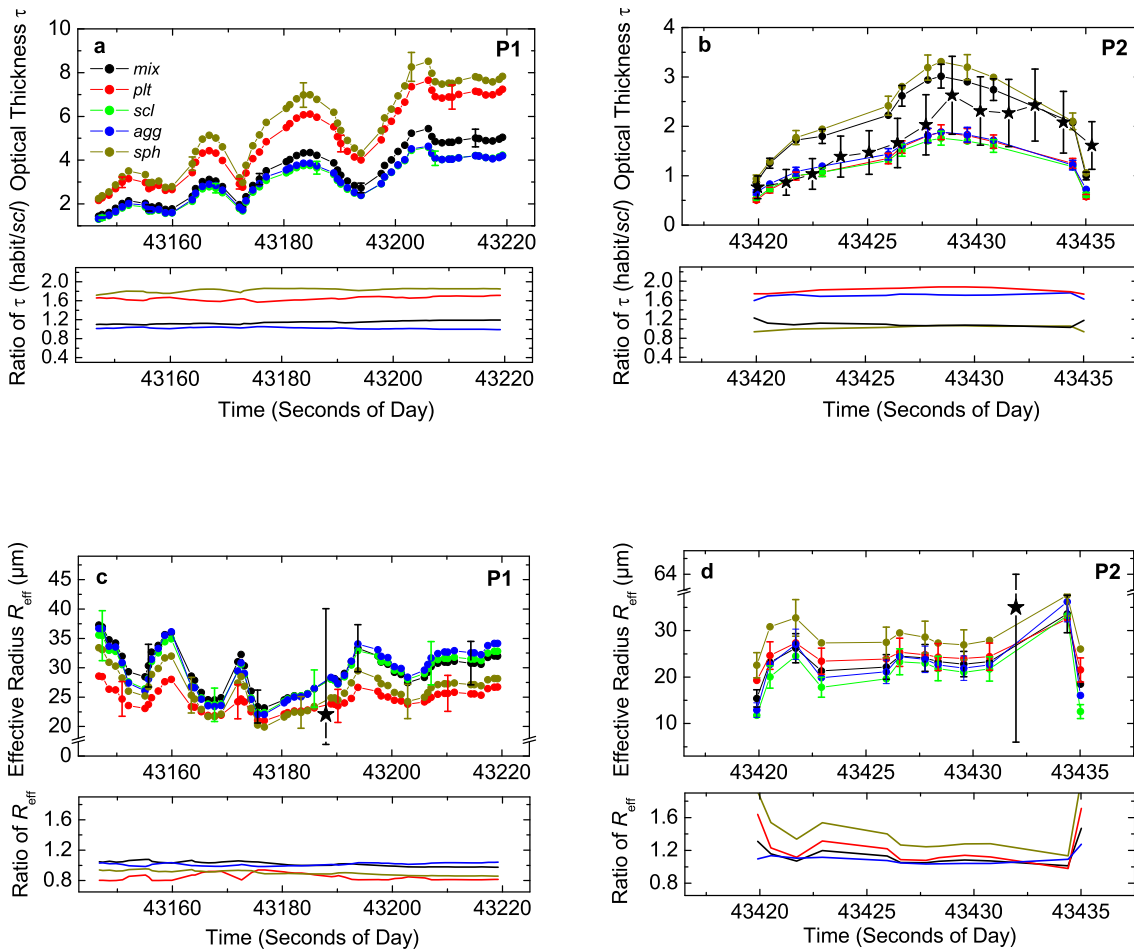


Figure 5.1: Time series of retrieved optical thicknesses τ and effective radius R_{eff} for different ice crystal shape assumptions for flight 22 May, 2007 (period 1 (P1), 43,146–43,220 s) and (period 2 (P2), 43,419–43,435 s). Lidar-derived τ are also shown (for P2) and R_{eff} determined from FSSP+CPI-measurements are indicated (for P1 and P2) by black stars, respectively. Error bars based on measurement uncertainties are included. Different y-scales are used. Ratios of τ and R_{eff} of each habit with respect to *scl* are also shown to illustrate the shape effect.

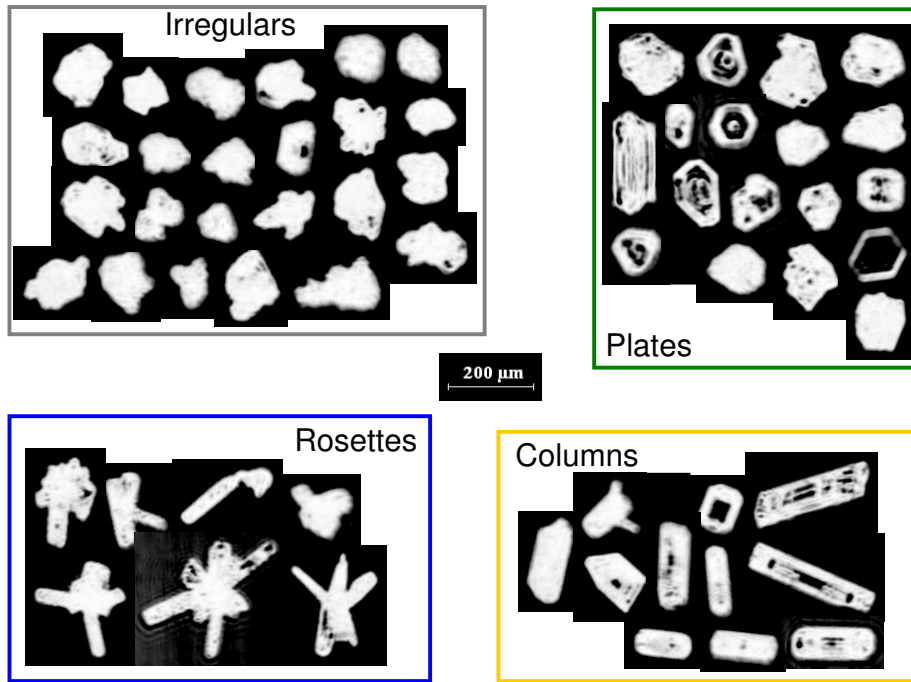


Figure 5.2: CPI images in uppermost in-cloud leg at 9.78 km altitude.

(2005) the differences of scattering phase functions of varying crystal habits diminish due to multiple scattering for $\tau > 2$. For that reason, only comparisons with in situ measurements in the upper parts of the cirrus were made. CPI images in Figures 5.2 and 5.3 show that at the uppermost in-cloud flight leg at 9.78 km a mixture of different ice particle habits was observed: plates, columns, and rosettes are the main distinguishable shapes. However, the contribution of irregularly-shaped particles is dominant (cf. Figure 5.3). This probably results from the fact that the shape of particles smaller than $50 \mu\text{m}$ cannot be confidently determined from the analysis of CPI images (Korolev et al., 1999) and are therefore frequently classified as irregulars. Even though CPI images mostly correctly discriminate large crystals ($R_{\text{eff}} > 50 \mu\text{m}$), it is reasonable to assume that also small crystals of the identified shapes exist. Therefore it is stated that these microphysical measurements of crystal shapes support the findings of the combined retrieval of τ from lidar- and radiance measurements. However, due to the combined uncertainties of lidar- and radiance measurements it is not clear if reliable retrievals of dominant ice crystal shape are feasible.

5.1.2 Ice Particle Effective Radius

Retrieval results of R_{eff} for P1 (cf. Table 5.2) show smallest values assuming hollow columns, rosettes, and plates with mean values of $23\text{--}24.5 \mu\text{m}$. They are about $15\text{--}20\%$ smaller than the values assuming solid columns, rough aggregates, or a mixture of habits for which highest R_{eff} (means around $29\text{--}30 \mu\text{m}$) were retrieved. The assumption of spherical ice particles leads to mean R_{eff} of about $26 \mu\text{m}$. As shown in Figure 5.1c, spatial variations of R_{eff} (about 40%) during the 12 km long flight path of P1 are smaller than variations of τ .

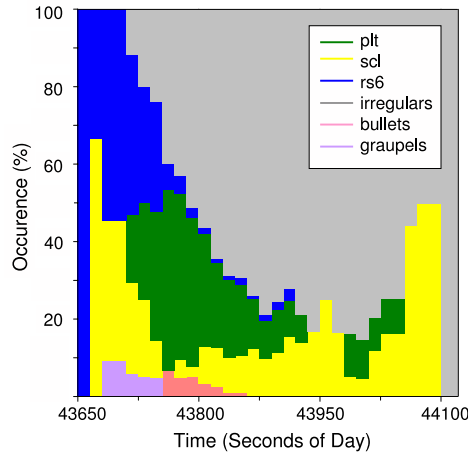


Figure 5.3: Frequency of occurrence of crystal shapes in uppermost in-cloud leg at 9.78 km altitude.

Similar to P1, the results for P2 in Table 5.3 show that smallest R_{eff} were derived assuming hollow columns or rosettes. For these habits, observed r_c fit best with r_c assuming cirrus with R_{eff} of 18–19 μm on average. In contrast to P1, retrieved R_{eff} assuming hexagonal plates with a mean of nearly 25 μm are about 20 % larger than the values retrieved for solid columns (mean = 20.6 μm). Again, mean R_{eff} -values for aggregates and a mixture of particle habits are very similar (means of roughly 23 μm) but slightly higher than the ones of solid columns. Under the assumption of spherical particles, mean retrieved R_{eff} amount to 28.7 μm . During the 3 km flight leg of P2 R_{eff} vary by a factor of three due to spatial cirrus inhomogeneities (cf. Figure 5.1d).

R_{eff} was also determined from microphysical in situ measurements with the FSSP-300 and the CPI. In-cloud flight legs lasting about 10 min each were conducted at four levels (9.78 km, 8.85 km, 8.22 km, and 7.6 km). R_{eff} increased from highest to lowest flight leg with means \pm standard deviations σ of (26 \pm 25) μm , (33 \pm 21) μm , (38 \pm 23) μm , and (44 \pm 30) μm , respectively. Standard deviations are on the order of the mean R_{eff} values indicating strong horizontal inhomogeneity of the probed cirrus. Comparisons of the reflectance-based retrieval results of R_{eff} with the values determined from in situ measurements are prone to some uncertainties and difficulties. Firstly, measurements were not truly collocated. The remote sensing leg in Northwestern direction was followed by the uppermost in-cloud leg towards the Southeast. The time difference between above-cloud flight leg and in-cloud leg of the same geographic location for P1 and P2 was about 12 min and 4 min, respectively. Advection of the inhomogeneous cirrus thus plays a role. Also it should be kept in mind that R_{eff} values retrieved by reflectance-based methods correspond to the upper cloud layers (Platnick, 2000). In addition, the in situ measurements are affected by particle shattering on the instruments thus influencing the R_{eff} based on these microphysical measurements (cf. Section 3.2.3). However, when considering the uncertainties in R_{eff} determined from microphysical measurements (cf. Section 3.2.3) and from cloud top reflectance measurements (see below), R_{eff} determined from both methods agree within their error bars (cf. Table 5.2, Table 5.3, and Figure 5.1). For P1, means and standard deviations of R_{eff} from FSSP+CPI and the cirrus retrieval with different particle habit assumptions are (22 \pm 13) μm and (23–30) \pm (2–4) μm , respectively. Obviously, values agree quite well despite the time lag during which the cirrus

evolved and was advected to the East. For P2, the R_{eff} derived from microphysical measurements averaging at about $(35 \pm 15) \mu\text{m}$ are somewhat higher than the reflectance-based retrieved mean values of $(18\text{--}29) \pm (3\text{--}6) \mu\text{m}$. As mentioned in Chepfer et al. (2005) such discrepancies may be due to both the small time period considered and the spatial inhomogeneity of the cirrus. It was already indicated that spatial variations in R_{eff} of 300% were observed during P2.

5.1.3 Influence of Surface Albedo and Retrieval Mesh Density

As illustrated in Figures 4.6 and 4.7, the shape of the cloud retrieval solution grid strongly depends on surface albedo. For that reason the influence of a surface albedo variation by 10% was tested. As an average over all crystal habits and both periods, the surface albedo variation was found to lead to uncertainties of about 3% and 6% in τ and R_{eff} , respectively as presented in Table 5.1.

The assumption of solid columns and hexagonal plates lead to minimum and maximum retrieved values of τ and considerable differences in retrieved R_{eff} (cf. Tables 5.2 and 5.3). As explained by Francis et al. (1998), the differences are largely due to the higher degree of forward scattering of hexagonal plates compared to columns (cf. Figure 2.3). Also, it should be noted that the location of the data points in the cloud retrieval space, or to be more exact, the mesh density has an influence on the retrieved values. While data points in P1 (cf. Figure 4.6) have relatively big reflectances and are thereby situated in the well-spread part of the τ - R_{eff} -solution space, the observed reflectances in P2 (cf. Figure 4.7) are small and close to the origin of the solution space where constant lines of τ and R_{eff} are very close to each other. This fact in combination with the differing surface albedo in P1 and P2 leading to different shapes of the cloud retrieval solution grid also explains why R_{eff} for hexagonal plates were about 15% smaller in P1 and 20% larger in P2. In addition, as stated in Knap et al. (1999), for optically thick clouds retrieved crystal sizes are less uncertain than for optically thin clouds because for increasing values of τ lines of constant τ and R_{eff} are becoming nearly orthogonal.

5.1.4 Influence of Wavelengths Used in the Retrieval

The question to which extent the wavelengths used in the cirrus retrieval affect the retrieval results is now addressed. The results are summarized in Table 5.4. As described in Platnick et al. (2003), MODIS cirrus retrievals are made at different wavelength combinations. The non-absorbing band is chosen to minimize the impact of the underlying surface. For land and ocean surfaces the bands at $0.65 \mu\text{m}$ and $0.87 \mu\text{m}$ are selected. Moreover, three different bands ($1.6 \mu\text{m}$, $2.1 \mu\text{m}$, and $3.7 \mu\text{m}$) sensitive to ice absorption are used. MODIS products based on three retrievals (of the chosen non-absorbing band in combination with each of the absorbing bands) are available. Since the $3.7 \mu\text{m}$ band is not covered by the I_{λ}^{\uparrow} -measurements with the SMART-Albedometer, the influence of applying a cirrus retrieval at $0.6\text{--}0.7 \mu\text{m}$ in combination with the $2.1\text{--}2.2 \mu\text{m}$ range is tested. As previously mentioned, optical properties of the ice cloud parametrization by Key et al. (2002) are integrated over

Table 5.4: Influence of wavelength combinations used in the cirrus retrieval on τ and R_{eff} . Percentage differences are averages over all particle shapes.

Case study	Wavelengths combinations used in retrieval	Difference in	
		τ (%)	R_{eff} (%)
P1	0.6–0.7 μm + 1.5–1.65 μm ; 0.6–0.7 μm + 2.1–2.2 μm ;	5	30
P2	0.6–0.7 μm + 1.5–1.65 μm ; 0.8–0.9 μm + 2.1–2.2 μm ;	7	5

spectral bands; for that reason mean r_c of the given wavelength ranges are used. For P1 it was found that employing the wavelength range 2.1–2.2 μm resulted in slightly smaller retrieved τ in comparison to using the 1.5–1.65 μm range. As an average over all crystal habits this difference was 5%. This deviation results from the uncertainties in I_λ^\uparrow measurements which propagate in the retrieval. Due to the non-perpendicular shape of the reflectance grid uncertainties of I_λ^\uparrow at ice-absorbing wavelengths cause not only a deviation in the retrieved R_{eff} as expected but also a deviation in τ . The uncertainties of $I_{1.6}^\uparrow$ and $I_{2.1}^\uparrow$ differ with 9.2% and 10.1%, respectively, causing differences of the retrieval results.

On average, retrieved R_{eff} based on r_c at 2.1–2.2 μm are 30% smaller than the ones using r_c at 1.5–1.65 μm (cf. Table 5.4). This can be explained by the fact that due to varying strengths of ice crystal absorption at these different spectral bands, the retrieved R_{eff} are representative for different heights within the cloud. Ice absorption at 2.1–2.2 μm is stronger than at 1.5–1.65 μm hence the 2.1–2.2 μm result corresponds to the very top layer of the cirrus while radiation at 1.5–1.65 μm can penetrate deeper into the cloud. Thus the larger R_{eff} retrieved at 1.5–1.65 μm are in agreement with the cirrus crystal size profile observed by the microphysical in situ measurement showing increasing R_{eff} with decreasing altitude. However, as emphasized in Chang and Li (2003), it is difficult to assign the reflectance-based retrieval results from different wavelengths to any particular cloud level near cloud top. In addition, Platnick (2000) investigated the influence of solar zenith angle on the height within the cloud at which a retrieved R_{eff} is valid. He found that the lower the sun, the shallower the layer into which photons can penetrate thus retrieved R_{eff} at large solar zenith angles correspond to ice particles at higher layers in the cloud than the ones retrieved for smaller solar zenith angles. For P2, the cirrus retrieval was repeated for the non-absorbing wavelength preferred for clouds over water surfaces (0.86 μm , (Knap et al., 1999; Platnick et al., 2003; King et al., 2004)). Using r_c at 0.8–0.9 μm in combination with the 1.5–1.65 μm band resulted τ values differing up to 7% from the ones based on r_c at 0.6–0.7 μm (cf. Table 5.4). This is still within the τ uncertainty range induced by I_λ^\uparrow -measurement uncertainties (cf. Table 5.1) and thereby justifies that we use 0.6–0.7 μm instead as non-absorbing band to retrieve τ . It is concluded that since the surface albedo of water is low at both wavelength ranges (0.6–0.7 μm and 0.8–0.9 μm), differences in retrieved τ are small. Using this second set of wavelengths in the retrieval also has a small impact on R_{eff} of 5% (average over all particle shapes).

The effect of ice crystal habit on the retrieval of cirrus τ and particle R_{eff} for the two CIRCLE-2 case studies which are published in Eichler et al. (2009) can be summarized as follows: The influence of crystal habit on τ is larger than on R_{eff} . Shape-induced percentage differences between retrieved τ may amount up to 70% which is in agreement with McFarlane et al. (2005) and Key et al. (2002) stating differences of up to 50% and 60%, respectively. With

maximum differences in retrieved R_{eff} of about 20 % our results are of the same magnitude as the ones reported by Knap et al. (1999) (11 %) and McFarlane et al. (2005) (30 %). These findings highlight the need for using reasonable crystal habit assumptions in remote sensing retrievals of τ and R_{eff} .

5.2 Impact of Ice Crystal Habit on Cirrus Radiative Forcing

In this Section, the impact of different ice crystal habit assumptions on the cloud radiative forcing of the two CIRCLE-2 case studies P1 and P2 is analyzed. Results are discussed separately for the spectral ($\Delta F_{\lambda}^{\text{sol}}$) and broadband (ΔF^{sol}) solar radiative forcing (cf. Section 5.2.1), the spectral ($\Delta F_{\lambda}^{\text{IR}}$) and broadband (ΔF^{IR}) thermal IR radiative forcing (cf. Section 5.2.2), and the broadband net radiative forcing ΔF^{net} (cf. Section 5.2.3). Instantaneous solar/thermal IR/net cirrus radiative forcings at the observed $\theta_0 = 36^\circ$ were calculated. In addition, the diurnal variation of ΔF^{sol} was determined.

As described in Section 2.1 (especially cf. Eq. 2.10), the cloud radiative forcing $\Delta F(z)$ at altitude z is defined as difference of the net irradiances in cloudy and clear sky conditions. Spectra of downwelling and upwelling irradiances (F_{λ}^{\downarrow} and F_{λ}^{\uparrow}) were modelled with *libRadtran* using the retrieval results from Section 5.1. Calculations were made at top-of-atmosphere (TOA) and below the cirrus at bottom-of-atmosphere (BOA). τ and R_{eff} of the model input ice cloud during P1 and P2 were described by the corresponding time series assuming *mix* presented in Figure 5.1.

At TOA Eq. 2.10 simplifies to

$$\Delta F_{\text{TOA}} = \left[F^{\uparrow}(\text{TOA}) \right]_{\text{clear}} - \left[F^{\uparrow}(\text{TOA}) \right]_{\text{cloudy}} \quad (5.1)$$

because

$$\left[F^{\downarrow}(\text{TOA}) \right]_{\text{cloudy}} = \left[F^{\downarrow}(\text{TOA}) \right]_{\text{clear}}. \quad (5.2)$$

5.2.1 Solar Radiative Forcing

The mean (averaged over the respective flight paths P1 and P2) cirrus spectral solar radiative forcing $\Delta F_{\lambda}^{\text{sol}}$ in units of $\text{W m}^{-2} \text{nm}^{-1}$ at TOA and BOA is illustrated in Figure 5.4 for the particle habits *mix*, *plt*, *scl*, *agg*, and *sph*. Results for *rs4*, *rs6*, *hcl* are not shown in order to not overload the panels. The plot shows that the observed cirrus leads to a negative solar radiative forcing, i.e., a solar cooling of the surface and the atmosphere. This can be attributed to the reflection of incoming solar radiation at the ice cloud resulting in an increased amount of solar radiation escaping to space at TOA as well as to a reduced amount of solar radiation reaching the surface (BOA). The magnitude of the cirrus solar radiative forcing depends on cirrus optical thickness, cloud cover, and solar zenith angle

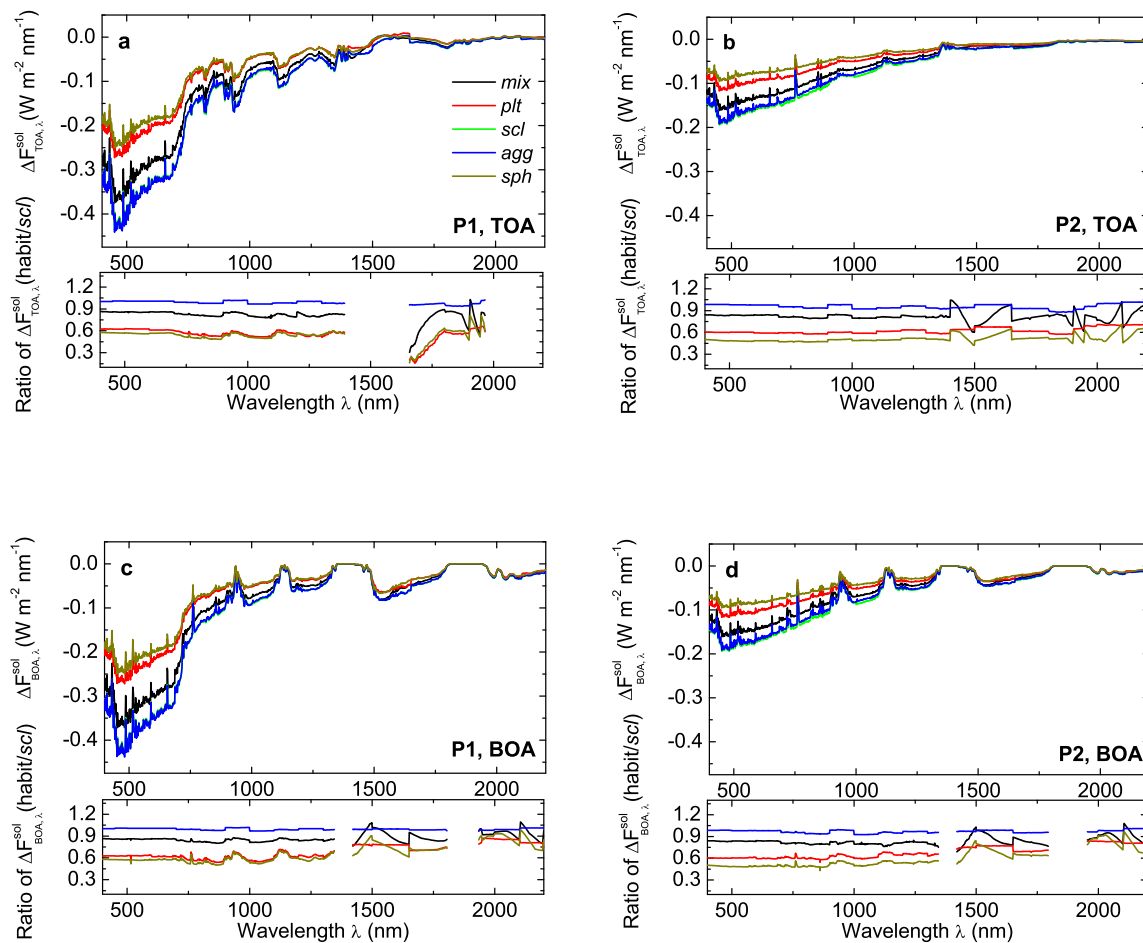


Figure 5.4: Instantaneous spectral solar radiative forcing $\Delta F_{\lambda}^{\text{sol}}$ of the two Circle-2 case studies P1 and P2 for different crystal habits (*mix*, *plt*, *scl*, *agg*, *sph*). Upper panels show $\Delta F_{\lambda}^{\text{sol}}$ at TOA. In the lower panels $\Delta F_{\lambda}^{\text{sol}}$ at BOA is presented. The color code is the same for all four panels. Ratios of $\Delta F_{\lambda}^{\text{sol}}$ of each habit with respect to *scl* are also shown to illustrate the shape effect. Gaps in the ratio plots refer to wavelength ranges in which the ratio could not be determined (division by zero).

Table 5.5: Mean (averaged over P1 and P2) broadband solar radiative forcing in units of W m^{-2} for the assumed ice crystal shapes. Instantaneous ΔF^{sol} at $\theta_0 = 36^\circ$ and diurnal means are presented.

	Instantaneous				Diurnal mean			
	P1		P2		P1		P2	
	$\Delta F_{\text{BOA}}^{\text{sol}}$	$\Delta F_{\text{TOA}}^{\text{sol}}$	$\Delta F_{\text{BOA}}^{\text{sol}}$	$\Delta F_{\text{TOA}}^{\text{sol}}$	$\Delta F_{\text{BOA}}^{\text{sol}}$	$\Delta F_{\text{TOA}}^{\text{sol}}$	$\Delta F_{\text{BOA}}^{\text{sol}}$	$\Delta F_{\text{TOA}}^{\text{sol}}$
<i>mix</i>	-159	-157	-94	-93	-87	-101	-59	-68
<i>plt</i>	-118	-110	-71	-69	-71	-82	-50	-58
<i>scl</i>	-185	-187	-114	-114	-100	-117	-71	-84
<i>agg</i>	-185	-187	-110	-110	-100	-117	-70	-82
<i>hcl</i>	-156	-152	-91	-89	-88	-102	-61	-71
<i>rs4</i>	-154	-150	-90	-88	-88	-102	-61	-71
<i>rs6</i>	-157	-150	-92	-89	-88	-102	-61	-71
<i>sph</i>	-110	-104	-60	-56	-68	-80	-45	-52

(e.g., Stubenrauch et al., 1999; Chen et al., 2000; Futyan et al., 2005). The surface albedo also has an influence on ΔF^{sol} (e.g., Shupe and Intrieri, 2004; Dong et al., 2006).

With a mean optical thickness of 3.4, the cirrus during P1 was optically thicker than during P2 (mean $\tau = 1.3$). Thus, the strongest spectral radiative solar cooling at 500 nm is much higher at P1 than at P2. Strongest solar cooling of $-0.5 \text{ W m}^{-2} \text{ nm}^{-1}$ (P1) and $-0.2 \text{ W m}^{-2} \text{ nm}^{-1}$ (P2) was obtained under the assumption of *scl* and *agg*. $|\Delta F_{\lambda}^{\text{sol}}|$ is largest at small wavelengths where the amount of incoming spectral solar irradiance is greatest and scattering of solar radiation is the dominant process. $\Delta F_{\lambda}^{\text{sol}}$ decreases with increasing wavelengths and at BOA it is approaching a value of zero in the absorption bands of gaseous atmospheric constituents (O_2 at 760 nm, water vapor at 940 nm, 1120–1150 nm, and 1350–1470 nm, CO_2 at 1350–1470 nm, and 1810–1945 nm; cf. Figure 5.4c and d). For the observed cirrus $\Delta F_{\lambda}^{\text{sol}}$ was found to be of the same magnitude at BOA and TOA.

To obtain the solar broadband forcing ΔF^{sol} of the cirrus (in units of W m^{-2}), $\Delta F_{\lambda}^{\text{sol}}$ was spectrally integrated over the considered wavelength range (400–2200 nm). The complete solar range (200–5000 nm) was not covered due to wavelength range limitations in the parameterizations of the cirrus optical properties. However, test calculations showed that the considered wavelength range covers 93% of the solar spectrum, thus the integrated cirrus radiative forcing is a good approximation of the total solar cirrus radiative forcing.

ΔF^{sol} were averaged over the time series of P1 and P2, these mean values of ΔF^{sol} are listed in Table 5.5. With values of about -186 W m^{-2} (P1) and -112 W m^{-2} (P2), the strongest broadband solar radiative cooling at BOA and TOA was obtained under the assumption of *scl* and *agg*, while the smallest solar radiative impact resulted for *plt* and *sph* with values of about -114 W m^{-2} (*plt*) and -107 W m^{-2} (*sph*) in P1 and -70 W m^{-2} (*plt*) and -58 W m^{-2} (*sph*) in P2, respectively (cf. Table 5.5). Assuming *mix* led to a solar radiative forcing of about -158 W m^{-2} (P1) and -93 W m^{-2} (P2) and is thus of the same order as the values obtained assuming *hcl*, *rs4*, and *rs6* (cf. Table 5.5).

Values presented so far denote instantaneous ΔF^{sol} at the observed θ_0 of 36° . In addition, the diurnal variation of ΔF^{sol} were determined for the mean (averaged over P1 and P2, respectively) derived cirrus properties assuming *mix*. For the time between sunrise and sunset (at about 3 UTC and 20 UTC, respectively) on May 22, 2007 at the West coast of

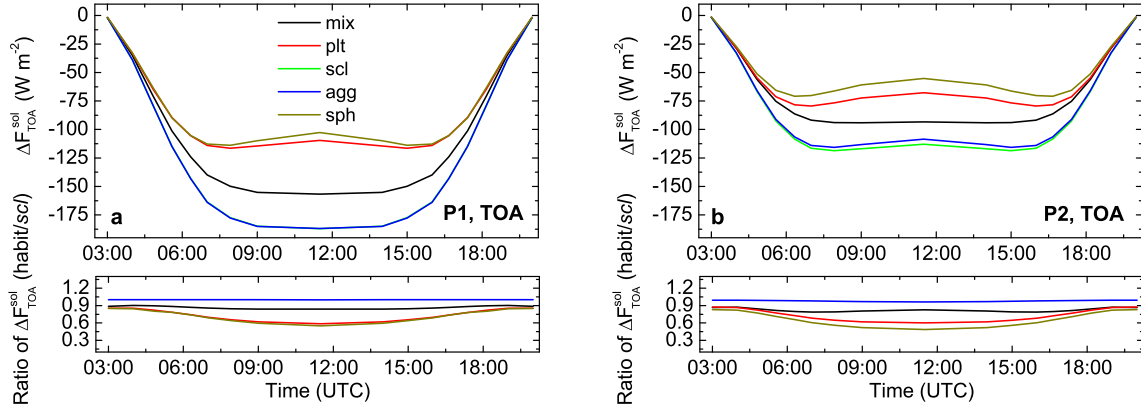


Figure 5.5: Diurnal variation of ΔF^{sol} of the two CIRCLE-2 case studies P1 and P2 for different crystal habits (*mix*, *plt*, *scl*, *agg*, *sph*) at TOA. The color code is the same for both panels.

Denmark (56.5°N , 8.1°E), a set of broadband solar radiative forcing calculations was made by varying the solar zenith angle in steps of $\Delta\mu_0 = 0.1$.

Figure 5.5 shows results for TOA, qualitatively results at BOA are similar and thus not displayed. The diurnal variation of ΔF^{sol} can be explained by a superposition of two effects: The diurnal cycle of the amount of incoming solar radiation and the dependence of the scattering phase function on scattering angle (cf. Figure 2.3). For *plt* (and *sph*) the probability that photons are scattered into an angle $\vartheta \geq 110^\circ$ is reduced compared to other habits. This leads to a smaller $|\Delta F^{\text{sol}}|$ at noon when such scattering angles are observed. Effects of $\mathcal{P}(\vartheta)$ are generally less pronounced at BOA. For P1, diurnal means of ΔF^{sol} range between -80 W m^{-2} (*sph*) and -117 W m^{-2} (*agg*, *scl*) at TOA. At BOA, diurnal averages of $|\Delta F^{\text{sol}}|$ are about 13% smaller than at TOA (cf. Table 5.5). For the optically thinner cirrus observed during P2, averaged diurnal values of $|\Delta F^{\text{sol}}|$ are smallest for *sph* (-45 W m^{-2} at BOA and -52 W m^{-2} at TOA). Largest diurnal averages of $|\Delta F^{\text{sol}}|$ were observed for *scl* with values of -71 W m^{-2} at BOA and -84 W m^{-2} at TOA. The obtained values are within the ranges given in previous publications (e.g., Chen et al., 2000; Mace et al., 2006a; Dupont and Haeffelin, 2008). Chen et al. (2000) found global mean values of $\Delta F_{\text{BOA}}^{\text{sol}}$ of -22 W m^{-2} for cirrus and -80 W m^{-2} for cirrostratus while Dupont and Haeffelin (2008) analyzed a 23-day midlatitude overcast cirrus dataset and measured $\Delta F_{\text{BOA}}^{\text{sol}}$ ranging between $+40 \text{ W m}^{-2}$ and -350 W m^{-2} .

The crystal shape effect on the instantaneous $\Delta F_{\lambda}^{\text{sol}}$ is shown in Figure 5.4 as ratio of $\Delta F_{\lambda}^{\text{sol}}$ of each habit with respect to *scl* (having the strongest solar radiative forcing). For P1 and P2, the shape effect was found to be on the same order, with a slightly more pronounced shape effect (3% as average over all crystal shapes) for the optically thinner cirrus in P2. The influence of ice crystal shape leads to differences in instantaneous $\Delta F_{\lambda}^{\text{sol}}$ (and ΔF^{sol}) of up to 38% (*plt*) and 46% (*sph*). These percentage differences are higher than the 26% reported by Wendisch et al. (2005). However, in Wendisch et al. (2005) ΔF^{sol} of a cirrus with a higher optical thickness ($\tau = 7$) was analyzed. There, multiple scattering which smoothes out differences in the scattering properties of the various ice crystal shapes is more

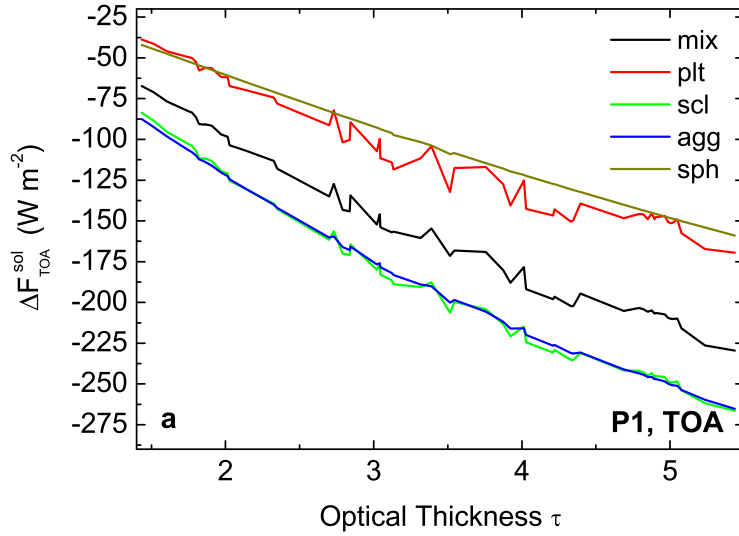


Figure 5.6: Instantaneous broadband solar radiative forcing ΔF^{sol} of the CIRCLE-2 case study P1 for different crystal habits (*mix*, *plt*, *scl*, *agg*, *sph*) versus cirrus optical thickness τ at TOA.

important resulting in smaller shape effects on ΔF^{sol} .

Wendisch et al. (2005) studied the influence of θ_0 on ΔF^{sol} and found the shape effect decreases with increasing θ_0 . Similar findings are reported by Wyser (1999). This behaviour is also illustrated here in the lower panels of Figure 5.5. At local noon (small values of θ_0) the shape effect on ΔF^{sol} is greatest (up to 46%). It gradually decreases with increasing θ_0 until sunset when maximum shape effects were on the order of 15%. This behaviour is explained by multiple scattering which is dominant at larger solar zenith angles when photon path lengths in the cirrus are increased.

A way to quantify the dependence of the instantaneous solar cirrus radiative forcing on cirrus optical thickness is by determining the solar forcing efficiency $S\Delta F^{\text{sol}}$ (Redemann et al., 2006). For a linear dependence between ΔF^{sol} and τ (cf. Figure 5.6), $S\Delta F^{\text{sol}}$ can be determined from the slope of the linear least squares regression line of ΔF^{sol} against τ :

$$S\Delta F^{\text{sol}} = \frac{\partial(\Delta F^{\text{sol}})}{\partial(\tau)}. \quad (5.3)$$

For P1 and P2 at BOA and TOA the correlation coefficient for the linear fit for ΔF^{sol} with τ as regressor is 0.98–0.99 (depending on crystal habit). Values of the instantaneous $S\Delta F^{\text{sol}}$ are listed in Table 5.6. For both P1 and P2, values of the instantaneous $S\Delta F^{\text{sol}}$ at BOA and TOA are of the same magnitude. For P1, the increase of instantaneous $|\Delta F^{\text{sol}}|$ per τ increase of one ranges between -29 W m^{-2} (*sph*) and -45 W m^{-2} (*scl* and *agg*). For P2, an increase of τ by one results in an increase of $|\Delta F^{\text{sol}}|$ between -44 W m^{-2} (*sph*) and -83 W m^{-2} (*scl* and *agg*). The effect of different crystal shape assumptions on instantaneous $S\Delta F^{\text{sol}}$ can be up to 34% for P1 and 48% for P2, differences are greatest between *sph* or *plt* and *scl* or *agg*.

Table 5.6: Broadband solar radiative forcing efficiencies $S\Delta F^{\text{sol}}$ in units of W m^{-2} of the case studies P1 and P2 and all assumed ice crystal shapes. Instantaneous $S\Delta F^{\text{sol}}$ at $\theta_0 = 36^\circ$ and diurnal means are presented.

	Instantaneous				Diurnal mean			
	P1		P2		P1		P2	
	$S\Delta F_{\text{BOA}}^{\text{sol}}$	$S\Delta F_{\text{TOA}}^{\text{sol}}$	$S\Delta F_{\text{BOA}}^{\text{sol}}$	$S\Delta F_{\text{TOA}}^{\text{sol}}$	$S\Delta F_{\text{BOA}}^{\text{sol}}$	$S\Delta F_{\text{TOA}}^{\text{sol}}$	$S\Delta F_{\text{BOA}}^{\text{sol}}$	$S\Delta F_{\text{TOA}}^{\text{sol}}$
<i>mix</i>	-38	-39	-70	-69	-17	-18	-37	-41
<i>plt</i>	-31	-31	-52	-50	-14	-16	-29	-32
<i>scl</i>	-42	-45	-82	-83	-17	-19	-41	-46
<i>agg</i>	-42	-45	-81	-82	-17	-19	-41	-46
<i>hcl</i>	-38	-39	-69	-68	-16	-18	-37	-41
<i>rs4</i>	-38	-39	-69	-67	-16	-18	-36	-40
<i>rs6</i>	-38	-39	-69	-67	-16	-18	-36	-40
<i>sph</i>	-30	-29	-47	-44	-14	-15	-28	-31

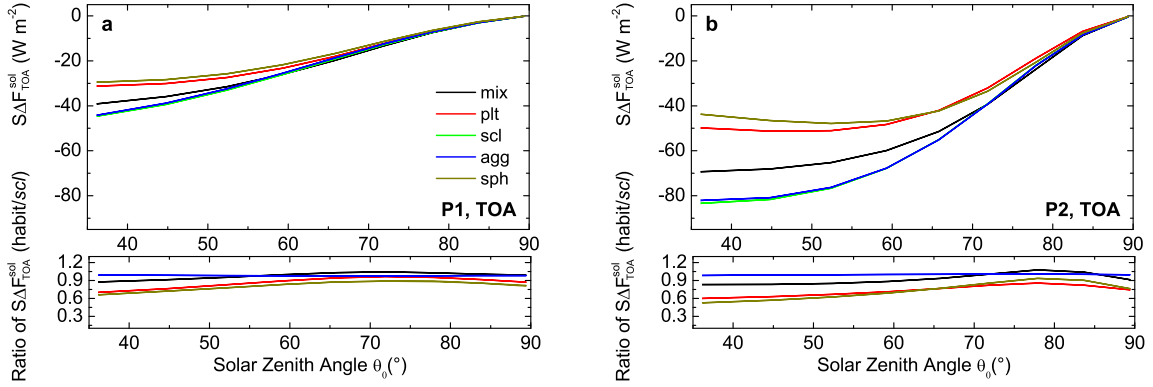


Figure 5.7: Variation of the solar forcing efficiency $S\Delta F^{\text{sol}}$ of the two CIRCLE-2 case studies P1 and P2 for different crystal habits (*mix*, *plt*, *scl*, *agg*, *sph*) at TOA. The color code is the same for both panels.

With $S\Delta F^{\text{sol}}$ the solar radiative effect of the observed cirrus over land (P1) and water (P2) can be compared quantitatively. Depending on ice particle shape, the instantaneous solar radiative cooling of the cirrus over the dark water surface is about 33–47% stronger than over land (for the same τ). The influence of surface albedo on $S\Delta F^{\text{sol}}$ is smallest for *sph* and *plt* and largest for *scl* and *agg*.

The diurnal variation of $S\Delta F^{\text{sol}}$ was determined in radiative transfer calculations with variations of θ_0 between 36° and 89° in steps of $\Delta\mu_0 = 0.1$. Results are shown in Figure 5.7 as function of solar zenith angle θ_0 . $|S\Delta F^{\text{sol}}|$ is largest for small θ_0 when the amount of incoming solar radiation is largest and decreases with increasing θ_0 (setting sun). Diurnal means of $S\Delta F^{\text{sol}}$ are presented in Table 5.6. For both P1 and P2, $S\Delta F^{\text{sol}}$ at BOA are about 10% smaller than at TOA. Diurnal averages of $S\Delta F^{\text{sol}}$ at TOA during P1 range between -15 W m^{-2} (assuming *sph*) and -19 W m^{-2} (assuming *scl* or *agg*). Thus, for the diurnal average the maximum shape effect is decreased to 22%. Over water (P2), the diurnal average of $S\Delta F^{\text{sol}}$ at TOA amounts to values between -31 W m^{-2} (assuming *sph*) and -46 W m^{-2}

leading to maximum shape effects of 32 % which are thus also much smaller than the instantaneous shape effects at noon. As a diurnal mean, the percentage differences in $S\Delta F^{\text{sol}}$ over land and water are even stronger, they range between 50 % for *plt* and 60 % for *agg*. This fact clearly shows that the solar radiative effect of a cirrus also depends on surface albedo as mentioned by Dong et al. (2006). Dupont and Haeffelin (2008) report values of $S\Delta F^{\text{sol}}$ at BOA of -80 W m^{-2} to -100 W m^{-2} . These values are larger than the ones observed for the CIRCLE-2 case studies. However, Dupont and Haeffelin (2008) do not specify for which solar zenith angles their values were determined for.

5.2.2 Thermal Infrared Radiative Forcing

Cirrus absorb thermal IR radiation emitted by the surface and the lower (warmer) atmosphere and emit EM radiation to space and back towards the surface as a function of cloud temperature and cloud optical thickness. Thus two facts are of importance: On the one hand, the IR emission to space in the presence of cirrus is lower than in clear sky conditions because the ice clouds emit at lower temperatures than the surface which results in a warming of atmosphere and surface. On the other hand, the emitted radiation which is directed downwards leads to a warming of the surface. The strength of the thermal IR radiative forcing depends on two factors: the altitude of the cirrus (and thus its temperature) as well as its optical thickness τ (*e.g.*, Shupe and Intrieri, 2004; Wendisch et al., 2007). The higher the cirrus is situated in the atmosphere, the colder is its environment and thus the less thermal IR radiation it emits. For the observed cirrus, the temperature at cloud bottom and -top was -22°C and -47°C , respectively while the surface temperature during P1 (land) and P2 (North Sea) amounted to 18°C and 11°C , respectively. For a cirrus with small τ , more thermal IR radiation from below the cloud can penetrate it, thus the thermal IR radiative forcing is smaller than for a cirrus with large τ which absorbs more upwelling IR radiation. In summary, an optically thick and high (cold) cirrus is expected to have the strongest thermal IR radiative forcing.

The mean (averaged over the respective flight legs P1 and P2) instantaneous spectral thermal IR radiative forcing $\Delta F_\lambda^{\text{IR}}$ in units of $\text{W m}^{-2} \mu\text{m}^{-1}$ was calculated for the crystal habits for which optical properties were available for the entire thermal IR range: *plt*, *scl*, *agg*, *hcl*, *rs4*, and *sph*. Results are illustrated in Figure 5.8. However, in the plots only results for the wavelength-range 3–30 μm are shown because for larger wavelengths, $\Delta F_\lambda^{\text{IR}}$ was neglectable. As in Figure 5.4, results for *rs4*, *rs6*, *hcl* are not shown. Mean values were derived by averaging of $\Delta F_\lambda^{\text{IR}}$ over the time series of P1 and P2. The broadband instantaneous thermal IR forcing ΔF^{IR} (in units of W m^{-2}) was obtained via spectral integration of $\Delta F_\lambda^{\text{IR}}$ over the thermal IR wavelength range (3–100 μm).

Several results are obvious in Figure 5.8: Firstly, values of $\Delta F_\lambda^{\text{IR}}$ are always positive, thus showing that in the thermal IR range, the cirrus is warming the atmosphere and the surface as discussed above. Secondly, when comparing P1 and P2, $\Delta F_\lambda^{\text{IR}}$ of P1 is larger (at TOA and BOA) which is attributed to the higher optical thickness of the cirrus during P1. Thirdly, for P1 and P2, $\Delta F_\lambda^{\text{IR}}$ at TOA is higher than at BOA. The observed cirrus only has a small impact on the thermal IR radiation at the surface because it is situated too high in the atmosphere.

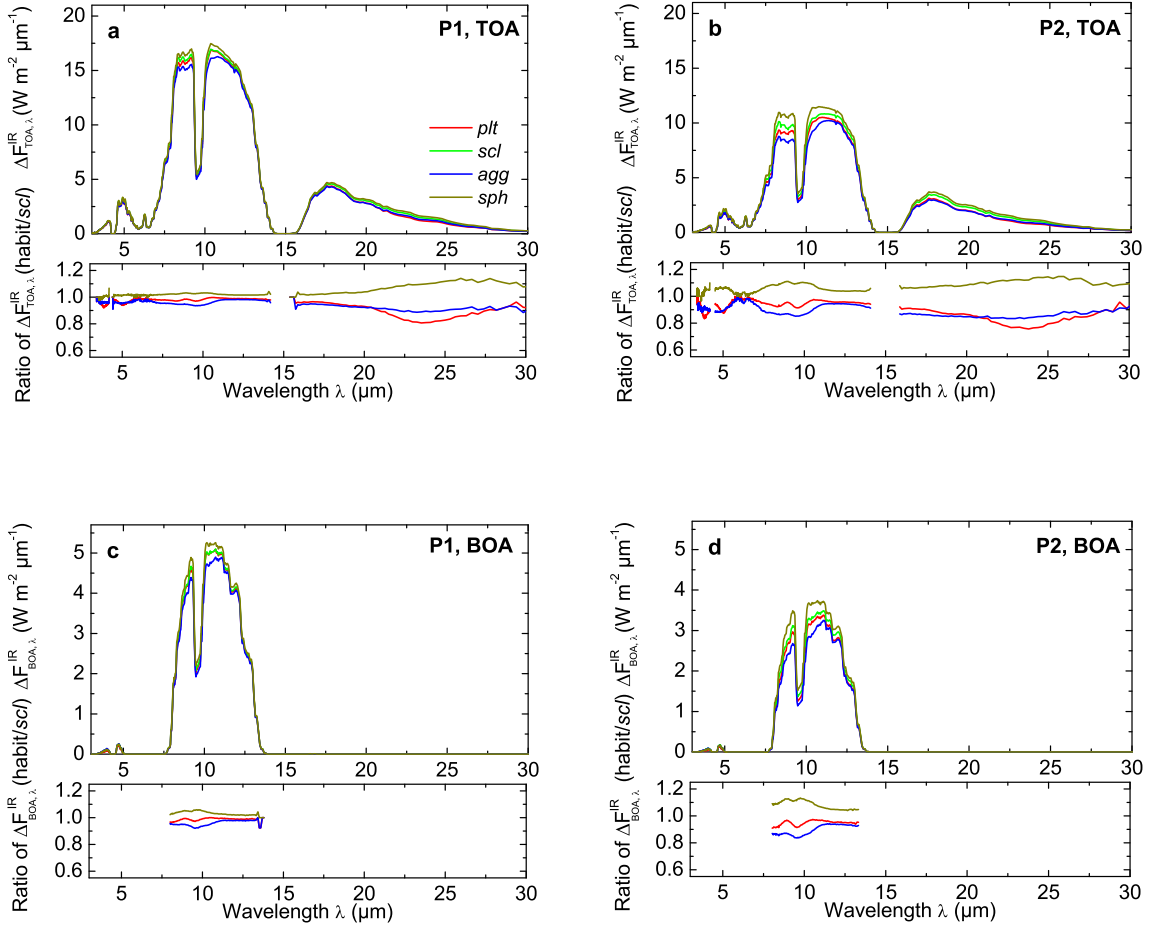


Figure 5.8: Instantaneous spectral IR radiative forcing $\Delta F_{\lambda}^{\text{IR}}$ of the two CIRCLE-2 case studies P1 and P2. Upper panels show $\Delta F_{\lambda}^{\text{IR}}$ at TOA. In the lower panels $\Delta F_{\lambda}^{\text{sol}}$ at BOA is presented. The color code is the same for all four panels. The habit *mix* is not considered because the optical properties are not provided for the IR wavelength range. Ratios of $\Delta F_{\lambda}^{\text{sol}}$ of each habit with respect to *scl* are also shown to illustrate the shape effect. Gaps in the ratio plots refer to wavelength ranges in which the ratio could not be calculated (division by zero). Different y-scales are used for BOA and TOA.

Table 5.7: Instantaneous (averaged over the respective flight legs P1 and P2) broadband thermal IR radiative forcing in units of W m^{-2} for the assumed ice crystal shapes.

	P1		P2	
	$\Delta F_{\text{BOA}}^{\text{IR}}$	$\Delta F_{\text{TOA}}^{\text{IR}}$	$\Delta F_{\text{BOA}}^{\text{IR}}$	$\Delta F_{\text{TOA}}^{\text{IR}}$
<i>plt</i>	19	112	13	73
<i>scl</i>	19	115	13	79
<i>agg</i>	19	110	12	71
<i>hcl</i>	19	113	13	75
<i>rs6</i>	19	112	12	73
<i>sph</i>	20	119	14	85

Instead, the downwelling thermal IR irradiance at BOA is dominated by the emission of thermal IR radiation by water vapor in the lower troposphere (Shupe and Intrieri, 2004). Within the so-called atmospheric window (8–12 μm), the gaseous atmospheric constituents do not absorb or emit much thermal IR radiation. For that reason, the $\Delta F_{\lambda}^{\text{IR}}$ is highest in that spectral region. The atmospheric window is interrupted by an absorption band of O_3 at 9.6 μm which leads to a decrease of $\Delta F_{\lambda}^{\text{IR}}$. The absorption within the other major gas absorption bands is even stronger, thus the thermal IR radiative forcing is close to zero at 4.3 μm (CO_2), 6.3 μm (water vapor) and 15 μm (CO_2).

The instantaneous mean broadband thermal IR radiative forcing of P1 and P2 at TOA and BOA is presented in Table 5.7. With values of around 114 W m^{-2} , $\Delta F_{\text{TOA}}^{\text{IR}}$ is six times higher than the cirrus-induced warming at BOA averaging at 19 W m^{-2} during P1. For P2, the result is similar but with a lower absolute warming of about 76 W m^{-2} at TOA and 13 W m^{-2} at BOA. These findings are in agreement with the results of Dupont and Haefelin (2008) giving a range of $-6 - +30 \text{ W m}^{-2}$ for $\Delta F_{\text{BOA}}^{\text{IR}}$ based on a 23 days midlatitude cirrus data set. Similar values were observed by Mace et al. (2006a) at the Atmospheric Radiation Measurement Program (ARM) Southern Great Plains (SGP) site during the year 2000. They analyzed $\Delta F_{\text{TOA}}^{\text{IR}}$ and found it to amount to $29 - 107 \text{ W m}^{-2}$, depending on cirrus optical thickness.

Compared to the solar wavelength range, the crystal shape effect in the thermal IR spectral region is much smaller and strongly depends on τ . Differences in mean $\Delta F_{\text{TOA}}^{\text{IR}}$ (with respect to *scl*) amount to about 5% (P1) and 11% (P2) on maximum. Thus, the shape effect is more important for the optically thinner cirrus observed during P2. At BOA the spectrally averaged differences are slightly less because they only play a role in the atmospheric window (cf. Figure 5.8) and have maximum values of 4% (P1) and 10% (P2). In general, the largest broadband thermal IR radiative forcing was obtained under the assumption of ice spheres, smallest warming resulted when assuming *agg*.

5.2.3 Broadband Net Radiative Forcing

Instantaneous broadband net radiative forcings ΔF^{net} were obtained by adding respective ΔF^{sol} and ΔF^{IR} . The results are presented in Figure 5.9 and Table 5.8. At BOA the net forcing is mainly driven by the solar radiative forcing because the thermal IR forcing is

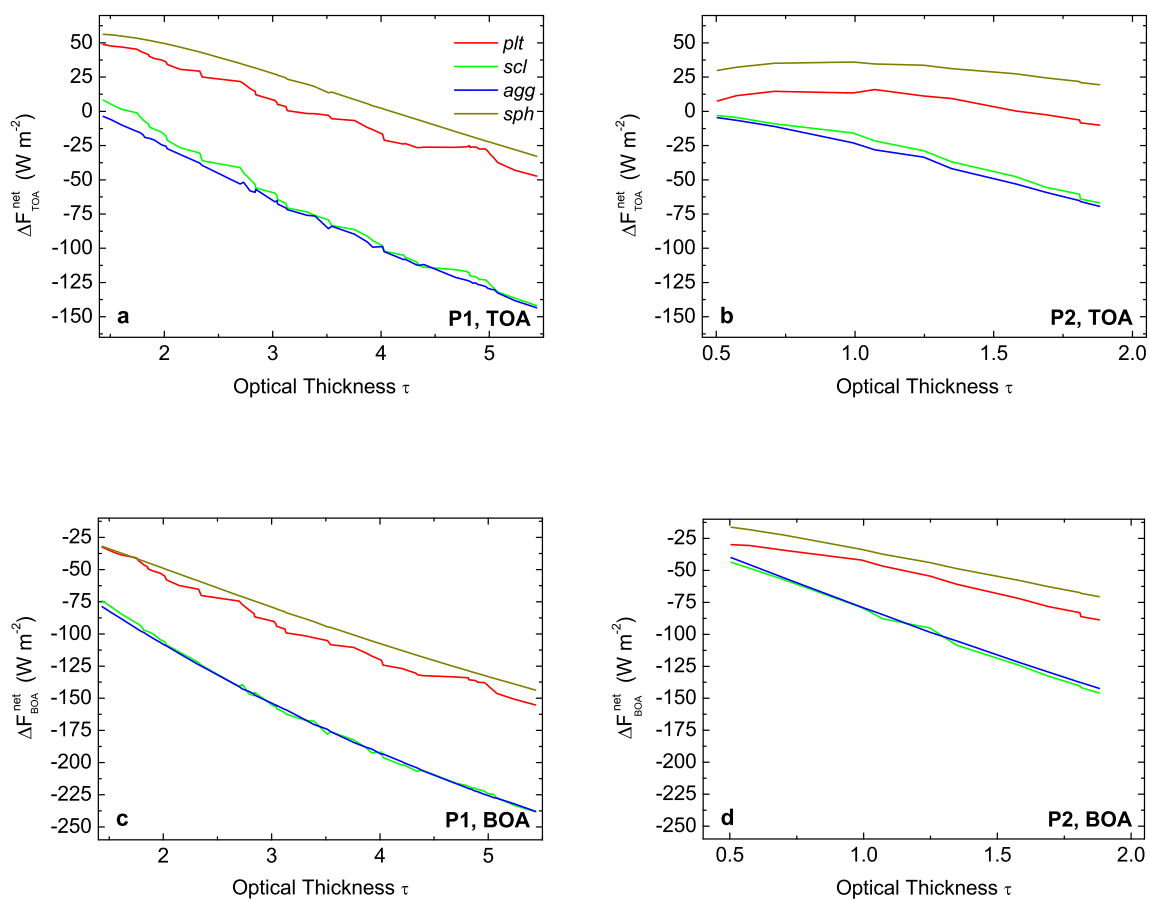


Figure 5.9: Instantaneous broadband net cirrus radiative forcing ΔF^{net} of the two CIRCLE-2 case studies P1 and P2 versus τ . Upper panels show ΔF^{net} at TOA. In the lower panels ΔF^{net} at BOA is presented. The color code is the same for all four panels. Different x-scales are used for P1 and P2.

Table 5.8: Instantaneous mean broadband net radiative forcing in units of W m^{-2} of the case studies P1 and P2 for the assumed ice crystal shapes.

	P1		P2	
	$\Delta F_{\text{BOA}}^{\text{net}}$	$\Delta F_{\text{TOA}}^{\text{net}}$	$\Delta F_{\text{BOA}}^{\text{net}}$	$\Delta F_{\text{TOA}}^{\text{net}}$
<i>plt</i>	-99	2	-59	5
<i>scl</i>	-166	-72	-100	-34
<i>agg</i>	-166	-77	-98	-38
<i>hcl</i>	-137	-39	-79	-13
<i>rs6</i>	-138	-40	-80	-16
<i>sph</i>	-90	15	-46	29

small. Thus the cirrus observed during P1 and P2 was found to have a cooling effect at BOA. For P1, $\Delta F_{\text{BOA}}^{\text{net}}$ ranged between $-90 - -166 \text{ W m}^{-2}$, for P2 between $-46 - -100 \text{ W m}^{-2}$. The strongest surface cooling was observed for *scl* and *agg* while the least cooling was obtained assuming *plt* and *sph*. The crystal shape effect led to differences in $\Delta F_{\text{BOA}}^{\text{net}}$ of up to 40 % (*plt*) and 46 % (*sph*) during P1 and 41 % (*plt*) and 55 % (*sph*) during P2, respectively. The dependence of $\Delta F_{\text{BOA}}^{\text{net}}$ on τ is illustrated in Figure 5.9. The thicker the cirrus, the stronger is its cooling effect. In this plot, deviations from a straight line result from varying R_{eff} observed at the different τ .

While at BOA a strong cooling was observed for all crystal shape assumptions, at TOA the net radiative forcing was found to change its sign depending on crystal habit and τ . The mean $\Delta F_{\text{TOA}}^{\text{net}}$ assuming *plt* and *sph* was slightly positive (thus leading to a warming effect) while it was negative (cooling) for the other crystal shape assumptions (cf. Table 5.8). Similar results were found by Wendisch et al. (2007). Closer analysis showed, that *plt* and *sph* can also lead to a cooling effect: As illustrated in Figure 5.9a, the net radiative effect of *plt* and *sph* changes its sign from warming for optically thin cirrus to cooling for optically thicker cirrus at τ around 3–4. For P2 (cf. Figure 5.9b), this effect was observed at smaller optical thickness ($\tau = 1.5$) for *plt*. Assuming *sph*, the IR warming effect outweighs the cooling solar albedo effect during P2 for all observed τ . The net radiative forcing of tropical cirrus anvils at TOA was investigated by Jensen et al. (1994). They report a warming effect of cirrus for $\tau \leq 16$ and a cooling effect for cirrus with larger optical depths. However, in that study cirrus near the tropical tropopause was considered. These clouds are situated at higher altitudes than in the case studies presented here and are thereby situated in colder environments thus leading to stronger thermal IR warming. $\Delta F_{\text{TOA}}^{\text{net}}$ values reported in other studies are on the order of our results. For example, Mace et al. (2006a) report yearly $\Delta F_{\text{TOA}}^{\text{net}}$ averages at the ARM SGP site of $-30 - +16 \text{ W m}^{-2}$.

As in the study of Wendisch et al. (2007), the net radiative cooling effect of the observed cirrus is much stronger at BOA than at TOA. $\Delta F_{\text{TOA}}^{\text{net}}$ ranged between $-77 - +15 \text{ W m}^{-2}$ at P1 and $-38 - +29 \text{ W m}^{-2}$ at P2. As at BOA, strongest cooling was observed for *scl* and *agg*. The shape effect at TOA is stronger than at BOA and amounts to up to 100 % (*plt*) and 120 % (*sph*) during P1, and 115 % (*plt*) and 180 % (*sph*) during P2 (always with respect to *scl*).

What should be kept in mind is that instantaneous radiative forcings are considered here. In

reality, the effects of the cirrus on solar radiation only is important for daytime while thermal IR radiation is absorbed and emitted around the clock. Thus, results for ΔF^{net} presented here refer to daytime conditions, at night positive ΔF^{net} occur due to the sole contribution of thermal IR radiation.

Summing up the results it can be stated that for the considered case studies the assumption of ice crystal shape on the cirrus radiative forcing does play an important role. Strongest net cooling was observed under the assumption of *scl* and *agg* while the smallest radiative impact was obtained when assuming *plt* and *sph*.

6 Cirrus Spatial Heterogeneity Versus Crystal Shape Effects

The first part of this work focuses on the effect of assumed ice crystal shape on the retrieval of cirrus optical thickness τ and particle effective radius R_{eff} (cf. Chapter 4 and 5). Two case studies based on measurements of spectral upwelling radiance I_{λ}^{\uparrow} with the SMART-Albedometer made during the CIRCLE-2 aircraft field experiment (cf. Chapter 3) were presented. The ice crystal shape assumption was found to have a significant impact on the retrieved cirrus properties. However, as indicated in Section 1.1, remote sensing retrievals are also biased by spatial heterogeneities of microphysical cloud properties. In the presented CIRCLE-2 case studies cirrus spatial heterogeneity effects were not addressed because no information on the 3D cloud structure was obtained.

Subsequently, the relative importance of 3D effects and ice crystal shape of spatially inhomogeneous cirrus on the remote sensing of τ and R_{eff} is evaluated. This part of the study is based on 3D and independent pixel approximation (IPA) radiative transfer calculations performed with MYSTIC (Monte Carlo code for the physically correct tracing of photons in cloudy atmospheres, Mayer (2009)). As model input a cirrus cloud case that was generated from data collected during the NASA Tropical Composition, Cloud, and Climate Coupling (TC⁴) experiment is used.

The analyzed cirrus is introduced in Section 6.1. Section 6.2 gives an overview of the radiative transfer simulations as well as associated uncertainties in the retrieval results. In Section 6.2.2 the cirrus retrieval results are presented. While in Section 6.3.1 the effects of cirrus heterogeneity are assessed, Section 6.3.2 focuses on the ice crystal habit effects. Finally, both effects on the retrieval of τ and R_{eff} are compared in Section 6.3.3.

6.1 The TC⁴ Experiment

6.1.1 Overview

The data used for the generation of the 3D cirrus cloud was collected during the NASA TC⁴ experiment based in Costa Rica and Panama in July and August, 2007. This field experiment aimed at investigating the atmospheric structure, properties, and processes in the tropical Eastern Pacific. It focused on characterizing the Tropical Tropopause Layer (TTL), cirrus anvil production and evolution processes, and the role of sub-visible cirrus in the exchange between stratosphere and troposphere (Toon et al., 2009). The linking of satellite and aircraft data was another key issue. Among several aircraft, the NASA ER-2 was

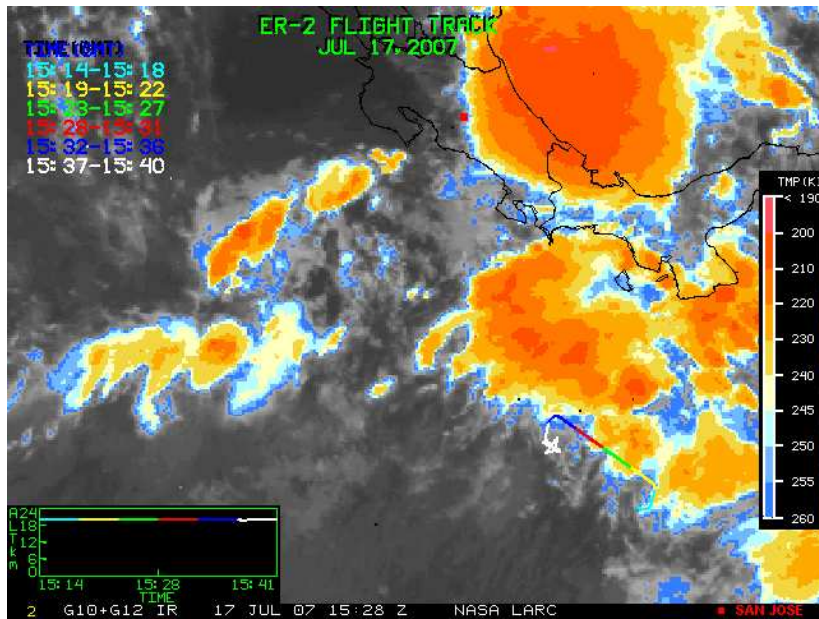


Figure 6.1: IR image of the GOES G10 and G12 satellites from 15:28 UTC on July 17, 2007. The ER-2 flight track at 15:20–15:35 UTC is superimposed on the satellite image. A plot of flight altitude versus time is inserted in the lower left corner. San Jose in Costa Rica is indicated by a small red square in the upper centre of the image. The color scale for the brightness temperatures is displayed at the right side: red refers to lowest temperatures, blue to highest. Image courtesy NASA (<http://www-angler.larc.nasa.gov/tc4/>).

employed. This aircraft was equipped with remote sensing instruments, such as the MODIS Airborne Simulator (MAS, King et al. (1996)), the Cloud Radar System (CRS, Li et al. (2004)), and the Solar Spectral Flux Radiometer (SSFR, Pilewskie et al. (2003)). Including the transit flights, the ER-2 flew 13 science missions during TC⁴.

The cloud field observed at the flight on July 17, 2007 was selected to construct the model cloud used as input for radiative transfer simulations. During that mission the flight path was situated over the Eastern Pacific approximately 550 km west of Columbia and 300 km south of Panama (around 5°N, 83°W). High level outflow cirrus downstream of a line of convective systems situated northeast of the flight track was probed. The ER-2 was flying well above cloud top level at 20 km towards the northwest and the solar incidence was from the northeast with a solar zenith angle of approximately 35°. The cloud scene is shown in Figure 6.1, displaying the IR image of the Geostationary Operational Environmental Satellites (GOES) G10 and G12.

6.1.2 Input Cloud Generation

Data from MAS and CRS were used to construct a 3D cloud based on the ER-2 flight leg from 15:20 to 15:35 UTC on July 17, 2007 (approximately 190 km long). The same cloud field was examined by Schmidt et al. (2009) in the context of cloud absorption.

MAS measures fields of I_{λ}^{\uparrow} at $\lambda = 0.87 \mu\text{m}$ and $\lambda = 2.13 \mu\text{m}$ along the flight path of the ER-2. It retrieves horizontal fields of τ and R_{eff} from these I_{λ}^{\uparrow} measurements following the

bispectral reflectance method (cf. Section 4.2) which is discussed in detail for MAS cloud products by King et al. (2004). In addition to τ and R_{eff} , MAS provides fields of cloud top height z_{top} ; all at a resolution of 50 m or 100 m (depending on z_{top} and flight altitude). For cirrus, the MAS z_{top} retrieval is based on the CO₂ slicing technique (Menzel et al., 1983) as used by MODIS (Menzel et al., 2008). For low level clouds, z_{top} is determined using the IR window method (or IR brightness temperature method, Schmetz et al. (1993)).

The radar reflectivity profiles $Z(z)$ measured by the CRS were used to determine the vertical cloud structure below the ER-2 flight track. The resolution of the reflectivity field is 100 m in the horizontal and 37.5 m in the vertical.

The 2D field of τ retrieved from MAS gridded to 500 m resolution is shown in the upper panel of Figure 6.2. It covers an area of 192 km \times 17.5 km (distance along flight track multiplied by MAS swath). The MAS swath was determined from the ER-2 altitude of 20 km and an average cloud top altitude of 11.25 km as determined by CRS. The dashed line along $y = 0$ km represents the ER-2 flight track. Within the cloud scene, τ ranges between 5 and 100, with regions of high cloud extinction heterogeneity indicated by a high variability in τ . Cloud-free areas in the scene are displayed in white. The MAS-derived cloud top height along the nadir track varied between 8 and 12 km. It is represented by a black line in the vertical cross section of radar reflectivity from CRS in the lower panel of Figure 6.2. In addition to the outflow cirrus, some patches of low-level cloud between 0–3 km were present. The column-retrieved optical thickness comprises contributions from both low-level liquid and high-level ice clouds. For simplicity, both the low level and the high level clouds were treated as ice clouds in this modeling study.

Using the relationship determined by Liu and Illingworth (2000), the profile of radar reflectivity Z , was used to derive approximate vertical profiles of ice water content ($IWC(z)$, in g m^{-3}) along the flight track:

$$IWC(z) = 0.137 \cdot Z(z)^{0.64}. \quad (6.1)$$

For each vertical profile along flight track, the column-integrated ice water path (IWP_{CRS}) was calculated. The IWP was also retrieved from MAS following (Stephens, 1978):

$$IWP_{\text{MAS}} = \frac{2}{3} \cdot \rho_{\text{ice}} \cdot \tau \cdot R_{\text{eff}}, \quad (6.2)$$

with ρ_{ice} being the density of ice (approximately 0.925 g cm^{-3}). While the CRS profile was only measured along the center (nadir) track, MAS-derived IWP was available across the entire swath for each point along the track. In the model cloud, the vertical IWC profiles were obtained through:

$$IWC(z) = \frac{IWC_{\text{CRS}} \cdot IWP_{\text{MAS}}}{IWP_{\text{CRS}}}, \quad (6.3)$$

with the assumption that the vertical distribution of ice water was constant across the MAS swath. The entire profile was shifted up or down corresponding to z_{top} as retrieved by MAS.

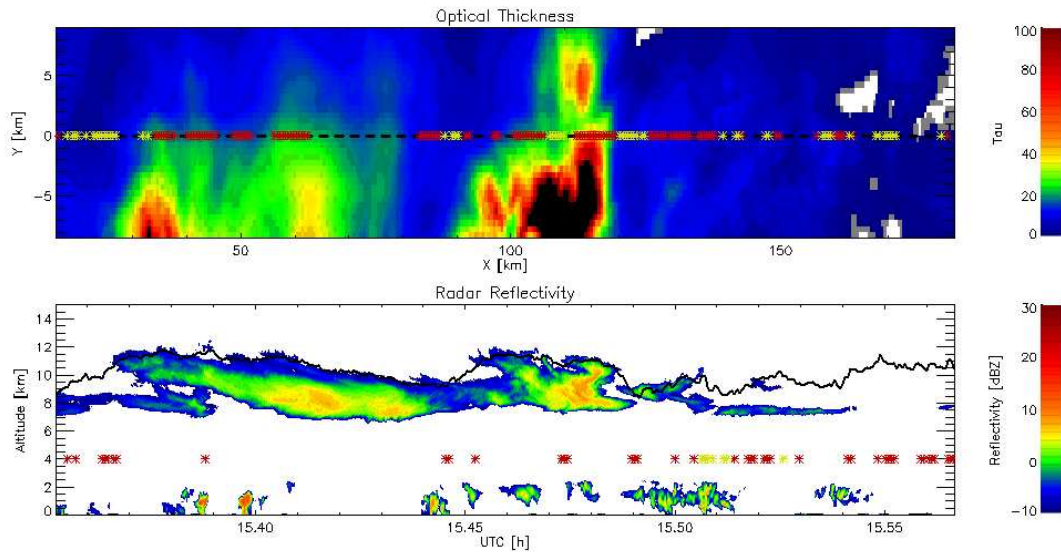


Figure 6.2: TC⁴ cloud data from the ER-2 for a portion of the 17 July 2007 flight track (15:21–15:34 UTC = 15.35–15.57 decimal time) used in generating the 3D cloud. Upper panel: MAS-retrieved cloud optical thickness τ (swath 17.5 km) gridded to 500 m resolution. Clear-sky gaps are represented in white. Crosses at $y = 0$ km (ER-2 flight track) indicate regions at which τ retrieved with 3D calculations was under-/ overestimated (dark red/yellow). Lower panel: Radar reflectivity from CRS in dBZ with cloud top altitude from MAS along the ER-2 flight track (thick black line). Crosses indicate regions at which R_{eff} retrieved with 3D calculations was under-/ overestimated (dark red/yellow). The marks are explained in Secion 6.3.1.

In lack of other information, the effective radius was set to

$$R_{\text{eff}}(x, y, z) = R_{\text{eff,MAS}}(x, y), \quad (6.4)$$

i.e., assumed constant throughout the entire cloud column. This is clearly a simplification because deeper down into the clouds, ice particle size distributions are different from that near cloud top. Moreover, the R_{eff} in the underlying liquid water clouds is presumably much smaller. The MAS-derived R_{eff} is representative of the upper cloud layers (Platnick, 2000) where ice crystals are often smaller than in lower layers within the cirrus (e.g., Francis et al., 1998; Gayet et al., 2004).

Summarizing, all the cloud properties: IWC , τ , R_{eff} , and z_{top} were tied to MAS measurements; the CRS profiles were used to distribute the MAS-derived IWP in the vertical dimension, whereby another simplification consists in using the nadir-only CRS profiles for distributing IWP_{MAS} values vertically across the entire swath. Assumed ice crystal shapes were also set constant with height. The generated 3D cloud (IWC , R_{eff}) was gridded to 500 m horizontal and 1000 m vertical resolution. More information on the input cloud generation can be found in Schmidt et al. (2009).

6.2 Methodology

6.2.1 Strategy

In order to compare the relative impact of cirrus 3D effects and ice particle habits on the retrieval of τ and R_{eff} , the following strategy which is illustrated in Figure 6.3 was pursued. As in Chapter 5, single-scattering properties of ice crystals from the databases of Key et al. (2002) and Baum et al. (2005b) were employed. For this part of the work, hexagonal plates (*plt*), solid columns (*scl*), and rough aggregates (*agg*) as well as the mixture of particle habits (*mix*) are considered.

The strategy is as follows:

- (a) Cloud generation: Build a 3D cloud field from MAS data (2D fields of τ and R_{eff}) and CRS data ($IWC(z)$) (cf. Section 6.1.2). Optical thickness and effective radius of this cloud are referred to as τ^{inp} and $R_{\text{eff}}^{\text{inp}}$.
- (b) Consistency check: From this generated cloud, calculate upwelling radiances $I_{\lambda}^{\uparrow, \text{IPA}}$ (and hence cloud top reflectances $r_{c, \lambda}^{\text{IPA}}$) along nadir track (for wavelengths $\lambda = 0.87 \mu\text{m}$ and $\lambda = 2.13 \mu\text{m}$, assuming *mix*) with the radiative transfer model MYSTIC in IPA mode (cf. Section 6.2.2). Use these $I_{\lambda}^{\uparrow, \text{IPA}}$ to retrieve back τ and R_{eff} and compare these values to the input cloud values τ^{inp} and $R_{\text{eff}}^{\text{inp}}$ (cf. Section 6.2.3). The retrieved results should be consistent with the input cloud values since both, the MYSTIC-IPA calculations and the LUT, are based on *mix*.
- (c) Impact of cloud heterogeneities (Γ ratios): Use MYSTIC in full 3D mode (see Section 6.2.2) with *mix* to calculate upwelling radiances $I_{\lambda}^{\uparrow, 3\text{D}}$ (and hence cloud top reflectances $r_{c, \lambda}^{3\text{D}}$) along nadir track at 500 m resolution as they would be measured by imaging radiometers. From these $I_{\lambda}^{\uparrow, 3\text{D}}$ derive $\tau^{3\text{D}}$ and $R_{\text{eff}}^{3\text{D}}$ by using the *mix*-LUT to simulate a standard (e.g., MAS or MODIS) retrieval of τ and R_{eff} . Define ratios $\Gamma_{\tau} = \tau^{3\text{D}}/\tau^{\text{inp}}$ and $\Gamma_{R_{\text{eff}}} = R_{\text{eff}}^{3\text{D}}/R_{\text{eff}}^{\text{inp}}$ as measures of 3D cloud structure effects.
- (d) Impact of ice crystal shape (Ψ ratios): First, determine the crystal shape effect on cloud top reflectances r_c . Therefore, calculate $I_{\lambda}^{\uparrow, \text{IPA}}$ (and hence $r_{c, \lambda}^{\text{IPA}}$) for wavelengths $\lambda = 0.87 \mu\text{m}$ and $\lambda = 2.13 \mu\text{m}$ using different ICP (*mix*, *plt*, *scl*, *agg*) with MYSTIC-IPA (cf. Section 6.3.2). Secondly, from the radiances calculated with *mix*, retrieve τ^{IPA} and $R_{\text{eff}}^{\text{IPA}}$ with *plt*, *scl*, *agg* LUTs (cf. Section 6.3.2). Define ratios $\Psi_{\tau} = \tau^{\text{IPA}}/\tau^{\text{inp}}$ and $\Psi_{R_{\text{eff}}} = R_{\text{eff}}^{\text{IPA}}/R_{\text{eff}}^{\text{inp}}$ as a measure of the ice crystal habit effect. IPA is used in order to better separate effects caused by crystal habit assumptions from cloud spatial heterogeneity effects.
- (e) Comparison: Assess the relative importance of 3D cloud structure (Γ) and crystal shape (Ψ) on the retrieved values, and examine the impact of cloud optical thickness, effective radius, and cloud variability on the two effects (cf. Section 6.3.3).

Several details about the methodology should be mentioned: First, the cloud field that serves as input to the MYSTIC-3D and MYSTIC-IPA radiative transfer calculations is already affected by 3D effects because it is based on data from an imaging radiometer (MAS).

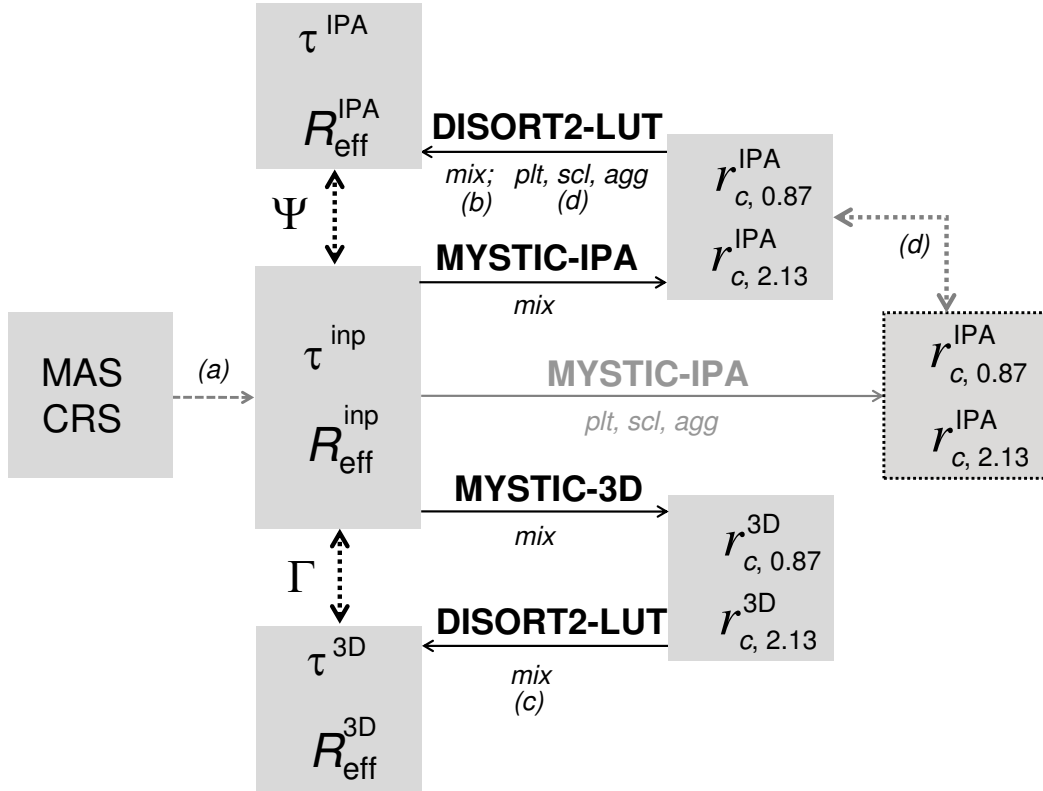


Figure 6.3: Schematic of the methodology. In the first step (a), a 3D cloud field (τ^{inp} and $R_{\text{eff}}^{\text{inp}}$) is generated from MAS and CRS data. Next, radiative transfer calculations are made with the MYSTIC code assuming *mix*: both the 3D (MYSTIC-3D), and independent pixel approximation modes (MYSTIC-IPA) are run. The resulting fields of upwelling radiance I_{λ}^{\uparrow} (and hence cloud top reflectance r_c) at two wavelengths ($0.87 \mu\text{m}$ and $2.13 \mu\text{m}$) are used to retrieve back τ and R_{eff} using pre-calculated LUT of reflectance pairs generated with DISORT2 (cf. step (b) and (c)). The retrieved values for τ^{3D} and $R_{\text{eff}}^{\text{3D}}$ based on $r_{c, \lambda}^{\text{3D}}$ (using the *mix*-LUT) are compared with the original input cloud values, and their pixel-by-pixel ratio Γ serves as a measure for 3D-effects. From the MYSTIC-IPA based reflectance fields, values for τ and R_{eff} are retrieved back using LUTs calculated assuming *plt*, *scl*, and *agg*, see text for details at step (d). The pixel-by-pixel ratio Ψ of the retrieved values to the input cloud values serves as a measure for ice crystal habit effects. Additionally, cloud top reflectances determined with MYSTIC-IPA ($r_{c, \lambda}^{\text{IPA}}$) assuming *mix* are compared to $r_{c, \lambda}^{\text{IPA}}$ assuming *plt*, *scl*, *agg* to single out the crystal shape effect on r_c (see step (d)).

However, the results of this study are not dependent on how closely the original cloud field was matched; the generated cloud is taken as a realistic sample cloud. The choice of ICP (*mix*, *plt*, *scl*, *agg*) does not represent all of the overall natural variability of crystal shapes and corresponding single-scattering properties. Also, as described in Section 4.1.4, it should be kept in mind that the Baum et al. (2005b) parameterization uses an explicit scattering phase function $\mathcal{P}(\cos \vartheta)$ (i.e., as function of the scattering angle), while the parameterizations of Key et al. (2002) use a double Henyey-Greenstein parameterization for $\mathcal{P}(\cos \vartheta)$. Hence, when analyzing Ψ ratios, it should be kept in mind that the deviation from unity does not solely result from the different ice crystal habits, but potentially could also stem from the different handling of $\mathcal{P}(\cos \vartheta)$. However, the main differences between the different ICP are caused by differences in single scattering albedo ($\tilde{\omega}$) and asymmetry parameter (g), both of which are well described by both *mix* and the parameterizations of Key et al. (2002). Secondary differences induced by particular features of $\mathcal{P}(\cos \vartheta)$ (which can not be reproduced by the double Henyey-Greenstein parameterization) are unlikely to change the results qualitatively, although minor quantitative changes can be expected.

6.2.2 Radiative Transfer Modelling and Cirrus Retrieval

The generated 3D ice cloud field (cf. Section 6.1.2) was used as input for radiative transfer simulations. In this part of the work, radiative transfer calculations of I_{λ}^{\uparrow} at 20 km altitude (the flight altitude of the ER-2) were performed with MYSTIC (Emde and Mayer, 2007; Mayer, 2009) which is embedded in *libRadtran*.

With Monte Carlo solvers such as MYSTIC the radiation field is modelled by tracing individual photons on their random path through the 3D atmosphere. The model domain is divided into grid cells (pixels), within each grid cell the optical properties are constant. The single-scattering albedo (cf. Eq. 2.14) of a particular grid cell determines the probability that a photon reaching this cell is either absorbed or scattered into a random direction. The probability for scattering into a certain direction is given by the scattering phase function \mathcal{P} . A photon is traced until it is absorbed or leaves the model domain at TOA, absorption or scattering at the surface are taken into account.

Monte Carlo radiative transfer is computationally expensive. The accuracy of the results is determined by the number of photons. In MYSTIC some methods which speed up the calculation by improving the photon statistics are employed. Thus, the simulations were performed in the backward Monte Carlo mode (i.e., tracing photons from the detector to the source; cf. Mayer (2009)) and using the bias-free "Variance Reduction Optimal Options Method" (VROOM, Buras, 2009, in preparation). This method is also known as local or directional estimate technique. At each scattering point it calculates the probability that the photon is scattered into the direction of the *sensor*, rather than into the actual scattering direction. However, the actual photon path is not affected by this technique. Also, the extinction between the location of the scattering event and the detector is taken into account.

MYSTIC can be run in full 3D (MYSTIC-3D) and in IPA mode (MYSTIC-IPA). In the latter case, the 3D model domain is approximated by independent columns for each of which 1D

Table 6.1: Cirrus retrieval input of the TC⁴ case study. φ denotes the aircraft heading.

Input parameter	TC ⁴ case study
Surface albedo	water (Cox and Munk, 1954)
θ_0	35°
φ_0	113°
φ	307°
Aerosol profile	maritime summer
Cloud base height	8.0 km
Cloud top height	11.0 km
τ	0.1–60.1
$\Delta\tau$	5.0
R_{eff}	15–50 μm
ΔR_{eff}	5 μm

RTE-calculations are applied. Thus, net horizontal photon transport between the columns (or pixels) is neglected.

Monte Carlo calculations were performed 10 times with the same input. In each of these calculations 10.000 photons were traced for each wavelength and each pixel along the nadir track, resulting in a standard deviation (σ) in I_λ^\uparrow of 1.0–1.7%. As described in Mayer (2009), the uncertainty of the Monte Carlo results decreases with the square root of the number of photons.

The basic radiative transfer model input used here follows the description given in Section 4.1.1. Here, the tropical standard atmosphere profile from Anderson et al. (1986) was used. As shown in Figure 6.1, the probed cirrus was situated over the Eastern Pacific. Thus, a surface albedo of water was employed. It was parameterized following Cox and Munk (1954) assuming a surface wind speed of 5 m s^{-1} . According to the wavelengths used in the MAS-retrieval of τ and R_{eff} , calculations were made at 0.87 μm (no cloud absorption) and 2.13 μm (ice crystals are absorbing).

The retrieval of τ and R_{eff} from the MYSTIC-3D and MYSTIC-IPA calculated I_λ^\uparrow (and hence r_c ; leftward arrows in Figure 6.3) relies on bispectral LUT described in Section 4.2. The LUTs were pre-calculated for pairs of r_c (at 0.87 μm and 2.13 μm) using the DISORT2 algorithm (Stamnes et al., 1988b) which has been shown to agree with MYSTIC within better than 0.1% for one-dimensional cases (Mayer, 2009). For the solar geometry that prevailed during the flight leg, LUT calculations were performed for τ ranging from 0.1–50.1 in steps of $\Delta\tau = 5$ and R_{eff} ranging from 15–60 μm in steps of $\Delta R_{\text{eff}} = 5 \mu\text{m}$ as illustrated in Figure 6.4. LUTs were generated assuming *mix*, *plt*, *scl*, and *agg*. The *libRadtran* model input for the cirrus retrieval is summed up in Table 6.1. For retrieving τ and R_{eff} from $I_\lambda^{\uparrow,3\text{D}}$ and $I_\lambda^{\uparrow,\text{IPA}}$ (assuming *Baum-mix*), the latter were first converted to reflectance pairs $r_c^{3\text{D}}(0.87, 2.13)$ and $r_c^{\text{IPA}}(0.87, 2.13)$. These reflectance values at 0.87 μm and 2.13 μm were matched to the best-fitting pair of pre-calculated LUT reflectance pairs. The LUTs were interpolated linearly in order to obtain a finer resolution in τ and R_{eff} space. The values of τ and R_{eff} as retrieved back from MYSTIC-3D calculated reflectance pairs $r_c^{3\text{D}}(0.87, 2.13)$ are named $\tau^{3\text{D}}$ and $R_{\text{eff}}^{3\text{D}}$. They correspond to what remote sensing instruments would retrieve for the input cloud. Likewise, retrieved τ and R_{eff} values based on $I_\lambda^{\uparrow,\text{IPA}}$ (and thus r_c^{IPA}) from the

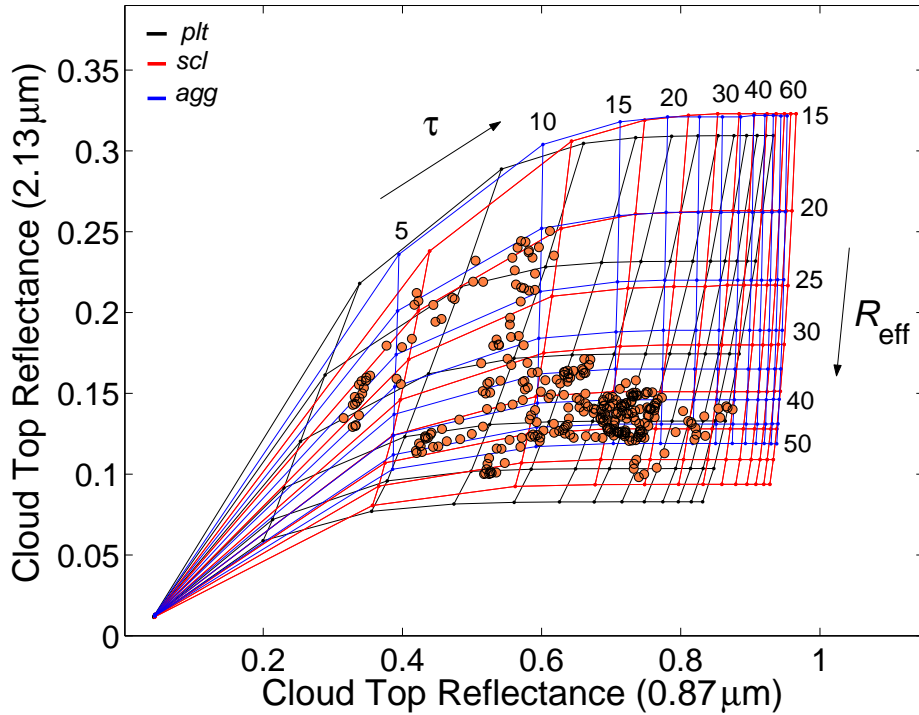


Figure 6.4: Cloud retrieval solution space for three particle habits (*plt*, *scl*, *agg*) showing contours of constant τ and R_{eff} (in μm). Modelled cloud top reflectances r_c along the nadir track of the TC⁴ case based on MYSTIC-IPA calculations assuming a mixture of particle habits (*mix*) are represented by dots.

MYSTIC-IPA (*mix*) calculations are referred to as τ^{IPA} , and $R_{\text{eff}}^{\text{IPA}}$ (cf. Figure 6.3). These retrievals used LUTs based on *plt*, *scl*, and *agg*. This method basically corresponds to a mapping of one LUT (*mix*) onto another (*plt*, *scl*, and *agg*) to determine the crystal shape effect as also done for the CIRCLE-2 case studies in Chapter 5.

It should be kept in mind that the observed and modelled r_c in the CIRCLE-2 case studies (cf. Chapters 4 and 5) were averaged over the wavelength bands 0.6–0.7 μm and 1.5–1.65 μm since the optical properties in the ice cloud parameterization by Key et al. (2002) are constant over these wavelength ranges. In this part of the study however, spectral radiative transfer calculations (at 0.87 μm and 2.13 μm) were made because simulations with MYSTIC are computationally expensive. To quantify the effect of either using spectral simulations of r_c or band-averaged r_c values, the cirrus retrieval for the CIRCLE-2 case studies was repeated doing spectral calculations of r_c at 0.67 μm and 1.6 μm and comparing the resulting values of τ and R_{eff} with the ones based on the band-averaged r_c . With mean differences (averaged over all crystal shapes and over the time series) in τ of 3% during P1 and 5% during P2 the discrepancies are within the uncertainty of the τ retrieval results. Due to the rather big "step" in r_c based on Key et al. (2002) (cf. Figure 4.8) between $\lambda \leq 1.65 \mu\text{m}$ and $\lambda \geq 1.65 \mu\text{m}$, differences in retrieved R_{eff} are bigger, on average they amount to 11% (P1) and 10% (P2) and thus are slightly bigger than the R_{eff} uncertainty (cf. Table 5.1). The uncertainty introduced by doing spectral calculations of r_c is paid attention to in the uncertainty estimation in Section 6.2.4 in Table 6.2.

6.2.3 Consistency Check

Calculations of I_λ^\uparrow were made with MYSTIC in 3D mode and in IPA mode. This was done in order to use the exact same model for IPA and 3D calculations. To check that MYSTIC-IPA gives indeed the same results as the DISORT algorithm, IPA calculations with DISORT2 were made for each pixel. I_λ^\uparrow determined with MYSTIC-IPA and DISORT2 agreed to within 0.5% and 1.7% (mean relative deviations at $0.87\ \mu\text{m}$ and $2.13\ \mu\text{m}$, respectively) assuring the number of photons used in the Monte Carlo simulations was adequate. Moreover, this agreement justifies using DISORT2 (instead of MYSTIC-IPA) in the determination of the LUT and the retrieval of τ^{IPA} , $R_{\text{eff}}^{\text{IPA}}$, τ^{3D} , and $R_{\text{eff}}^{\text{3D}}$. When doing MYSTIC-IPA calculations of I_λ^\uparrow based on *mix* and retrieving τ^{IPA} and $R_{\text{eff}}^{\text{IPA}}$ with a LUT also based on *mix*, results should exactly reproduce the input cloud values. This was tested and confirmed: The retrieved τ^{IPA} and $R_{\text{eff}}^{\text{IPA}}$ were almost equal to the original τ^{inp} and $R_{\text{eff}}^{\text{inp}}$ values, with only minor deviations (1% in τ and 0.1% in R_{eff} on average, see Figure 6.5).

6.2.4 Uncertainties

When addressing the uncertainty of the retrieval results, several influences are considered. One part is the standard deviation (σ) of MYSTIC-IPA and MYSTIC 3D calculations and how they propagate into the retrieval results of τ and R_{eff} . This error component was examined by adding and subtracting the Monte Carlo standard deviations from the calculated r_c . From these upper and lower limits of the modelled r_c , the corresponding 1σ uncertainty range of τ and R_{eff} for each pixel was derived. Furthermore, uncertainties can arise from z_{top} differences in the input cloud and the fixed z_{top} of 11 km (cf. Table 6.1) used for the LUT calculations. However, the influence of variations in z_{top} in the LUT calculations was found to be neglectable ($< 0.1\%$). Moreover, the influence of the LUT resolution was quantified by decreasing the spacing of $\Delta\tau$ and ΔR_{eff} to 1. Its influence on retrieved properties ranged between 0.4–1.1% (cf. Table 6.2). Besides, uncertainties in matching the r_c of the model cloud to the best-fitting LUT reflectance pairs were determined. Therefore, the retrieval was made using MYSTIC-IPA I_λ^\uparrow of a certain crystal habit and employing the corresponding LUT of the same habit. Retrieved τ and R_{eff} of all habits are then expected to be alike and should reproduce the input cloud values (τ^{IPA} and $R_{\text{eff}}^{\text{IPA}}$) so the observed differences in the retrieval results are attributed to interpolation uncertainties. This procedure proves as validation of the method and is described in detail in Section 6.2.3 for *mix*. In addition, the uncertainty introduced by doing spectral calculations though optical properties in the database of Key et al. (2002) are band-averaged values as described in Section 6.2.2 was addressed. The combined uncertainties of the potential error sources were determined. The standard deviations of the MYSTIC calculations influence the other mentioned uncertainties. However, Gaussian error propagation gives an upper limit for the retrieval uncertainty and amount to about 5%, 10%, 6%, and 10% for τ^{IPA} , $R_{\text{eff}}^{\text{IPA}}$, τ^{3D} , and $R_{\text{eff}}^{\text{3D}}$, respectively as listed in Table 6.2.

Table 6.2: Uncertainties of the TC⁴ cirrus retrieval results. The total error was determined with Gaussian error propagation.

In- fluence on	r_c variation with MYSTIC-std	z_{top} vari- ation	LUT reso- lution	Inter- polation uncertainty	Spec- tral calculation	Total retrieval uncertainty
τ^{IPA}	1.6 %	<0.1 %	0.7 %	2.1 %	4.0 %	4.8 %
$R_{\text{eff}}^{\text{IPA}}$	0.9 %	<0.1 %	0.4 %	0.5 %	10.0 %	10.1 %
τ^{3D}	1.4 %	<0.1 %	1.1 %	4.5 %	4.0 %	6.3 %
$R_{\text{eff}}^{\text{3D}}$	0.9 %	<0.1 %	0.8 %	2.2 %	10.0 %	10.3 %

6.3 Cloud Retrieval Results

The retrieval results along the flight path in nadir direction (assuming *mix*) are illustrated in the upper panels of Figure 6.5. Percentage deviations of the retrieved values from the input cloud values are shown in the lower panels. As obvious in the plot, the cloud field exhibited strong spatial heterogeneities, with τ varying by a factor of 9 ($\tau = 5\text{--}45$). Variations of R_{eff} were much smaller (up to a factor of two) with R_{eff} ranging from $16\ \mu\text{m}$ to $36\ \mu\text{m}$. Small R_{eff} were often observed during optically thinner parts of the cirrus while largest R_{eff} generally occurred in optically thicker cloud regions.

6.3.1 3D Effects

Retrieved values (τ^{3D} and $R_{\text{eff}}^{\text{3D}}$) are influenced by horizontal as well as vertical cirrus inhomogeneities which can result in both over- and underestimation of τ and R_{eff} . Such effects are not captured by IPA calculations. In Figure 6.5a, the most pronounced feature in the time series of τ occurs at 110–120 km along the flight track where highest values of τ (30–45) were observed. The peak of 3D retrieved optical thickness (τ^{3D} , in green) is shifted with respect to the peak in the input cloud. The reason becomes obvious when looking at the off-nadir distribution of τ^{inp} in the original cloud field (Figure 6.2). While on the flight track, the maximum τ^{inp} occurs at 118 km, τ^{3D} along the flight track picks up contributions from cross-track pixels. Obviously, the high optical thickness areas at $x \approx 105\text{--}115\ \text{km}$, $y \approx -5\ \text{km}$ lead to a peak in τ^{3D} at $x \approx 109\ \text{km}$. This is caused by *horizontal* photon transport from areas of high to low photon density (i.e., from bright to dark regions). In this case, this is equivalent to transport from high to low optical thickness areas. Regions with a relatively thin cirrus layer in propagation with patches of relatively thick low-level clouds (cf. Figure 6.2) are prone to strong *vertical* 3D effects: Photons reaching the low cloud are lost through the sides and eventually get absorbed by the dark ocean surface. This photon leakage results in an *underestimation* of τ as observed at distances of 42, 50, 85, 125–135 km along the flight track (cf. Figure 6.2 (upper panel), and Figure 6.6a: underestimation of τ marked by dark red symbols).

Doing MYSTIC-3D calculations mostly leads to an *overestimation* of effective radius along this specific flight track. Strong overestimation of the R_{eff} occurs mostly in optically thin regions (e.g., at 133–140 km along the flight track) or partly cloud-free areas (see Figure 6.2b

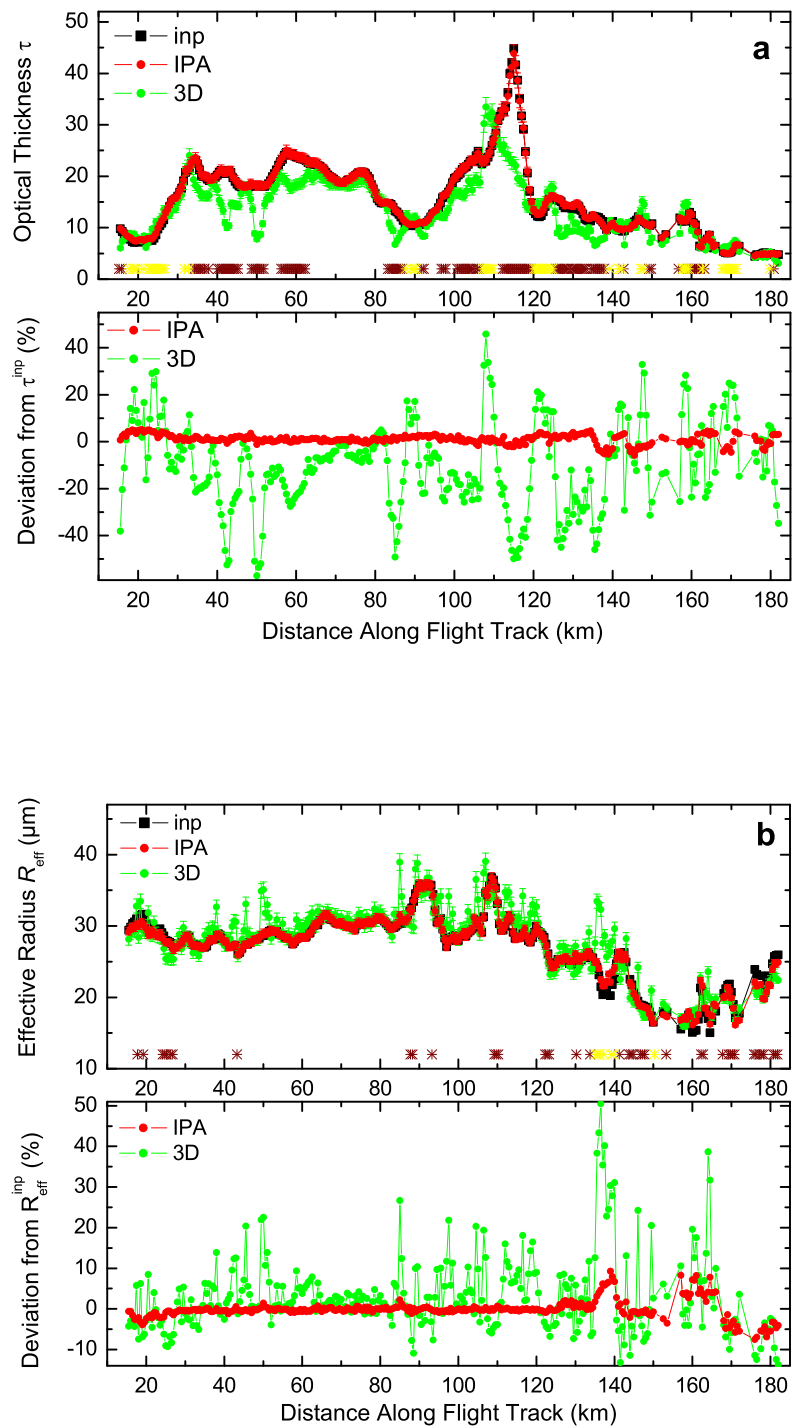


Figure 6.5: Comparison of the input cloud a) τ^{inp} and b) $R_{\text{eff}}^{\text{inp}}$ with retrieval results along nadir track of the ER-2. MYSTIC-IPA (red) and MYSTIC-3D (green) results using the single-scattering properties of *mix* are shown. In the upper panels in a) and b), regions where 3D results under-/overestimated input cloud values are marked with dark red/yellow crosses. In the bottom panels, relative deviations of the IPA- and 3D- based retrieval results from the input cloud values are plotted.

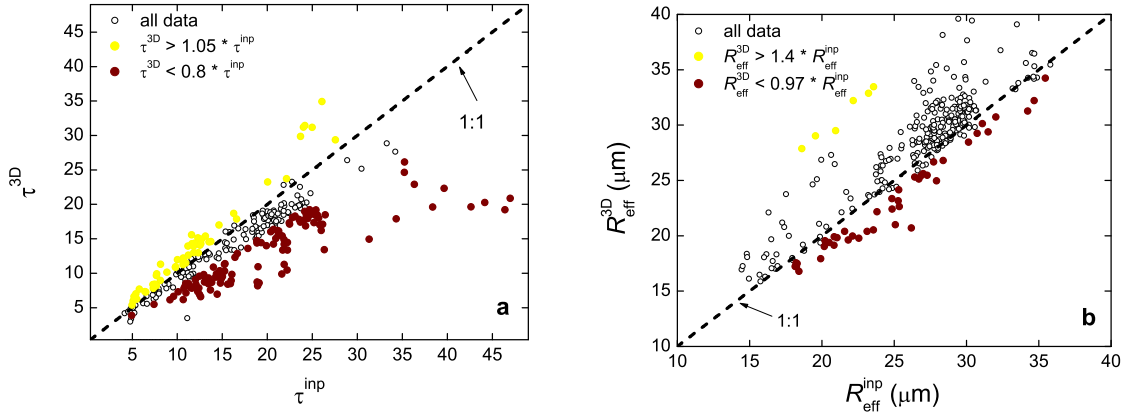


Figure 6.6: a) Retrieved τ^{3D} versus τ^{inp} and b) R_{eff}^{3D} versus R_{eff}^{inp} assuming *mix*. Under- and (strong) overestimation of input cloud values are marked with dark red and yellow symbols, respectively.

(upper panel), strong overestimation marked by yellow symbols). In these areas radiation penetrates to the strongly absorbing sea-surface. However, upward scattering of photons at the low-level cloud can also cause increased reflectances at $2.13 \mu m$ resulting in an *underestimation* of R_{eff} (e.g., at 89, 93, 123–125, 129–131 km along flight track). The strongest underestimations of R_{eff} are found in areas of thin (or broken) cirrus layers, with boundary layer clouds underneath. In the context of over- and underestimation of τ and R_{eff} by 3D calculations, the dependence of horizontal smoothing scale on wavelength as discussed in Platnick (2001) is important. There it was shown that the horizontal displacement of photons is considerably shorter at absorbing wavelengths. This leads to sharp peaks at which R_{eff}^{3D} deviate from R_{eff}^{inp} . These peaks extend over only a few pixels because the horizontal transport of photons at $2.13 \mu m$ is over short distances only (cf. Figure 6.5b). In contrast, τ^{3D} exhibit rather broad and smooth deviations from τ^{inp} (cf. Figure 6.5a). This is attributed to the long horizontal smoothing scales at $0.87 \mu m$, the wavelength used for the determination of τ^{3D} . The different horizontal path lengths at $0.87 \mu m$ and $2.13 \mu m$ cause different reflectance enhancement factors in the 3D calculations so that under- or overestimations of τ^{inp} and R_{eff}^{inp} have different magnitudes and spatial extents.

In Figure 6.6 τ^{3D} and R_{eff}^{3D} (assuming *mix*) are plotted versus τ^{inp} and R_{eff}^{inp} . Strong under- and overestimation of the original values are marked with dark red and yellow symbols, respectively. The thresholds in Figure 6.6 are chosen for illustration of those regions at which under- and overestimations occur in Figure 6.2 and Figure 6.5 (highlighted by marks with the same color code). Figure 6.6a shows that for the observed cloud scene, remote sensing instruments with 500 m spatial resolution (which measure $I_{\lambda}^{\uparrow,3D}$ influenced by cloud 3D effects) would mostly underestimate the true τ by more than 20%. At the same time (cf. Figure 6.5b and Figure 6.6b), they would often overestimate R_{eff} by about 3–15%. Averaged over the flight leg from 15.5–182.0 km, the original optical thickness, τ^{inp} is 16, and the retrieved value, τ^{3D} is 14 (12% underestimation). Similarly, averaged $R_{eff}^{inp} = 27 \mu m$, and averaged $R_{eff}^{3D} = 28 \mu m$ (4% overestimation). The underestimation of τ and overestimation

Table 6.3: Asymmetry parameter g and single-scattering albedo $\tilde{\omega}$ for different ice crystal habits and different R_{eff} at wavelengths of $0.87 \mu\text{m}$ and $2.13 \mu\text{m}$.

R_{eff} (μm)	g or $\tilde{\omega}$	<i>mix</i>	<i>plt</i>	<i>scl</i>	<i>agg</i>
20	$g_{0.87}$	0.812	0.908	0.792	0.771
	$g_{2.13}$	0.83	0.928	0.787	0.819
	$\tilde{\omega}_{0.87}$	1	1	1	1
	$\tilde{\omega}_{2.13}$	0.937	0.945	0.937	0.936
25	$g_{0.87}$	0.82	0.92	0.793	0.771
	$g_{2.13}$	0.846	0.94	0.848	0.827
	$\tilde{\omega}_{0.87}$	1	1	1	1
	$\tilde{\omega}_{2.13}$	0.926	0.921	0.912	0.917
30	$g_{0.87}$	0.834	0.931	0.793	0.771
	$g_{2.13}$	0.866	0.948	0.851	0.832
	$\tilde{\omega}_{0.87}$	1	1	1	1
	$\tilde{\omega}_{2.13}$	0.914	0.92	0.905	0.904
35	$g_{0.87}$	0.844	0.936	0.795	0.771
	$g_{2.13}$	0.88	0.953	0.859	0.837
	$\tilde{\omega}_{0.87}$	1	1	1	1
	$\tilde{\omega}_{2.13}$	0.904	0.917	0.885	0.893

of R_{eff} by IPA retrievals based on remotely sensed $I_{\lambda}^{\uparrow,3D}$ was also found by Marshak et al. (2006) who attributed it to shadowing effects in boundary layer clouds. However, in this TC⁴ case study, shadowing effects did not play a significant role in producing the same biases. The effects of cloud illumination and cloud top structure were of minor importance in this case, partly because of the near-zenith sun position, and partly because of the flat cloud top topography, compared to the liquid water clouds studied by Marshak et al. (2006).

6.3.2 Ice Particle Shape Effects

Impact on Cloud Top Reflectance

In order to understand the crystal shape effects on retrieved cloud microphysical properties, first the crystal shape effect on $I_{\lambda}^{\uparrow, \text{IPA}}$ (and hence cloud top reflectance $r_{c, \lambda}^{\text{IPA}}$) is discussed, using MYSTIC-IPA calculations at $0.87 \mu\text{m}$ and $2.13 \mu\text{m}$ wavelength and assuming different ICP. Calculations were made for the nadir track at the observed solar zenith angle of 35° . First, the dependence of $r_{c, \lambda}^{\text{IPA}}$ on τ^{inp} was examined. The non-linear increase of $r_{c, 0.87}^{\text{IPA}}$ with increasing τ^{inp} is illustrated in Figure 6.7a. Assuming *scl* or *agg* leads to higher values of $r_{c, 0.87}^{\text{IPA}}$ than assuming *mix*. The *plt* assumption generally results in lower values of $r_{c, 0.87}^{\text{IPA}}$. This is primarily because the asymmetry factors g of these crystal habits are quite different (cf. Table 6.3). If plotted as $r_{c, 0.87}^{\text{IPA}}$ versus $(1 - g) \cdot \tau^{\text{inp}}$, the curves for the various habits would collapse into a nearly identical set of curves (not shown). Deviations from the logarithmic dependence of $r_{c, 0.87}^{\text{IPA}}$ with increasing τ^{inp} are obvious for $\tau^{\text{inp}} < 12$ for *plt*. This variability of the reflectance for a given τ^{inp} value stems from the variable R_{eff} (g of plates strongly increases with R_{eff} , cf. Table 6.3).

Figure 6.8a shows the ratio of $r_{c, 0.87}^{\text{IPA}}(\text{Key})$ and $r_{c, 0.87}^{\text{IPA}}(\text{mix})$. (Key) refers to the different particle habits described in the ice cloud parameterization by Key et al. (2002) that were used

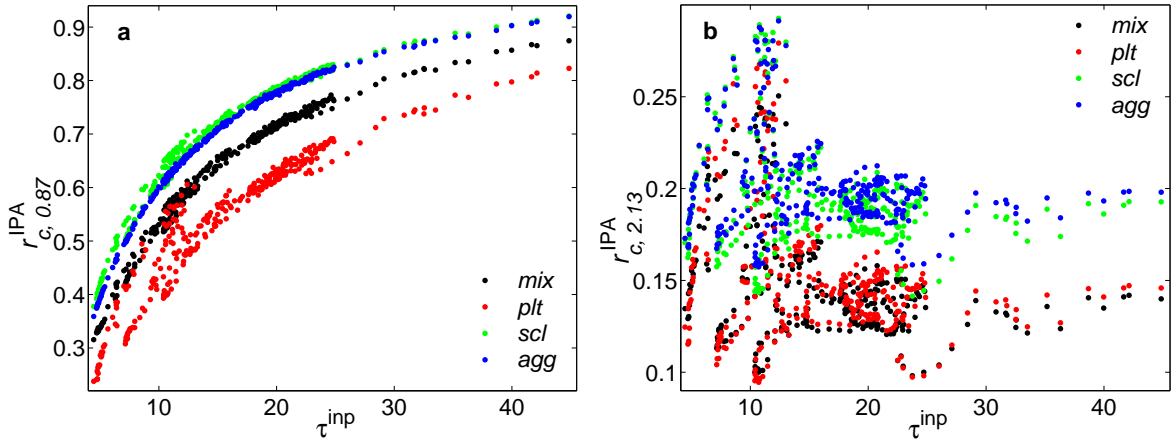


Figure 6.7: (a) $r_{c,0.87}^{IPA}$ versus τ_{inp} and (b) $r_{c,2.13}^{IPA}$ versus τ_{inp} assuming four different crystal shapes (*mix*, *plt*, *scl*, *agg*).

in the calculations (*plt*, *scl*, *agg*). At non-absorbing wavelengths (i.e., $0.87 \mu\text{m}$) the differences between various ICP become less significant with increasing τ because cloud reflectance becomes saturated and is approaching unity at $\tau_{inp} > 45$. Multiple scattering washes out the differences in the single-scattering properties of the various crystal habits. The same finding of diminishing crystal shape effects with increasing τ was made by Wendisch et al. (2005) for irradiances at scattering wavelengths.

Figure 6.7b shows $r_{c,\lambda}^{IPA}$ at the absorbing wavelength ($2.13 \mu\text{m}$) versus τ_{inp} . $r_{c,2.13}^{IPA}$ determined using *scl* or *agg* lead to higher values of $r_{c,2.13}^{IPA}$ compared to *mix* and *plt*. The fact that $r_{c,2.13}^{IPA}$ using the different single habits of the ICP by Key et al. (2002) are generally higher than $r_{c,2.13}^{IPA}$ of the *mix* can be explained as follows: As presented in Table 4.1 the *mix* does not only consist of plates, columns, and aggregates but also of droxtals (small crystals) and bullet-rosettes (large crystals) which are not considered separately here. $r_{c,2.13}^{IPA}$ are found to saturate at a crystal shape-dependent upper limit. This limit is reached at smaller optical depths than for non-absorbing wavelengths (at around $\tau_{inp} \approx 12$). Due to absorption, the limiting asymptotic value of cloud top reflectance is lower than unity (about 0.14 for *mix* and *plt*, and 0.2 for *scl* and *agg*). Its value depends largely on the single scattering albedo (and the asymmetry parameter) which in turn depend on the crystal habit (cf. Table 6.3). To sum things up, that means from $\tau_{inp} \approx 12$ onward, a constant $r_{c,2.13}^{IPA}$ value which is dependent on crystal habit is reached (cf. Figure 6.7b).

This is also shown in Figure 6.8b, where the ratio of $r_{c,2.13}^{IPA}(\text{Key})$ and $r_{c,2.13}^{IPA}(\text{mix})$ is shown. Observed shape-induced differences in $r_{c,2.13}^{IPA}$ were independent of τ_{inp} for $\tau_{inp} > 12$. Wendisch et al. (2005) found that for irradiances at absorbing wavelengths the shape effects increased with increasing τ . However, this was for clouds with $\tau < 7$ only. As shown, in the limit of larger τ , $r_{c,2.13}^{IPA}$ also becomes saturated and approaches an upper limit which depends on the single scattering albedo and the asymmetry parameter.

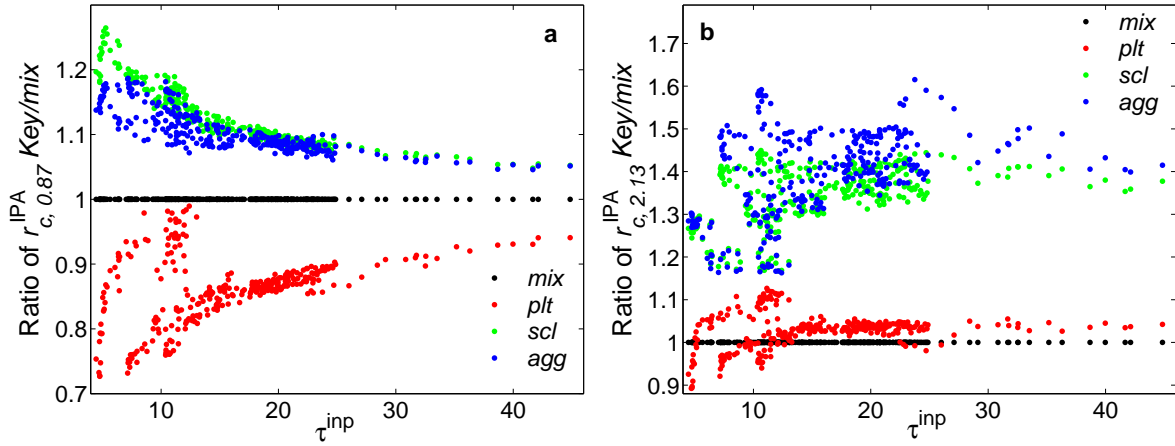


Figure 6.8: a) Ratio of $r_{c,0.87}^{\text{IPA}}(\text{Key})$ to $r_{c,0.87}^{\text{IPA}}(\text{mix})$ versus τ^{inp} . b) Ratio of $r_{c,2.13}^{\text{IPA}}(\text{Key})$ to $r_{c,2.13}^{\text{IPA}}(\text{mix})$ versus τ^{inp} . Key refers to *plt*, *scl*, *agg*.

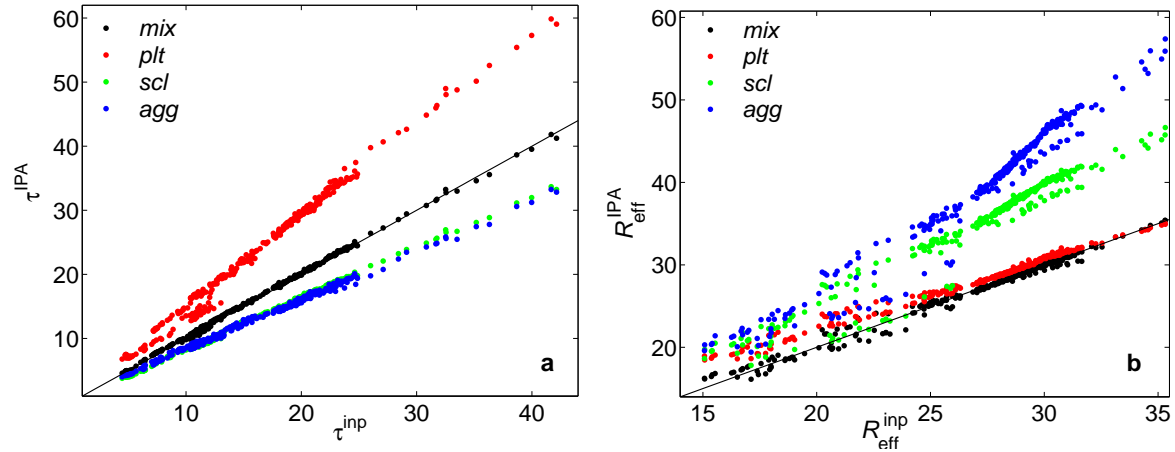


Figure 6.9: (a) Retrieved τ^{IPA} versus τ^{inp} and (b) $R_{\text{eff}}^{\text{IPA}}$ versus $R_{\text{eff}}^{\text{inp}}$.

Impact on Retrieved Microphysical Cirrus Properties

Figures 6.9a and 6.9b show the MYSTIC-IPA based τ^{IPA} and $R_{\text{eff}}^{\text{IPA}}$ values as a function of the values in the original input cloud, for all pixels along the nadir flight track. When using the LUT based on *mix*, one retrieves the same values (black symbols on the 1:1 line) because this is the same ICP as used in the MYSTIC-IPA calculations. When using other ICP for the generation of LUT such as *plt*, *scl*, and *agg*, the retrieval results differ from the values in the input cloud. Highest values of τ^{IPA} with a mean of 23 (cf. Table 6.4) are retrieved assuming *plt* while using *scl* and *agg* results in smaller values of τ^{IPA} averaging at 13 (always compared to using *mix*). Similar findings were reported by Francis et al. (1998) and McFarlane et al. (2005) and also agree with the results presented in Section 5.1.1. Time series of τ^{IPA} under all considered shape assumptions (*mix*, *plt*, *scl*, *agg*) are illustrated in

Table 6.4: Means and standard deviations (σ) of retrieved τ and R_{eff} for the TC⁴ case study based on IPA calculations of I_{λ}^{\uparrow} under the assumption of different ice particle shapes.

	τ^{IPA}		$R_{\text{eff}}^{\text{IPA}}$ (μm)	
	Mean	σ	Mean	σ
<i>mix</i>	16.1	7.1	27.2	4.5
<i>plt</i>	23.3	10.6	28.3	3.8
<i>scl</i>	13.1	5.8	35.0	6.9
<i>agg</i>	12.9	5.5	39.6	9.0

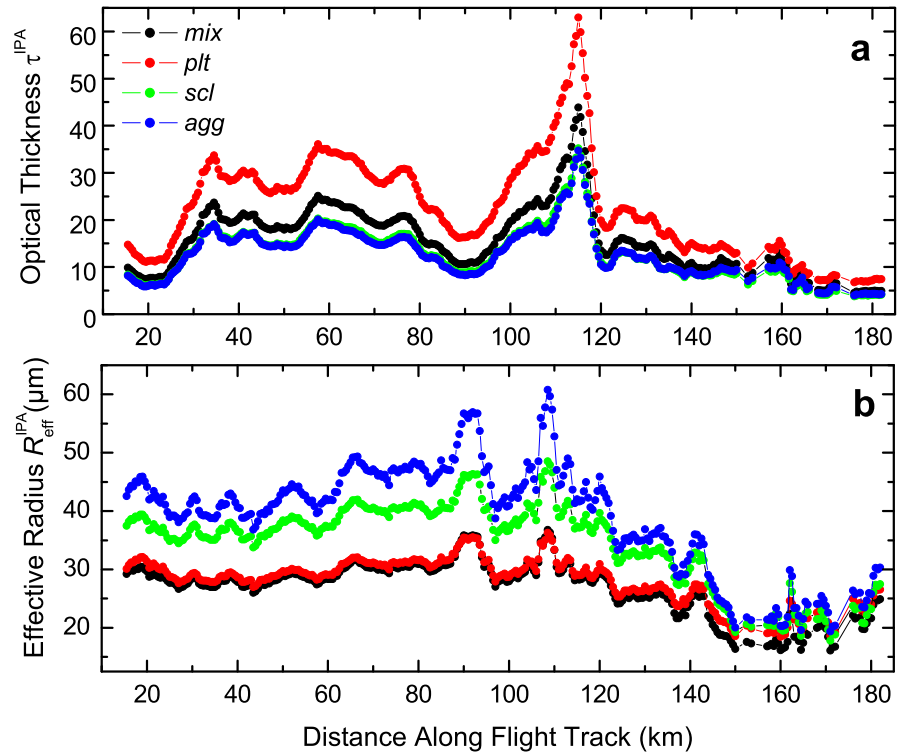


Figure 6.10: Time series of TC⁴ retrieval results along nadir track of the ER-2 under different shape assumptions. a) shows τ^{IPA} and b) $R_{\text{eff}}^{\text{IPA}}$.

Figure 6.10a. As for retrieved $R_{\text{eff}}^{\text{IPA}}$, the assumption of *scl* or *agg* leads to larger values of $R_{\text{eff}}^{\text{IPA}}$ (averaging at $35 \mu\text{m}$ and $40 \mu\text{m}$, respectively, cf. Table 6.4) whereas using the LUT based on *plt* results in $R_{\text{eff}}^{\text{IPA}}$ similar to the ones retrieved using *mix* (mean values of $28 \mu\text{m}$ and $27 \mu\text{m}$, respectively). To some extent, these results differ from the ones presented in Section 5.1.2 for the CIRCLE-2 case studies. Differences are attributed to the fact that in the CIRCLE-2 case studies cirrus of much smaller optical thickness were observed. As shown in Section 6.3.3, the shape effect in retrieved $R_{\text{eff}}^{\text{IPA}}$ depends on τ^{inp} (for optical thicknesses smaller than 12). This effect can also be seen in Figure 6.10b, where time series of $R_{\text{eff}}^{\text{IPA}}$ under all considered shape assumptions (*mix*, *plt*, *scl*, *agg*) are shown.

6.3.3 3D versus Shape Effects

In this Section, the relative importance of 3D cloud structure and ice crystal habit is assessed. For that reason, measures of 3D cloud structure (Γ) and ice crystal habit (Ψ) are introduced. Γ_τ and $\Gamma_{R_{\text{eff}}}$ are defined as ratio between the LUT retrieval results based on MYSTIC-3D calculated radiances and the original values of the input cloud. They serve as measure of 3D effects:

$$\Gamma_\tau = \frac{\tau^{3\text{D}}}{\tau^{\text{inp}}} \quad \text{and} \quad \Gamma_{R_{\text{eff}}} = \frac{R_{\text{eff}}^{3\text{D}}}{R_{\text{eff}}^{\text{inp}}}. \quad (6.5)$$

Ψ_τ and $\Psi_{R_{\text{eff}}}$ are defined as ratio between the retrieval results based on MYSTIC-IPA calculations and the original values of the input cloud:

$$\Psi_\tau = \frac{\tau^{\text{IPA}}}{\tau^{\text{inp}}} \quad \text{and} \quad \Psi_{R_{\text{eff}}} = \frac{R_{\text{eff}}^{\text{IPA}}}{R_{\text{eff}}^{\text{inp}}}. \quad (6.6)$$

Ψ is a measure of the effects of crystal habit on the retrieval results. While the MYSTIC-IPA calculations ($\tau, R_{\text{eff}} \rightarrow I_\lambda^\uparrow$) are based on *mix*, the LUT-based retrievals ($I_\lambda^\uparrow \rightarrow \tau, R_{\text{eff}}$) use *scl*, *agg*, and *plt*. A LUT assuming *mix* is also used in the retrievals to verify that it reproduces the same values for τ and R_{eff} as those in the original cloud field (cf. Section 6.2.3). For simplicity, the labels for the individual habits are omitted on the Ψ symbols. *mix* is chosen as reference habit because it is used in MODIS Collection-5 standard ice cloud retrievals.

Figure 6.11a shows Γ_τ and Ψ_τ as function of τ^{inp} . The black crosses mark 3D effects and the colored symbols the shape effects. Both have roughly the same magnitude with a maximum over- and underestimation of τ of 50%. The shape-ratios (Ψ_τ) are constant with τ^{inp} : Using *plt* for the retrievals leads to an overestimation of τ^{inp} by nearly 50%; using *scl* or *agg* results in an underestimation by approximately 20% (in agreement with Eichler et al. (2009)). In contrast, Γ_τ ranges between 0.6–1.4 and decreases from values around unity at zero optical thickness to about 0.6 for $\tau^{\text{inp}} = 40$. The growing extent of underestimation of τ with increasing τ can be viewed as direct consequence of radiative smoothing of the reflectance fields. In the absence of shadows, photons are effectively redistributed from areas of maximum optical thickness to the surroundings. Since LUT-techniques do not correct for this net horizontal transport, optical thickness is underestimated in optically thick regions, and overestimated elsewhere. In clear-sky or optically very thin areas ($\tau < 3$), photons may

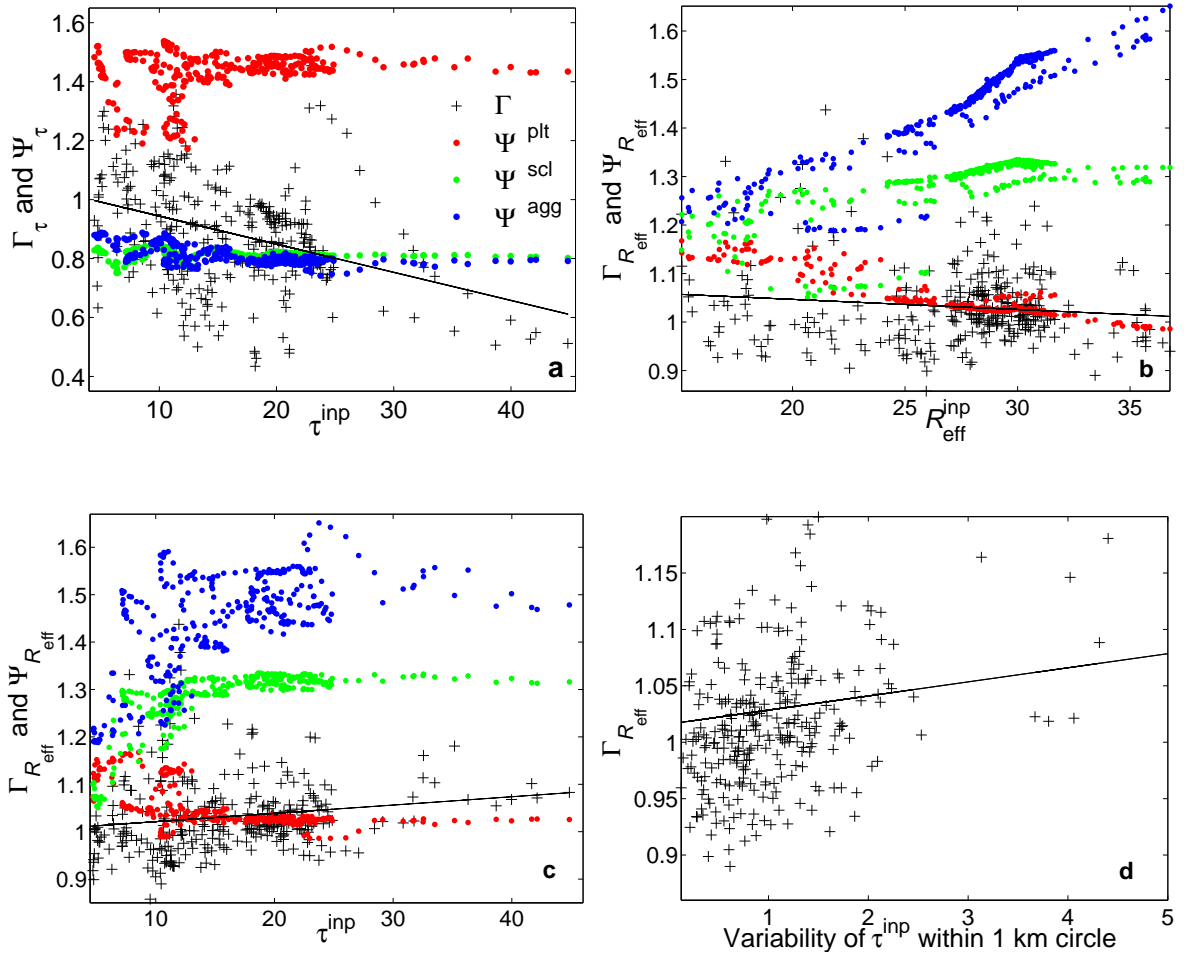


Figure 6.11: (a) Γ_τ and Ψ_τ versus τ^{inp} . (b) $\Gamma_{R_{\text{eff}}}$ and $\Psi_{R_{\text{eff}}}$ versus $R_{\text{eff}}^{\text{inp}}$. (c) $\Gamma_{R_{\text{eff}}}$ and $\Psi_{R_{\text{eff}}}$ versus τ^{inp} . (d) $\Gamma_{R_{\text{eff}}}$ versus variability of τ^{inp} within a circle of 1 km radius. In (a)–(d), Γ is indicated by black crosses, linear fits of Γ are shown by the black line.

even get absorbed at the surface. As shown in Section 6.3.1, over- and underestimation do not cancel each other out, and τ is underestimated by 12% on domain-average. Part of this net underestimation may be because of surface absorption. For small τ , under- and overestimation of τ seems to be equally likely (40%). Linear regression shows that $\Gamma_\tau \rightarrow 1$ for $\tau^{\text{inp}} \rightarrow 0$. Potentially, the dependence of Γ_τ on τ (slope) could be a useful indicator for the impact of cloud heterogeneity on retrievals.

The dependence of $\Gamma_{R_{\text{eff}}}$ and $\Psi_{R_{\text{eff}}}$ on $R_{\text{eff}}^{\text{inp}}$ is shown in Figure 6.11b. $\Gamma_{R_{\text{eff}}}$ generally ranges between 0.9–1.1. Larger values (>1.1 , more than 10% overestimation) were observed when low-level clouds were present. It slightly decreases with increasing $R_{\text{eff}}^{\text{inp}}$. On average, $\Gamma_{R_{\text{eff}}} \approx 1.04$ (4% overestimation). Shape-related biases in R_{eff} can amount to 60% for largest observed crystals ($R_{\text{eff}} = 35 \mu\text{m}$). $\Psi_{R_{\text{eff}}}$ strongly depends on the chosen ICP: When using *agg* in the retrieval, $\Psi_{R_{\text{eff}}}$ increases from 1.2 to 1.6 with increasing $R_{\text{eff}}^{\text{inp}}$. For *scl*, $\Psi_{R_{\text{eff}}}$ has a constant value of 1.3 while it decreases from 1.15 to 1 for *plt*. The different functional dependence of $\Psi_{R_{\text{eff}}}$ for *agg*, *scl*, and *plt* can be ascribed to a different dependence of the single scattering albedo ($\tilde{\omega}$) at $2.13 \mu\text{m}$ on R_{eff} for the different crystal habits (cf. Table 6.3). The magnitude of the shape-related bias is comparable to that of 3D effects only for *plt*, and exceeds it by far for *agg* and *scl*. In this case study, the choice of habit has a much larger impact on size retrievals than 3D effects. Note that the largest habit-related bias in τ is observed for *plt* (red dots), while *agg* (blue dots) introduce the largest bias for R_{eff} . The reason is that at the non-absorbing wavelength, *plt* exhibits a strong forward peak in the scattering phase function, thus leading to the most pronounced shape effect in the retrieval of τ (due to the asymmetry factor). In contrast, at $2.13 \mu\text{m}$ the $\tilde{\omega}$ of *agg* or *scl* for a given $R_{\text{eff}}^{\text{inp}}$ generally differ from that of the *mix*, resulting in high $\Psi_{R_{\text{eff}}}$. The $\tilde{\omega}$ of *plt* is generally more similar to that of *mix* thus leading to a good agreement of R_{eff} (cf. Table 6.3).

In Figure 6.11c, $\Gamma_{R_{\text{eff}}}$ and $\Psi_{R_{\text{eff}}}$ are displayed as function of τ^{inp} . As described in Section 6.3.1, multi-layer effects with optically thin cirrus and patches of low-level clouds are responsible for extremely high (>1.1) or low (<0.9) values of $\Gamma_{R_{\text{eff}}}$. Horizontal inhomogeneities result in $0.9 < \Gamma_{R_{\text{eff}}} < 1.1$. The linear fit of $\Gamma_{R_{\text{eff}}}$ in Figure 6.11c shows that 3D cloud effects on R_{eff} generally cause an overestimation of R_{eff} with increasing τ^{inp} . $\Gamma_{R_{\text{eff}}} \sim 1$ is extrapolated for $\tau^{\text{inp}} \rightarrow 0$. For $\tau^{\text{inp}} \approx 40$, $\Gamma_{R_{\text{eff}}}$ reaches about 1.08. The $\Psi_{R_{\text{eff}}}$ are independent of τ for $\tau^{\text{inp}} > 12$, and larger in magnitude than $\Gamma_{R_{\text{eff}}}$ (up to 1.6 for *agg*). For $\tau^{\text{inp}} < 12$, $\Psi_{R_{\text{eff}}}(\tau)$ have about the same magnitude as $\Gamma_{R_{\text{eff}}}(\tau)$. They increase (for *scl* and *agg*) or decrease (for *plt*) for $5 < \tau^{\text{inp}} < 12$. In optically thick regions of the cloud, the retrieval of R_{eff} is more influenced by crystal habit effects than cloud heterogeneity effects.

Finally, we tested if a systematic dependence of $\Gamma_{R_{\text{eff}}}$ or Γ_τ on the cloud optical thickness variability can be found. The cloud optical thickness variability was parameterized by the standard deviation of τ^{inp} within a circle of 1 km radius around each individual pixel. While Γ_τ did not show any systematic trend, $\Gamma_{R_{\text{eff}}}$ is slightly increasing with cloud variability. This is shown in Figure 6.11d. $\Gamma_{R_{\text{eff}}} \sim 1$ is extrapolated for a cloud with zero optical thickness variability within a 1 km circle. The finding that 3D retrieval biases do not (or only insignificantly) depend on the magnitude of cloud optical thickness variability is somewhat surprising. Instead, we found that 3D retrieval biases depend on the values of τ and R_{eff} themselves.

In view of the presented results, it can be concluded that locally both, the cirrus heterogeneity effects (Γ) and the ice crystal habit effects (Ψ), can be of the same magnitude (up to 50 % over- and underestimation of cirrus retrieval results), with different dependencies on cirrus optical thickness, effective radius, and optical thickness variability. However, on domain average, shape effects were found to bias the retrievals more strongly than 3D effects.

7 Summary, Conclusions, and Outlook

7.1 Summary and Conclusions

Within the scope of this work two central questions were addressed. On the basis of spectral radiance measurements and radiative transfer simulations the influence of

- Ice crystal shape and
- Cirrus spatial heterogeneity

on the remote sensing of cirrus optical thickness τ and effective crystal radius R_{eff} was investigated. Moreover, the effect of ice crystal habit variation on cirrus radiative forcing was analyzed. The study consists of two parts. In the first part, measurements of spectral upwelling radiance data (I_{λ}^{\uparrow}) with the SMART-Albedometer during the CIRCLE-2 field experiment were described. Based on these data, 1D radiative transfer calculations were employed to retrieve τ and R_{eff} . By using different ice particle shape assumptions in the retrieval, the influence of crystal shape on retrieved τ and R_{eff} was evaluated. Also, the radiative forcing of the two CIRCLE-2 cirrus case studies was investigated with a focus on the crystal shape effect. In the second part, the relative importance of cirrus spatial heterogeneity and ice crystal shape on the reflectance-based retrieval of τ and R_{eff} was quantified. For that purpose, 3D and IPA radiative transfer calculations were performed for a model cloud case that was generated from data collected during the TC⁴ experiment. Results of both parts are summarized subsequently.

7.1.1 Ice Particle Shape Effects

Within the frame of this work, the SMART-Albedometer was installed on a high-altitude pressurized aircraft for the first time. Data of I_{λ}^{\uparrow} presented here were obtained with that instrument during the CIRCLE-2 aircraft field experiment in May 2007. These I_{λ}^{\uparrow} data were converted to measured spectral cloud top reflectances r_c . Then, r_c in a wavelength range for which ice is mostly scattering solar radiation (0.6–0.7 μm , largely dependent on τ) as well as a spectral band in which ice is absorbing solar radiation (1.5–1.65 μm , controlled by R_{eff}) were calculated by 1D radiative transfer simulations. Thus, lookup tables of r_c were generated for a range of τ and R_{eff} . A retrieval process was simulated: the measured bispectral r_c values were mapped back onto values of cirrus optical thickness and effective crystal radius, as is usually done in standard lookup table (LUT) techniques. Simulations were repeated under different particle habit assumptions. Bulk optical properties were described by the ice-cloud parametrizations of Key et al. (2002) for single particle habits (hexagonal plates (*plt*),

solid columns (*scl*), hollow columns (*hcl*), rough aggregates (*agg*), planar rosettes (*rs4*), and spatial rosettes (*rs6*) as well as by the ice-cloud parametrization of Baum et al. (2005b) for a mixture of particle habits (*mix*). In addition, ice spheres (*sph*) for which optical properties are derived from Mie-theory were assumed.

Cirrus retrievals were made for two different surface albedos (land (case study P1), and water (case study P2)). Retrieved τ values were compared to lidar-derived τ . R_{eff} were compared to values determined from microphysical measurements. Values were found to agree reasonably. Special attention was paid to the influence of assumed crystal shape on the retrieved τ and R_{eff} . The analysis showed that the influence of ice particle habit on τ is larger than on R_{eff} . The obtained percentage differences between retrieved τ of up to 70 % compare well with values from literature. For example Key et al. (2002) and McFarlane et al. (2005) found maximum shape-induced differences of 60 % and 50 %, respectively. Concerning percentage differences in R_{eff} retrieved under various habit assumptions, the results of Knap et al. (1999) (11 %) and McFarlane et al. (2005) (30 %) are confirmed by the case studies of this work. Here, differences in retrieved R_{eff} were on the order of 20 %. McFarlane and Marchand (2008) came to the conclusion that the assumption of a single particle habit is likely not appropriate in all situations and mentioned that studies have indicated that habit mixtures are better able to match in situ measured microphysical properties. Wendisch et al. (2007) also emphasize that the maximum effects of assumed uniform ice crystal shape serve as boundaries between which effects for mixtures of ice crystals range. Here, this issue was paid attention to by making calculations on the basis of *mix* which is used in the ice cloud products of the MODIS Collection-5 retrievals. For the two case studies, values of τ and R_{eff} obtained assuming *mix* were indeed found to range within the boundaries spanned by single habit assumptions.

For the two CIRCLE-2 case studies, the influence of ice particle habit on instantaneous cirrus radiative forcing at $\theta_0 = 36^\circ$ was discussed separately for the solar radiative forcing ΔF^{sol} , the thermal IR radiative forcing ΔF^{IR} , and the broadband net radiative forcing ΔF^{net} . To address these questions, extensive solar and thermal IR radiative transfer simulations were made for top-of-atmosphere (TOA) and below the cirrus at bottom-of-atmosphere (BOA). In the presence of a cirrus, the amount of solar radiation incident on the surface is reduced and the amount of solar radiation reflected to space is increased. Both effects lead to a cooling in the solar wavelength range. The observed cirrus was found lead to a τ -dependent solar radiative cooling of the same magnitude at BOA and TOA. As an average over all assumed particle habits, the instantaneous ΔF^{sol} amounted to -150 W m^{-2} during P1 and -90 W m^{-2} during P2. Strongest instantaneous ΔF^{sol} was obtained assuming *scl* or *agg*, while assuming that the cirrus consists of *plt* or *sph* resulted in smallest solar cooling values. Different ice particle shape assumptions led to percentage differences in ΔF^{sol} of up to 46 %. Diurnal means of ΔF^{sol} were calculated. At TOA they ranged between $-80 - -117 \text{ W m}^{-2}$ at P1 and $-52 - -84 \text{ W m}^{-2}$ at P2.

The dependence of ΔF^{sol} on τ was linear. Thus, the solar forcing efficiency $S\Delta F^{\text{sol}}$ was determined as slope of the linear fit of ΔF^{sol} against τ . As average of the diurnal variation of $S\Delta F^{\text{sol}}$, it was found that for a given τ the cirrus solar radiative cooling over the dark water surface was 50–60 % stronger than over land.

In the thermal IR range, cirrus have a warming effect because they emit at lower temperatures

than the surface. For the CIRCLE-2 case studies, instantaneous ΔF^{IR} at TOA was found to be much stronger (factor of six) than at BOA. $\Delta F_{\text{TOA}}^{\text{IR}}$ amounted to about 114 W m^{-2} (P1) and 76 W m^{-2} (P2) while $\Delta F_{\text{BOA}}^{\text{IR}}$ averaged at 19 W m^{-2} (P1) and 13 W m^{-2} (P2). Shape-induced differences in values of ΔF^{IR} were much smaller than in ΔF^{sol} and increased with decreasing τ . Differences in ΔF^{IR} amounted to 5% during P1 ($\bar{\tau} = 3.4$ assuming *mix*) and 11% during P2 ($\bar{\tau} = 1.3$ assuming *mix*).

By adding ΔF^{sol} and ΔF^{IR} , ΔF^{net} was determined. During P1 and P2, the instantaneous net radiative forcing of the cirrus at BOA was negative with shape-averaged values of -133 W m^{-2} (P1) and -77 W m^{-2} (P2). Crystal shape induced differences in ΔF^{net} amounted to about 50% at maximum. At TOA, the sign of the radiative effect depended on ice crystal habit and τ . In general, a radiative cooling was observed with average values of -35 W m^{-2} (P1) and -11 W m^{-2} (P2). However, for optically thin cirrus a warming effect was calculated under the assumption of plates and ice spheres. Thus, the shape effect in ΔF^{net} at TOA is much stronger than at BOA, it even exceeds 100%. Summarizing, in this work it was shown that the cirrus radiative forcing strongly depends on assumed ice particle habit. Calculated values of cirrus radiative forcing are affirmed by the findings of Chen et al. (2000); Mace et al. (2006a); Wendisch et al. (2007); Dupont and Haefelin (2008).

7.1.2 Relative Importance of Ice Particle Shape and 3D Cloud Structure

In the second part of this work, the relative impact of single-scattering properties and cloud variability in ice clouds on the remote sensing products τ and R_{eff} was examined. The dataset was based on a cloud field that was encountered during the NASA TC⁴ experiment conducted in Costa Rica in summer 2007. From MODIS Airborne Simulator (MAS) and Cloud Radar System (CRS) data gathered with the ER-2 aircraft, a cloud field for input to 3D radiative transfer calculations was constructed. In this cloud field of 500 m horizontal resolution, cirrus extinction varied with height albeit the effective radius was vertically homogeneous. The radiative transfer model MYSTIC was run in full 3D and IPA mode and again the ice crystal scattering properties of Key et al. (2002) and Baum et al. (2005b) were used. Upwelling radiances (and hence cloud top reflectances r_c) along the flight track of the ER-2 were calculated for two wavelengths ($0.87 \mu\text{m}$ (a function of τ) and $2.13 \mu\text{m}$ (strongly dependent on R_{eff})). These r_c values were matched with the best-fitting lookup table values of cirrus optical thickness and effective crystal radius. The LUTs were pre-calculated with the DISORT2 1D radiative transfer model for different ice particle habits: the mixture of particle habits (*mix*); hexagonal plates (*plt*), solid columns (*scl*), and rough aggregates (*agg*). In the first step, the full 3D calculations simulated the upwelling radiance field along nadir track that a satellite imager would detect for the given cloud field. These radiances were then converted to cloud top reflectances and served as input to the bispectral 1D retrieval. In order to estimate the magnitude of 3D effects, the resulting LUT-based retrievals were compared to the original input cloud field. The metric Γ was defined as ratio between these retrieval results and the input cloud optical thickness τ^{inp} or effective radius $R_{\text{eff}}^{\text{inp}}$. To cancel out shape effects, the retrievals were based on the same crystal scattering properties as the 3D radiance calculations (*mix*).

In the second step, the ice particle shape effects were examined, and all four pre-calculated

LUTs (*mix*, *plt*, *scl*, *agg*) were used to retrieve optical thickness and effective radius. In order to single out the shape effects, net horizontal photon transport in the 3D model was disabled in the radiance calculations, i.e., IPA mode model runs were used. The ratio between the retrieved values and the original input values, Ψ , was introduced as measure of the ice crystal habit effect.

Both Γ and Ψ were analyzed as function of τ^{inp} , $R_{\text{eff}}^{\text{inp}}$, and cloud optical thickness variability. On the domain average, cirrus optical thickness is underestimated by 12 %, and effective ice particle radius is overestimated by 4 % due to 3D effects. In comparison, shape effects may bias the retrieval much more strongly: Assuming *plt* rather than the standard *mix* in the retrievals leads to an overestimation of optical thickness of up to 50 % (42 % on average); the R_{eff} is overestimated by up to 60 % (45 % on average) when assuming *agg* rather than *mix*. The shape-induced biases in optical thickness are constant in thick and thin cloud areas. In contrast, the 3D bias in τ ranges from 60 % underestimation to 40 % overestimation locally. Large τ values are generally underestimated by 3D based modelled r_c . Both under- and overestimation of τ occur in optically thin areas. The shape-induced R_{eff} biases depend strongly on ice particle size itself. While for small crystals, *plt*, *scl*, and *agg* are moderately biased positive with respect to *mix* (15–25 %), they overestimate the effective radius by up to 60 % for large crystal sizes. By comparison, 3D effects cause underestimations of 10 % to overestimations of 20 %. In areas with pronounced multi-layer structure, the effective crystal radius is overestimated by even up to 30 %.

It was thus demonstrated that locally both - shape effects and 3D effects - can be of the same magnitude (up to about 40-60 % over- and underestimation of τ and R_{eff}) with different dependencies on cirrus optical thickness, effective radius, and optical thickness variability. However, on domain average, shape effects bias the retrieval of τ and R_{eff} more strongly than 3D effects.

7.2 Outlook

7.2.1 Sensitivity Studies

It is emphasized that results presented here are only valid for the given cirrus case studies and that no generalization of the results should be attempted. Instead, it would be interesting to address the issue of relative importance of shape effect versus spatial inhomogeneity effect for an optically thinner cirrus and to determine the influence of the 3D cloud structure effect on the retrieval of τ and R_{eff} at different horizontal resolutions (for example 100 m and 1000 m). An issue that requires further study is the sensitivity of the ice crystal shape effect and the cirrus spatial inhomogeneity on variations in solar zenith angle. Another subject that is beyond the scope of this work is the question of the effect of 3D cloud structure on cirrus radiative forcing. The 3D model cloud based on measurements performed during the TC⁴ experiment can serve as input cloud to such calculations. Research addressing that question is planned in the near future.

7.2.2 Validation of Satellite Retrievals

While field experiments and in situ observations provide detailed information about cirrus microphysical properties, they are limited geographically and temporally (McFarlane et al., 2005). Thus, the determination of cirrus properties on larger spatial and time scales requires satellite data. As stated by Gonzalez et al. (2002), numerous approaches based on the interpretation of the radiation reflected by cirrus in different wavelength bands have been developed to infer τ and R_{eff} from radiances measured by satellite borne instruments. Formenti and Wendisch (2008) emphasize that aircraft measurements and satellite observations are synergistic tools both having their own strengths and weaknesses. Airborne spectral radiance measurements above cirrus with concurrent lidar and microphysical measurements as presented in this work provide a tool to verify satellite cirrus retrieval algorithms of τ and R_{eff} . However, care must be taken when comparing measurements of an instrument with a fine spatial resolution of the cloud (such as the SMART-Albedometer flying closely above cloud top with a footprint of several meters to few tens of meters) with satellite measurements obtained at much coarser spatial resolution on the order of several hundred meters. Comparisons of retrieved microphysical properties might thus be affected by the differences in pixel resolution, i.e., by the unresolved subgrid variability in the satellite measurements. As stated in Marshak et al. (2006), ignoring subpixel variability produces a negative bias in retrieval results due to the non-linear relationship between r_c and τ or R_{eff} . In addition, precise temporal and spatial coordination of aircraft flights with satellite overpasses is required for validation missions so that results are not affected by the temporal evolution and advection of the cloud. Several field programs such as the Cirrus Regional Study of Tropical Anvils and Cirrus Layers - Florida Area Cirrus Experiment [CRYSTAL-FACE, (Jensen et al., 2004)] and the TC⁴ experiment succeeded in gathering validation data for cloud property retrieval algorithms. However, Davis et al. (2009) highlight that for satellite versus aircraft-based remote sensing data of optical/microphysical properties there have been relatively few comparisons up to date. In future campaigns, data obtained with the SMART-Albedometer can be used to validate satellite retrievals provided that the required flight strategies needed for concurrent aircraft and satellite measurements are realized.

7.2.3 Tandem Measurement Platform

Experimental studies with *concurrent* measurements of radiometric quantities reflected by a cirrus and microphysical properties in the cirrus could also be used as a tool to validate reflectance-based cirrus retrievals. Within the scope of the Collaborative Research Center 641: TROPICE "The Tropospheric Ice Phase" a tandem platform allowing to do such collocated measurements with one aircraft has been developed and is described by Frey et al. (2009). The platform consists of a Learjet 35A research aircraft and the AIRcraft Towed Sensor Shuttle (AIRTOSS), which is an instrumented drag-body towed by the Learjet as presented in Figure 7.1. A first proof-of-concept field campaign of the platform was made in September 2007 at Hohn Airport, Northern Germany.

Among other instruments, the Learjet was equipped with the SMART-Albedometer in a configuration with two optical inlets to determine cloud top reflectance r_c (cf. Figure 7.1).

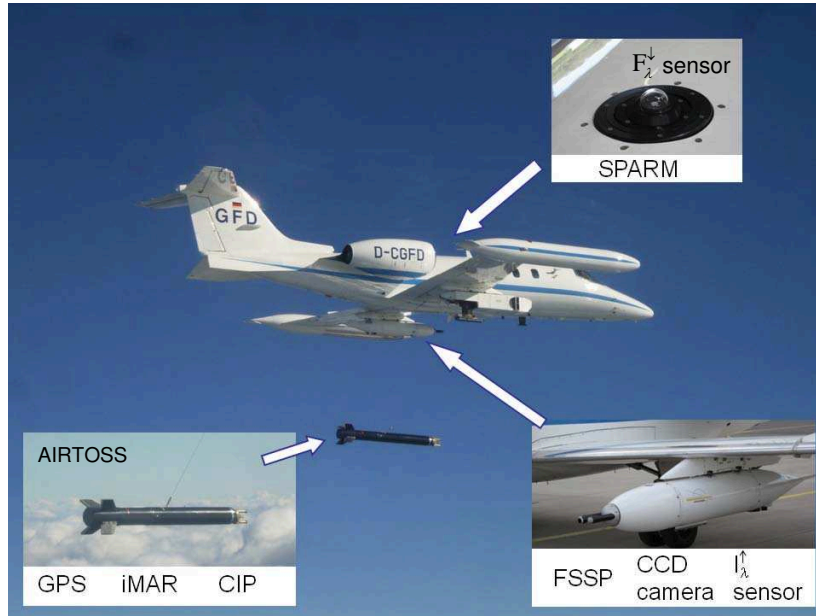


Figure 7.1: Instrumentation of the tandem platform for cloud-radiation interaction studies consisting of a Learjet 35A research aircraft and the drag-body AIRTOSS.

A downward-looking radiance inlet to measure I_{λ}^{\uparrow} was installed in the wingpod. On the top part of the aircraft fuselage a horizontally stabilized upward-looking irradiance sensor to measure F_{λ}^{\downarrow} was mounted. As emphasized in Wendisch et al. (2001), the active levelling of irradiance inlets is essential to guarantee the correct distinction of the upward and downward hemisphere. The Stabilized Platform for Airborne Radiation Measurements (SPARM) developed by *enviscope GmbH* was initially configured for low altitude measurements with unpressurized aircraft. The company put much effort into the modification of SPARM for operation on high-altitude pressurized aircraft such as the Learjet. Major modifications included the development of weather protection of the mechanical and electronic components which are mounted outside the pressurized cabin, wind protection to reduce dynamic pressure upon and turbulent flow around the sensing unit and to ensure proper moving of the stabilized optical inlet, and heating of mechanical components. The performance of SPARM was tested. It was found that SPARM is able to adjust for aircraft attitude changes (roll- and pitch angles) in the range of $\pm 5^{\circ}$ with a precision of $\pm 0.2^{\circ}$ during flight manoeuvres. This assures that misalignment-related uncertainties of the measured F_{λ}^{\downarrow} are less than $< 1\%$ for solar zenith angles $\theta_0 < 70^{\circ}$.

The setup was completed by the AIRTOSS (length = 2.85 m) which was instrumented with a Cloud Imaging Probe (CIP) for measuring cloud microphysical properties, a Global Positioning System (GPS), and an Inertial Navigation System (INS) designed by *iMAR GmbH* for measurements of flight attitudes (pitch and roll angles). The CIP was located at the tip of AIRTOSS (cf. Figure 7.1). It delivers 2D shadow images of cloud particles in a size range of 25–1600 μm in diameter (Baumgardner et al., 2001). Thus, particle shapes, particle size distributions, and number concentrations are obtained from the CIP measurements. Power supply for the AIRTOSS devices is provided by batteries lasting about 1 3/4 hours. The winch for the AIRTOSS is installed beneath the right wing of the Learjet. The cable

dragging AIRTOSS can be extended to up to four kilometres. By varying the towing cable length and the speed of the aircraft, the horizontal and vertical distance between the AIRTOSS and the Learjet can be varied. Thus, truly collocated measurements in two altitudes above, in, or below clouds can be obtained. Proof-of-concept tests of the AIRTOSS included several specific manoeuvres at different altitudes, airspeeds, and towing cable lengths while the attitude of the drag-body was measured. During these manoeuvres AIRTOSS was able to stabilize its flight in such a way that it is considered stable enough to allow radiation and cloud microphysics measurements within the limits imposed by the instruments. For a detailed description of the AIRTOSS performance the reader is directed to Frey et al. (2009).

However, in summary, the proof-of-concept field experiment demonstrated that the novel tandem platform is suitable to perform collocated measurements of radiative and microphysical cloud properties. In the future, it is also planned to implement optical inlets for up- and downwelling irradiance measurements on AIRTOSS as well as an F_{λ}^{\uparrow} optical inlet in the wingpod of the Learjet allowing to measure cloud absorption and transmittance by simultaneous data acquisition above and below the cloud. So far, these cloud-radiation interaction studies could only be realized via a coordination of two aircraft which is more difficult and of course also much more costly. Not to forget, the tandem platform is perfectly suited for simultaneous measurements in and above young contrails which - due to their rather small vertical and horizontal extension (Gounou and Hogan, 2007) - are difficult to capture by two aircraft.

Bibliography

- International Cloud Atlas, Vol. II, World Meteorological Organization (WMO), 1987.
- Anderson, G., Clough, S., Kneizys, F., Chetwynd, J., and Shettle, E.: AFGL Atmospheric Constituent Profiles (0–120 km), Tech. Rep. AFGL-TR-86-0110, AFGL (OPI), Hanscom AFB, MA 01736, 1986.
- Baran, A.: A review of the light scattering properties of cirrus, *J. Quant. Spectrosc. Ra.*, 110, 1239–1260, 2009.
- Baran, A. J. and Labonnote, L. C.: A self-consistent scattering model for cirrus. I: The solar region, *Quart. J. Roy. Meteor. Soc.*, 133, 1899–1912, 2007.
- Barker, H.: A parameterization for computing grid-averaged solar fluxes for inhomogeneous marine boundary layer clouds. Part I: Methodology and homogeneous biases, *J. Atmos. Sci.*, 53, 2289–2303, 1996.
- Baum, B. A., Heymsfield, A. J., Yang, P., and Bedka, S. T.: Bulk scattering properties for the remote sensing of ice clouds. Part I: Microphysical data and models, *J. Appl. Meteor.*, 44, 1885–1895, 2005a.
- Baum, B. A., Yang, P., Heymsfield, A. J., Platnick, S., King, M. D., Hu, Y. X., and Bedka, S. T.: Bulk scattering properties for the remote sensing of ice clouds. Part II: Narrowband models, *J. Appl. Meteor.*, 44, 1896–1911, 2005b.
- Baum, B. A., Yang, P., Nasiri, S., Heidinger, A. K., Heymsfield, A., and Li, J.: Bulk scattering properties for the remote sensing of ice clouds. Part III: High-resolution spectral models from 100 to 3250 cm^{-1} , *J. Appl. Meteor.*, 46, 423–434, 2007.
- Baumgardner, D., Dye, J. E., Gandrud, B. W., and Knollenberg, R. G.: Interpretation of measurements made by the Forward Scattering Spectrometer Probe (FSSP-300) during the airborne arctic stratospheric expedition, *J. Geophys. Res.*, 97, 8035–8046, 1992.
- Baumgardner, D., Jonsson, H., Dawson, W., O'Connor, D., and Newton, R.: The cloud, aerosol and precipitation spectrometer: a new instrument for cloud investigations, *Atmos. Res.*, 59-60, 251–264, 2001.
- Bergeron, T.: On the physics of cloud and precipitation, in *Proceedings 5th Assembly U.G.G.I.*, pp. 156–178, Lisbon, Portugal, 1935.
- Bierwirth, E.: Airborne measurements of the spectral surface albedo over morocco and its influence on the radiative forcing of saharan dust, Ph.D. thesis, Johannes Gutenberg University Mainz, Germany, 2008.

- Bierwirth, E., Wendisch, M., Ehrlich, A., Heese, B., Tesche, M., Althausen, D., Schladitz, A., Müller, D., Otto, S., Trautmann, T., Dinter, T., von Hoyningen-Huene, W., and Kahn, R.: Spectral surface albedo over Morocco and its impact on the radiative forcing of Saharan dust, *Tellus*, 61B, 252–269, 2009.
- Bohren, C. F. and Clothiaux, E. E.: *Fundamentals of atmospheric radiation*, Wiley-VCH Verlag GmbH & Co. KGaA, Weinheim, 2006.
- Bohren, C. F. and Huffman, D. R.: *Absorption and scattering of light by small particles*, Wiley-Interscience, New York, 1998.
- Cahalan, R. and Snider, J.: Marine stratocumulus structure, *Remote Sens. Environ.*, 28, 95–107, 1989.
- Cahalan, R., Ridgway, W., Wiscombe, W., and Bell, T.: The albedo of fractal stratocumulus clouds, *J. Atmos. Sci.*, 51, 2434–2455, 1994.
- Carlin, B., Fu, Q., Lohmann, U., Mace, G., Sassen, K., and Comstock, J.: High-cloud horizontal inhomogeneity and solar albedo bias, *J. Climate*, 15, 2321–2339, 2002.
- Cess, R., Nemesure, S., Dutton, E., DeLuisi, J., Potter, G., and Morcrette, J.-J.: The impact of clouds on the shortwave radiation budget of the surface-atmosphere system: Interfacing measurements and models, *J. Climate*, 6, 308–316, 1993.
- Chandrasekhar, S.: *Radiative transfer*, Oxford University Press, London, UK, 1950.
- Chang, F. L. and Li, Z. Q.: Retrieving vertical profiles of water-cloud droplet effective radius: Algorithm modification and preliminary application, *J. Geophys. Res.*, 108, 4763, 2003.
- Chen, T., Rossow, W., and Zhang, Y.: Radiative effects of cloud-type variations, *J. Climate*, 13, 264–286, 2000.
- Chepfer, H., Goloub, P., Riedi, J., De Haan, J. F., Hovenier, J., and Flamant, P.: Ice crystal shapes in cirrus clouds derived from POLDER/ADEOS-1, *J. Geophys. Res.*, 106, 7955–7966, 2001.
- Chepfer, H., Minnis, P., Young, D., Nguyen, L., and Arduini, R. F.: Estimation of cirrus cloud effective ice crystal shapes using visible reflectances from dual-satellite measurements, *J. Geophys. Res.*, 107, 4730, 2002.
- Chepfer, H., Noel, V., Minnis, P., Baumgardner, D., Nguyen, L., Raga, G., McGill, M. J., and Yang, P.: Particle habit in tropical ice clouds during CRYSTAL-FACE: Comparison of two remote sensing techniques with in situ observations, *J. Geophys. Res.*, 110, D16 204, 2005.
- Chou, M. D., Lee, K. T., and Yang, P.: Parameterization of shortwave cloud optical properties for a mixture of ice particle habits for use in atmospheric models, *J. Geophys. Res.*, 107, 2002.

- Coddington, O., Schmidt, K., Pilewskie, P., Gore, W., Bergstrom, R., Román, M., Redemann, J., Russell, P., Liu, J., and Schaaf, C.: Aircraft measurements of surface spectral albedo and its consistency with ground-based and space-borne observations, *J. Geophys. Res.*, 113, 10.1029/2008JD010089, 2008.
- Comstock, J. M., d’Entremont, R., DeSlover, D., Mace, G. G., Matrosov, S. Y., McFarlane, S. A., Minnis, P., Mitchell, D., Sassen, K., Shupe, M. D., Turner, D. D., and Wang, Z.: An intercomparison of microphysical retrieval algorithms for upper-tropospheric ice clouds, *Bull. Amer. Meteor. Soc.*, 88, 191–204, 2007.
- Cooper, S. J., L’Ecuyer, T. S., Gabriel, P., Baran, A. J., and Stephens, G. L.: Objective assessment of the information content of visible and infrared radiance measurements for cloud microphysical property retrievals over the global oceans. Part II: Ice clouds, *J. Appl. Meteorol.*, 45, 42–62, 2006.
- Cox, C. and Munk, W.: Measurement of the roughness of the sea surface from photographs of the sun’s glitter, *J. Opt. Soc. Am. A.*, 44, 838–850, 1954.
- Davis, S. M., Avallone, L. M., Kahn, B. H., Meyer, K. G., and Baumgardner, D.: Comparison of airborne in situ measurements and Moderate Resolution Imaging Spectroradiometer (MODIS) retrievals of cirrus cloud optical and microphysical properties during the Mid-latitude Cirrus Experiment (MidCiX), *J. Geophys. Res.-Atmos.*, 114, 2009.
- de Reus, M., Borrmann, S., Bansemmer, A., Heymsfield, A. J., Weigel, R., Schiller, C., Mitev, V., Frey, W., Kunkel, D., Kurten, A., Curtius, J., Sitnikov, N. M., Ulanovsky, A., and Ravegnani, F.: Evidence for ice particles in the tropical stratosphere from in-situ measurements, *Atmos. Chem. Phys.*, 9, 6775–6792, 2009.
- Dong, X. Q., Xi, B. K., and Minnis, P.: A climatology of midlatitude continental clouds from the ARM SGP central facility. Part II: Cloud fraction and surface radiative forcing, *J. Climate*, 19, 1765–1783, 2006.
- Dowling, D. R. and Radke, L. F.: A summary of the physical properties of cirrus clouds, *J. Appl. Meteor.*, 29, 970–978, 1990.
- Dupont, J. C. and Haefelin, M.: Observed instantaneous cirrus radiative effect on surface-level shortwave and longwave irradiances, *J. Geophys. Res.*, 113, 2008.
- Edwards, J., Havemann, S., Thelen, J.-C., and Baran, A.: A new parametrization for the radiative properties of ice crystals: Comparison with existing schemes and impact in a GCM, *Atmos. Res.*, 83, 19 – 35, 2007.
- Ehrlich, A.: The impact of ice crystals on radiative forcing and remote sensing of arctic boundary-layer mixed-phase clouds, Ph.D. thesis, Johannes Gutenberg University Mainz, Germany, 2009.
- Ehrlich, A., Bierwirth, E., Wendisch, M., Gayet, J.-F., Mioche, G., Lampert, A., and Heintzenberg, J.: Cloud phase identification of Arctic boundary-layer clouds from airborne spectral reflection measurements: Test of three approaches, *Atmos. Chem. Phys.*, 8, 7493–7505, 2008.

- Eichler, H., Ehrlich, A., Wendisch, M., Mioche, G., Gayet, J.-F., Wirth, M., Emde, C., and Minikin, A.: Influence of ice crystal shape on retrieval of cirrus optical thickness and effective radius: A case study, *J. Geophys. Res.*, 114, D19203, 2009.
- Emde, C. and Mayer, B.: Simulation of solar radiation during a total solar eclipse: A challenge for radiative transfer., *Atmos. Chem. Phys.*, 7, 2259–2270, 2007.
- Findeisen, W.: Kolloidmeteorologische Vorgänge bei Niederschlagsbildung, *Meteor. Z.*, 55, 121–133, 1938.
- Formenti, P. and Wendisch, M.: Combining upcoming satellite missions and aircraft activities, *Bull. Amer. Meteorol. Soc.*, 89, 385–388, 2008.
- Francis, P., Hignett, P., and Macke, A.: The retrieval of cirrus cloud properties from aircraft multi-spectral reflectance measurements during EUCREX '93, *Quart. J. Roy. Meteor. Soc.*, 124, 1273–1291, 1998.
- Frey, W., Eichler, H., de Reus, M., Maser, R., Wendisch, M., and Borrmann, S.: A new airborne tandem platform for collocated measurements of microphysical cloud and radiation properties, *Atmos. Meas. Tech.*, 2, 147–158, 2009.
- Fu, Q.: An accurate parameterization of the solar radiative properties of cirrus clouds in climate models, *J. Climate*, 9, 2058–2082, 1996.
- Fu, Q. and Takano, Y.: On the limitation of using asymmetry factor for radiative transfer involving cirrus clouds, *Atmos. Res.*, 34, 299–308, 1994.
- Futyan, J. M., Russell, J. E., and Harries, J. E.: Determining cloud forcing by cloud type from geostationary satellite data, *Geophys. Res. Lett.*, 32, 2005.
- Garrett, T. J., Gerber, H., Baumgardner, D. G., Twohy, C. H., and Weinstock, E. M.: Small, highly reflective ice crystals in low-latitude cirrus, *Geophys. Res. Lett.*, 30, doi:10.1029/2003GL018153, 2003.
- Gayet, J. F., Auriol, F., Minikin, A., Strom, J., Seifert, M., Krejci, R., Petzold, A., Febvre, G., and Schumann, U.: Quantitative measurement of the microphysical and optical properties of cirrus clouds with four different in situ probes: Evidence of small ice crystals, *Geophys. Res. Lett.*, 29, doi:10.1029/2001GL014342, 2002.
- Gayet, J. F., Ovarlez, J., Shcherbakov, V., Strom, J., Schumann, U., Minikin, A., Auriol, F., Petzold, A., and Monier, M.: Cirrus cloud microphysical and optical properties at southern and northern midlatitudes during the INCA experiment, *J. Geophys. Res.*, 109, doi:10.1029/2004JD004803, 2004.
- Gonzalez, A., Wendling, P., Mayer, B., Gayet, J.-F., and Rother, T.: Remote sensing of cirrus cloud properties in the presence of lower clouds: An ATSR-2 case study during the Interhemispheric Differences in Cirrus Properties From Anthropogenic Emissions (INCA) experiment, *J. Geophys. Res.*, 107, 10.1029/2002JD002535, 2002.

- Gounou, A. and Hogan, R. J.: A sensitivity study of the effect of horizontal photon transport on the radiative forcing of contrails, *J. Atmos. Sci.*, 64, 1706–1716, 2007.
- Grenfell, T. C. and Warren, S. G.: Representation of a nonspherical ice particle by a collection of independent spheres for scattering and absorption of radiation, *J. Geophys. Res.*, 104, 31.697–31.709, 1999.
- Gueymard, C. A.: The sun’s total and spectral irradiance for solar energy applications and solar radiation models, *Solar Energy*, 76, 423–453, 2004.
- Hallett, J. and Mossopp, S. C.: Production of secondary ice particles during riming process, *Nature*, 249, 26–28, 1974.
- Hartmann, D., Moy, L., and Fu, Q.: Tropical convection and the energy balance at the top of the atmosphere, *J. Climate*, 14, 4495–4511, 2001.
- Heymsfield, A. and Miloshevich, L.: Parameterizations for the cross-sectional area and extinction of cirrus and stratiform ice cloud particles, *J. Atmos. Sci.*, 60, 936–956, 2003.
- Heymsfield, A. and Platt, C.: A parameterization of the particle size spectrum of ice clouds in terms of the ambient temperature and the ice water content, *J. Atmos. Sci.*, 41, 846–855, 1984.
- Heymsfield, A. J.: On measurements of small ice particles in clouds, *Geophys. Res. Lett.*, 34, 2007.
- Heymsfield, A. J. and Miloshevich, L. M.: Relative humidity and temperature influences on cirrus formation and evolution: Observations from wave clouds and FIRE II, *J. Atmos. Sci.*, 52, 4302–4326, 1995.
- Heymsfield, A. J., Bansemer, A., Field, P. R., Durden, S. L., Stith, J. L., Dye, J. E., Hall, W., and Grainger, C. A.: Observations and parameterizations of particle size distributions in deep tropical cirrus and stratiform precipitating clouds: Results from in situ observations in TRMM field campaigns, *J. Atmos. Sci.*, 59, 3457–3491, 2002.
- Hobbs, P. V.: Ice multiplication in clouds, *J. Atmos. Sci.*, 26, 1969.
- Hobbs, P. V. and Rangno, A. L.: Ice particle concentrations in clouds, *J. Atmos. Sci.*, 42, 2523–2549, 1985.
- Hoffer, T. E.: A laboratory investigation of droplet freezing, *J. Meteor.*, 18, 766–778, 1961.
- Holton, J. and Gettelman, A.: Horizontal transport and the dehydration of the stratosphere, *Geophys. Res. Lett.*, 28, 2799–2802, 2001.
- Hong, G., Yang, P., Gao, B. C., Baum, B. A., Hu, Y. X., King, M. D., and Platnick, S.: High cloud properties from three years of MODIS Terra and Aqua collection-4 data over the Tropics, *J. Appl. Meteor. Clim.*, 46, 1840–1856, 2007.

- Hu, Y. X., Wielicki, B., Lin, B., Gibson, G., Tsay, S. C., Stamnes, K., and Wong, T.: delta-Fit: A fast and accurate treatment of particle scattering phase functions with weighted singular-value decomposition least-squares fitting, *J. Quant. Spectrosc. Ra.*, 65, 681–690, 2000.
- Iaquinta, J., Isaka, H., and Personne, P.: Scattering phase functions of bullet rosette ice crystals, *J. Atmos. Sci.*, 52, 1402–1413, 1995.
- Jäkel, E., Wendisch, M., Kniffka, A., and Trautmann, T.: Airborne system for fast measurements of upwelling and downwelling spectral actinic flux densities, *Appl.Opt.*, 44, 434–444, 2005.
- Jensen, E. J., Kinne, S., and Toon, O. B.: Tropical Cirrus Cloud Radiative Forcing - Sensitivity Studies, *Geophys. Res. Lett.*, 21, 2023–2026, 1994.
- Jensen, E. J., Lawson, P., Baker, B., Pilson, B., Mo, Q., Heymsfield, A. J., Bansemmer, A., Bui, T. P., McGill, M., Hlavka, D., Heymsfield, G., Platnick, S., Arnold, G. T., and Tanelli, S.: On the importance of small ice crystals in tropical anvil cirrus, *Atmos. Chem. Phys.*, 9, 5519–5537, 2009.
- Jensen, E. and Smith, J., Pfister, L., Pitman, J., Weinstock, E., Sayres, D., Herman, R., Troy, R., Rosenlof, K., Thompson, T., Fridlind, A., Hudson, P., Cziczo, D., Heymsfield, A., Schmitt, C., and Wilson, J.: Ice supersaturations exceeding 100 implications for cirrus formation and dehydration, *Atmos. Chem. Phys. Discuss.*, 4, 7433–7462, 2004.
- Jin, Y., Rossow, W. B., and Wylie, D. P.: Comparison of the climatologies of high-level clouds from HIRS and ISCCP, *J. Climate*, 9, 2850–2879, 1996.
- Joseph, J. H., Wiscombe, W. J., and Weinman, J. A.: Delta-Eddington approximation for radiative flux-transfer, *J. Atmos. Sci.*, 33, 2.452–2.459, 1976.
- Kassianov, E. and Kogan, Y.: Spectral dependence of radiative horizontal transport in stratocumulus clouds and its effect on near-IR absorption, *J. Geophys. Res.*, 107, doi:10.1029/2002JD002103, 2002.
- Key, J. R., Yang, P., Baum, B. A., and Nasiri, S. L.: Parameterization of shortwave ice cloud optical properties for various particle habits, *J. Geophys. Res.*, 107, Art. No. 4181, 2002.
- King, M., Menzel, W., Grant, P., Myers, J., Arnold, G., Platnick, S., Gumley, L., Tsay, S.-C., Moeller, C., Fitzgerald, M., Brown, K., and Osterwisch, F.: Airborne scanning spectrometer for remote sensing of cloud, aerosol, water vapour, and surface properties, *J. Atmos. Oceanic Technol.*, 13, 777–794, 1996.
- King, M., Platnick, P., Hubanks, P., Arnold, G., Moody, E., Wind, G., and Wind, B.: Collection 005 Change Summary for the MODIS Cloud Optical Property Algorithm., http://modis-atmos.gsfc.nasa.gov/C005_Changes/C005_CloudOpticalProperties_ver311.pdf, 2006.

- King, M. D., Platnick, S., Yang, P., Arnold, G. T., Gray, M. A., Riedi, J. C., Ackerman, S. A., and Liou, K. N.: Remote sensing of liquid water and ice cloud optical thickness and effective radius in the Arctic: Application of airborne multispectral MAS data, *J. Atmos. Oceanic Technol.*, 21, 857–875, 2004.
- Kinne, S. and Liou, K. N.: The effects of the nonsphericity and size distribution of ice crystals on the radiative properties of cirrus clouds, *Atmos. Res.*, 24, 273–184, 1989.
- Klett, J. D.: Stable Analytical Inversion Solution For Processing Lidar Returns, *Appl. Opt.*, 20, 211–220, 1981.
- Klotzsche, S. and Macke, A.: Influence of crystal tilt on solar irradiance of cirrus clouds, *Appl. Opt.*, 45, 1034–1040, 2006.
- Knap, W., Hess, M., Stammes, P., and Koелеmeijer, R.: Cirrus optical thickness and crystal size retrieval from ATSR-2 data using phase functions of imperfect hexagonal ice crystals, *J. Geophys. Res.*, 104, 31 721–31 730, 1999.
- Koop, T., Luo, B. P., Tsias, A., and Peter, T.: Water activity as the determinant for homogeneous ice nucleation in aqueous solutions, *Nature*, 406, 611–614, 2000.
- Korolev, A. and Isaac, G.: Roundness and aspect ratio of particles in ice clouds, *J. Atmos. Sci.*, 60, 1795–1808, 2003.
- Korolev, A. and Isaac, G. A.: Shattering during sampling by OAPs and HVPS. Part I: Snow particles, *J. Atmos. Oceanic Technol.*, 22, 528–542, 2005.
- Korolev, A., Isaac, G. A., and Hallett, J.: Ice particle habits in stratiform clouds, *Quart. J. Roy. Meteor. Soc.*, 126, 2873–2902, 2000.
- Korolev, A. V., Isaac, G. A., and Hallett, J.: Ice particle habits in Arctic clouds, *Geophys. Res. Lett.*, 26, 1.299–1.302, 1999.
- Kristjansson, J., Edwards, J., and Mitchell, D.: Impact of a new scheme for optical properties of ice crystals on climate of two GCMs, *J. Geophys. Res.*, 105, 10 063–10 079, 2000.
- Kylling, A., Stammes, K., and Tsay, S.-C.: A reliable and efficient two-stream algorithm for spherical radiative transfer: documentation of accuracy in realistic layered media, *J. Atmos. Chem.*, 21, 115–150, 1995.
- Labonnote, L. C., Brogniez, G., Doutriaux-Boucher, M., Buriez, J. C., Gayet, J. F., and Chepfer, H.: Modeling of light scattering in cirrus clouds with inhomogeneous hexagonal monocrystals. Comparison with in-situ and ADEOS-POLDER measurements, *Geophys. Res. Lett.*, 27, 113–116, 2000.
- Lawson, R. P., Baker, B. A., Schmitt, C. G., and Jensen, T. L.: An overview of microphysical properties of Arctic clouds observed in May and July 1998 during FIRE ACE, *J. Geophys. Res.*, 106, 14.989–15.014, 2001.

- Lawson, R. P., Baker, B., Pilson, B., and Mo, Q. X.: In situ observations of the microphysical properties of wave, cirrus, and anvil clouds. Part II: Cirrus clouds, *J. Atmos. Sci.*, 63, 3186–3203, 2006.
- Li, L., Heymsfield, G., Racette, P., Tian, L., and Zenker, E.: A 94 GHz cloud radar system on a NASA high-altitude ER-2 aircraft, *J. Atmos. Ocean Technol.*, 21, 1378–1388, 2004.
- Liou, K.-N.: Influence of cirrus clouds on weather and climate processes: A global perspective, *Mon. Wea. Rev.*, 114, 1167–1199, 1986.
- Liu, C.-L. and Illingworth, A.: Toward more accurate retrievals of ice water content from radar measurements of clouds, *J. Appl. Meteorol.*, 39, 1130–1146, 2000.
- Lynch, D., Sassen, K., Starr, D., and Stephens, G., eds.: *Cirrus*, Oxford University Press, 2002.
- Mace, G. G., Benson, S., and Kato, S.: Cloud radiative forcing at the Atmospheric Radiation Measurement Program Climate Research Facility: 2. Vertical redistribution of radiant energy by clouds, *J. Geophys. Res.*, 111, doi:10.1029/2005JD005922, 2006a.
- Mace, G. G., Deng, M., Soden, B., and Zipser, E.: Association of tropical cirrus in the 10–15-km layer with deep convective sources: An observational study combining millimeter radar data and satellite-derived trajectories, *J. Atmos. Sci.*, 63, 480–503, 2006b.
- Macke, A.: Scattering of light by polyhedral ice crystals, *Appl. Opt.*, 32, 2780–2788, 1993.
- Macke, A. and Francis, P. N.: The role of ice particle shapes and size distributions in the single scattering properties of cirrus clouds, *J. Atmos. Sci.*, 55, 2.874–2.883, 1998.
- Macke, A., Mueller, J., and Raschke, E.: Single scattering properties of atmospheric ice crystals, *J. Atmos. Sci.*, 53, 2813–2825, 1996.
- Marshak, A., Davis, A., Wiscombe, W., and Cahalan, R.: Radiative smoothing in fractal clouds, *J. Geophys. Res.*, 100, 26 247–26 261, 1995.
- Marshak, A., Platnick, S., Varnai, T., Wen, G. Y., and Cahalan, R. F.: Impact of three-dimensional radiative effects on satellite retrievals of cloud droplet sizes, *J. Geophys. Res.*, 111, 2006.
- Mayer, B.: Radiative transfer in the cloudy atmosphere, *Eur. Phys. J. Conferences*, 1, 75–99, 2009.
- Mayer, B. and Kylling, A.: Technical note: The libRadtran software package for radiative transfer calculations - description and examples of use, *Atmos. Chem. Phys.*, 5, 1.855–1.877, 2005.
- McFarlane, S. A. and Marchand, R. T.: Analysis of ice crystal habits derived from MISR and MODIS observations over the ARM Southern Great Plains site, *J. Geophys. Res.*, 113, D07 209, 2008.

- McFarlane, S. A., Marchand, R. T., and Ackerman, T. P.: Retrieval of cloud phase and crystal habit from Multiangle Imaging Spectroradiometer (MISR) and Moderate Resolution Imaging Spectroradiometer (MODIS) data, *J. Geophys. Res.*, 110, Art. No. D14 201, 2005.
- McFarquhar, G. and Heymsfield, A.: Microphysical characteristics of three anvils sampled during the central equatorial pacific experiment, *J. Atmos. Sci.*, 53, 2401–2423, 1996.
- McFarquhar, G., Yang, P., Macke, A., and Baran, A.: A new parameterization of single scattering solar radiative properties for tropical anvils using observed ice crystal size and shape distributions, *J. Atmos. Sci.*, 59, 2458–2478, 2002.
- McFarquhar, G. M. and Heymsfield, A. J.: The definition and significance of an effective radius for ice clouds, *J. Atmos. Sci.*, 55, 2039–2052, 1998.
- McFarquhar, G. M., Um, J., Freer, M., Baumgardner, D., Kok, G. L., and Mace, G.: Importance of small ice crystals to cirrus properties: Observations from the Tropical Warm Pool International Cloud Experiment (TWP-ICE), *Geophys. Res. Lett.*, 34, 2007.
- Menzel, W. P., Smith, W. L., and Stewart, T. R.: Improved cloud motion wind vector and altitude assignment using Vas, *J. Climate Appl. Meteor.*, 22, 377–384, 1983.
- Menzel, W. P., Frey, R. A., Zhang, H., Wylie, D. P., Moeller, C. C., Holz, R. E., Maddux, B., Baum, B. A., Strabala, K. I., and Gumley, L. E.: MODIS global cloud-top pressure and amount estimation: Algorithm description and results, *J. Appl. Meteor. Clim.*, 47, 1175–1198, 2008.
- Meyers, M. P., DeMott, P. J., and Cotton, W. R.: New Primary Ice-Nucleation Parameterizations In An Explicit Cloud Model, *J. Appl. Meteor.*, 31, 708–721, 1992.
- Mie, G.: Beiträge zur Optik trüber Medien, speziell kolloidaler Metallösungen, *Annalen der Physik*, Vierte Folge, 25, 377–445, 1908.
- Mioche, G., Josset, D., Gayet, J.-F., Pelon, J., Garnier, A., Minikin, A., and Schwarzenboeck, A.: Validation of the CALIPSO/CALIOP extinction coefficients from in situ observations in mid-latitude cirrus clouds during CIRCLE-2 experiment, *J. Geophys. Res.*, submitted, 2009.
- Mitchell, D., Macke, A., and Liu, Y.: Modeling cirrus clouds. Part II: Treatment of radiative properties, *J. Atmos. Sci.*, 53, 2967–2988, 1996.
- Mitchell, D. L.: Effective diameter in radiation transfer: General definition, applications, and limitations, *J. Atmos. Sci.*, 59, 2330–2346, 2002.
- Nakajima, T. and King, M.: Determination of the optical thickness and effective particle radius of clouds from reflected solar radiation measurements. Part I: Theory, *J. Atmos. Sci.*, 47, 1878–1893, 1990.
- Nasiri, S. L., Baum, B. A., Heymsfield, A. J., Yang, P., Poellot, M. R., Kratz, D. P., and Hu, Y. X.: The development of midlatitude cirrus models for MODIS using FIRE-I, FIRE-II, and ARM in situ data, *J. Appl. Meteor.*, 41, 197–217, 2002.

- Oreopoulos, L., Cahalan, R. F., and Platnick, S.: The plane-parallel albedo bias of liquid clouds from MODIS observations, *J. Climate*, 20, 5114–5125, 2007.
- Ou, S., Liou, K., Gooch, W., and Takano, Y.: Remote sensing of cirrus cloud parameters using advanced very-high-resolution radiometer 3.7- and 10.9- μm channels, *Appl. Opt.*, 32, 2171–2180, 1993.
- Peter, T., Marcolli, C., Spichtinger, P., Corti, T., Baker, M. B., and Koop, T.: When dry air is too humid, *Science*, 314, 1399–1401, 2006.
- Petty, G.: *A First Course in Atmospheric Radiation*, 2nd Edition, Sundog Publishing, Madison, Wisconsin, 2006.
- Pierluissi, J. and Peng, G.-S.: New molecular transmission band models for LOWTRAN, *Optical Engineering*, 24, 541–547, 1985.
- Pilewskie, P., Pommier, J., Bergstrom, R., Gore, W., Howard, S., Rabbette, M., Schmid, B., Hobbs, P. V., and Tsay, S. C.: Solar spectral radiative forcing during the Southern African Regional Science Initiative, *J. Geophys. Res.*, 108, doi:10.1029/2002JD002411, 2003.
- Platnick, S.: Vertical photon transport in cloud remote sensing problems, *J. Geophys. Res.*, 105, 22 919–22 935, 2000.
- Platnick, S.: Approximations for horizontal photon transport in cloud remote sensing problems, *J. Quant. Spectrosc. Ra.*, 68, 75–99, 2001.
- Platnick, S., Li, J., King, M., Gerber, H., and Hobbs, P.: A solar reflectance method for retrieving the optical thickness and droplet size of liquid water clouds over snow and ice surfaces, *J. Geophys. Res.*, 106, 15 185–15 199, 2001.
- Platnick, S., King, M., Ackerman, S., Menzel, W., Baum, B., Riedi, J., and Frey, R.: The MODIS cloud products: Algorithms and examples from TERRA, *IEEE Trans. Geosci. Remote Sens.*, 41, 459–473, 2003.
- Potter, J.: The delta function approximation in radiative transfer theory, *J. Atmos. Sci.*, 27, 943–949, 1970.
- Pruppacher, H. R.: A new look at homogeneous ice nucleation in supercooled water drops, *J. Atmos. Sci.*, 52, 1924–1933, 1995.
- Redemann, J., Pilewskie, P., Russell, P. B., Livingston, J. M., Howard, S., Schmid, B., Pommier, J., Gore, W., Eilers, J., and Wendisch, M.: Airborne measurements of spectral direct aerosol radiative forcing in the Intercontinental chemical Transport Experiment/Intercontinental Transport and Chemical Transformation of anthropogenic pollution, 2004, *J. Geophys. Res.*, 111, 2006.
- Ricchiazzi, P., Yang, S., Gautier, C., and Sowle, D.: SBDART: A research and teaching software tool for plane-parallel radiative transfer in the Earth's atmosphere, *Bull. Amer. Meteorol. Soc.*, 79, 2101–2114, 1998.

- Rolland, P., Liou, K., King, M., Tsay, S., and McFarquhar, G.: Remote sensing of optical and microphysical properties of cirrus clouds using Moderate-Resolution Imaging Spectroradiometer channels: Methodology and sensitivity to physical assumptions, *J. Geophys. Res.*, 105, 11 721–11 738, 2000.
- Rosinski, J. and Morgan, G.: Cloud condensation nuclei as a source of ice-forming nuclei in clouds, *J. Atmos. Sci.*, 22, 123–133, 1991.
- Rossow, W., Walker, A., Beuschel, D., and Roiter, M.: International Satellite Cloud Climatology Project (ISCCP) - Documentation of new cloud datasets, Available at <http://isccp.giss.nasa.gov>, 1996.
- Rutledge, S. A. and Hobbs, P. V.: The mesoscale and microscale structure and organization of clouds and precipitation in mid-latitude cyclones: A model for the seeder-feeder process in warm-frontal rainbands, *J. Atmos. Sci.*, 40, 1185–1206, 1983.
- Sassen, K. and Wang, Z.: Classifying clouds around the globe with the CloudSat radar: 1-year of results, *Geophys. Res. Lett.*, 35, L04 805, 2008.
- Sassen, K., Wang, Z., and Liu, D.: Global distribution of cirrus clouds from CloudSat/Cloud-Aerosol Lidar and Infrared Pathfinder Satellite Observations (CALIPSO) measurements, *J. Geophys. Res.*, 113, 2008.
- Schaaf, C. B., Gao, F., Strahler, A. H., Lucht, W., Li, X. W., Tsang, T., Strugnell, N. C., Zhang, X. Y., Jin, Y. F., Muller, J. P., Lewis, P., Barnsley, M., Hobson, P., Disney, M., Roberts, G., Dunderdale, M., Doll, C., d'Entremont, R. P., Hu, B. X., Liang, S. L., Privette, J. L., and Roy, D.: First operational BRDF, albedo nadir reflectance products from MODIS, *Remote Sens. Environ.*, 83, 135–148, 2002.
- Schmetz, J., Holmlund, K., Hoffman, J., Strauss, B., Mason, B., Gaertner, V., Koch, A., and Vandeberg, L.: Operational Cloud-Motion Winds From Meteosat Infrared Images, *J. Appl. Meteor.*, 32, 1206–1225, 1993.
- Schmidt, K., Pilewskie, P., Mayer, B., Wendisch, M., Kindel, B., Platnick, S., King, M., Wind, G., Arnold, G., Tian, L., Heymsfield, G., and Eichler, H.: Apparent and real absorption of solar spectral irradiance in heterogeneous ice clouds, *J. Geophys. Res.*, submitted, 2009.
- Schmitt, C. G. and Heymsfield, A. J.: On the occurrence of hollow bullet rosette- and column-shaped ice crystals in midlatitude cirrus, *J. Atmos. Sci.*, 64, 4514–4519, 2007.
- Schumann, U.: Formation, properties and climatic effects of contrails, *C. R. Physique*, 6, 549–565, 2005.
- Shettle, E.: Models of aerosols, clouds and precipitation for atmospheric propagation studies, in *Atmospheric propagation in the uv, visible, ir and mm-region and related system aspects*, no. 454 in AGARD Conference Proceedings, 1989.
- Shupe, M. D. and Intrieri, J. M.: Cloud radiative forcing of the Arctic surface: The influence of cloud properties, surface albedo, and solar zenith angle, *J. Climate*, 17, 616–628, 2004.

- Stamnes, K., Hendriksen, K., and Ostensen, P.: Simultaneous measurement of UV radiation received by the biosphere and total ozone amount, *Geophys. Res. Lett.*, 15, 784–787, 1988a.
- Stamnes, K., Tsay, S., Wiscombe, W., and Jayaweera, K.: A numerically stable algorithm for discrete-ordinate-method radiative transfer in multiple scattering and emitting layered media, *Appl. Opt.*, 27, 2502–2509, 1988b.
- Stamnes, K., Tsay, S.-C., Wiscombe, W., and Laszlo, I.: DISORT, a General-Purpose Fortran Program for Discrete-Ordinate-Method Radiative Transfer in Scattering and Emitting Layered Media: Documentation of Methodology, Tech. rep., Dept. of Physics and Engineering Physics, Stevens Institute of Technology, Hoboken, NJ 07030, 2000.
- Stephens, G.: Radiation profiles in extended water clouds. II: Parameterization schemes, *J. Atmos. Sci.*, 35, 2123–2132, 1978.
- Stephens, G., Tsay, S.-C., Stackhouse Jr., P., and Flatau, P.: The relevance of the microphysical and radiative properties of cirrus clouds to climate and climatic feedback, *J. Atmos. Sci.*, 47, 1742–1753, 1990.
- Stephens, G., Vane, D., Boain, R., Mace, G., Sassen, K., Wang, Z., Illingworth, A., O’Connor, E., Rossow, W., Durden, S., Miller, S., Austin, R., Benedetti, A., Mitrescu, C., and the CloudSat Science Team: The CloudSat mission and the A-train, *Bull. Amer. Meteorol. Soc.*, 83, 1771–1790, 2002.
- Stephens, G. L. and Kummerow, C. D.: The remote sensing of clouds and precipitation from space: A review, *J. Atmos. Sci.*, 64, 3742–3765, 2007.
- Stephens, G. L. and Vane, D. G.: Cloud remote sensing from space in the era of the A-Train, *J. Appl. Rem. Sens.*, 1, 2007.
- Stubenrauch, C. and Schumann, U.: Impact of air traffic on cirrus coverage, *Geophys. Res. Lett.*, 32, doi:10.1029/2005GL022707, 2005.
- Stubenrauch, C., Rossow, W., Scott, N., and Chedin, A.: Clouds as seen by satellite sounders (3I) and imagers (ISCCP). Part III: Spatial heterogeneity and radiative effects, *J. Climate*, 12, 3419–3442, 1999.
- Stubenrauch, C. J., Chedin, A., Radel, G., Scott, N. A., and Serrar, S.: Cloud properties and their seasonal and diurnal variability from TOVS path-B, *J. Climate*, 19, 5531–5553, 2006.
- Takano, Y. and Liou, K.-N.: Solar radiative transfer in cirrus clouds. Part I: Single-scattering and optical properties of hexagonal ice crystals, *J. Atmos. Sci.*, 46, 1–19, 1989.
- Takano, Y. and Liou, K. N.: Radiative transfer in cirrus clouds. Part III. Light scattering by irregular ice crystals, *J. Atmos. Sci.*, 52, 818–837, 1995.
- Toon, O. B., Starr, D., Jensen, E., Newman, P., Platnick, S., Schoeberl, M. R., Wennberg, P. O., Wofsy, S., M.J., K., Maring, H., Jucks, K., Craig, M., M.F., V., Pfister, L., Rosenlof, K., Selkirk, H., Colarco, P., Kawa, S., Mace, G., Minnis, P., and Pickering, K.: Planning

- and Implementation of the Tropical Composition, Cloud and Climate Coupling Experiment (TC4), *J. Geophys. Res.*, submitted August, 2009.
- Twomey, S. and Seton, K. J.: Inferences of gross microphysical properties of clouds from spectral reflectance measurements, *J. Atmos. Sci.*, 37, 1065–1069, 1980.
- Vardiman, L.: Generation of secondary ice particles in clouds by crystal-crystal collision, *J. Atmos. Sci.*, 35, 2168–2180, 1978.
- Wegener, A.: *Thermodynamik der Atmosphäre*, J. A. Barth Verlag, 1911.
- Wendisch, M. and Mayer, B.: Vertical distribution of spectral solar irradiance in the cloudless sky: A case study, *Geophys. Res. Lett.*, 30, Art. No. 1183, 2003.
- Wendisch, M., Müller, D., Schell, D., and Heintzenberg, J.: An airborne spectral albedometer with active horizontal stabilization, *J. Atmos. Oceanic Technol.*, 18, 1856–1866, 2001.
- Wendisch, M., Pilewskie, P., Jäkel, E., Schmidt, S., Pommier, J., Howard, S., Jonsson, H. H., Guan, H., Schröder, M., and Mayer, B.: Airborne measurements of areal spectral surface albedo over different sea and land surfaces, *J. Geophys. Res.*, 109, Art. No. D08 203, 2004.
- Wendisch, M., Pilewskie, P., Pommier, J., Howard, S., Yang, P., Heymsfield, A. J., Schmitt, C. G., Baumgardner, D., and Mayer, B.: Impact of cirrus crystal shape on solar spectral irradiance: A case study for subtropical cirrus, *J. Geophys. Res.*, 110, Art. No. D03 202, 2005.
- Wendisch, M., Yang, P., and Pilewskie, P.: Effects of ice crystal habit on thermal infrared radiative properties and forcing of cirrus, *J. Geophys. Res.*, 112, D03 202, 2007.
- Wind, G., Platnick, S., King, M., Hubanks, P., Pavolonis, M., Heidinger, A., Baum, B., and Yang, P.: Multilayer cloud detection with the MODIS near-infrared water vapor absorption band., *J. Appl. Meteor. Climatology*, submitted in July, 2009.
- Winker, D. M. and Trepte, C. R.: Laminar cirrus observed near the tropical tropopause by LITE, *Geophys. Res. Lett.*, 25, 3351–3354, 1998.
- Wirth, M., Fix, A., Mahnke, P., Schwarzer, H., Schrandt, F., and Ehret, G.: The airborne multi-wavelength water vapor differential absorption lidar WALES: System design and performance, *Applied Physics B-Lasers And Optics*, 96, 201–213, 2009.
- Wiscombe, W.: The delta-M method: Rapid yet accurate radiative flux calculations for strongly asymmetric phase functions, *J. Atmos. Sci.*, 34, 1408–1421, 1977.
- Wylie, D., Menzel, W., Woolf, H., and Strabala, K.: Four years of global cirrus cloud statistics using HIRS, *J. Climate*, 7, 1972–1986, 1994.
- Wyser, K.: Ice crystal habits and solar radiation, *Tellus*, 51, 937–950, 1999.
- Yang, P. and Liou, K. N.: Geometric-optics-integral-equation method for light scattering by nonspherical ice crystals, *Appl. Opt.*, 35, 6.568–6.584, 1996.

- Yang, P., Liou, K. N., Wyser, K., and Mitchell, D.: Parameterization of the scattering and absorption properties of individual ice crystals, *J. Geophys. Res.*, 105, 4.699–4.718, 2000.
- Yang, P., Baum, B. A., Heymsfield, A. J., Hu, Y. X., Huang, H. L., Tsay, S. C., and Ackerman, S.: Single-scattering properties of droxtals, *J. Quant. Spectrosc. Ra.*, 79, 1159–1169, 2003.
- Yang, P., Wei, H. L., Huang, H. L., Baum, B. A., Hu, Y. X., Kattawar, G. W., Mishchenko, M. I., and Fu, Q.: Scattering and absorption property database for nonspherical ice particles in the near- through far-infrared spectral region, *Appl. Opt.*, 44, 5512–5523, 2005.
- Yang, P., Zhang, L., Hong, G., Nasiri, S. L., Baum, B. A., Huang, H. L., King, M. D., and Platnick, S.: Differences between collection 4 and 5 MODIS ice cloud optical/microphysical products and their impact on radiative forcing simulations, *IEEE Trans. Geosci. Remote Sens.*, 45, 2886–2899, 2007.
- Yang, P., Hong, G., Kattawar, G. W., Minnis, P., and Hu, Y. X.: Uncertainties associated with the surface texture of ice particles in satellite-based retrieval of cirrus clouds: Part II - Effect of particle surface roughness on retrieved cloud optical thickness and effective particle size, *IEEE Trans. Geosci. Remote Sens.*, 46, 1948–1957, 2008.
- Zhang, Y., Macke, A., and Albers, F.: Effect of crystal size spectrum and crystal shape on stratiform cirrus radiative forcing, *Atmos. Res.*, 52, 59–75, 1999.
- Zhang, Z., Yang, P., Kattawar, W., Tsay, S., Baum, B., Hu, J., Heymsfield, A., Reichardt, J. Zhang, Y., Rossow, W., Lacis, A., Oinas, V., and Mishchenko, M.: Geometrical-optics solution to light scattering by droxtal ice crystals, *Appl. Opt.*, 43, 2490–2499, 2004.
- Zinner, T. and Mayer, B.: Remote sensing of stratocumulus clouds: Uncertainty and biases due to inhomogeneity, *J. Geophys. Res.*, 111, doi:10.1029/2005JD006955, 2006.

List of Symbols

α	Ångstrom exponent	1
θ	Zenith angle	rad or $^{\circ}$
θ_0	Solar zenith angle	rad or $^{\circ}$
ϑ	Scattering angle	rad or $^{\circ}$
λ	Wavelength	nm or μm
μ	Cosine of the zenith angle θ	1
μ_0	Cosine of the solar zenith angle θ_0	1
σ	Standard deviation	1
τ	Cloud optical thickness	1
π	Circular constant 3.14159...	1
ρ	Albedo	1
ρ_{surf}	Surface albedo	1
ϱ_{ice}	Density of ice	g cm^{-3}
φ	Azimuth angle	rad or $^{\circ}$
φ_0	Solar azimuth angle	rad or $^{\circ}$
$\tilde{\omega}$	Single scattering albedo	1
$\tilde{\omega}'$	Delta-scaled single scattering albedo	1
$\langle \tilde{\omega} \rangle$	Volumetric single scattering albedo	1
Γ	Metric for 3D cloud structure effects on cirrus retrieval results	1
Δ	Opening angle of radiance optical inlet	rad or $^{\circ}$
Λ	Truncation order	1
Φ	Radiant energy flux	W
Ψ	Metric for crystal habit effects on cirrus retrieval results	1
$\vec{\Omega}$	Direction of propagation of radiation	sr
$d\Omega$	Solid angle	sr
b_{abs}	Volumetric absorption coefficient	m^{-1}
b_{ext}	Volumetric extinction coefficient	m^{-1}
b_n	Coefficients of the Legendre expansion of \mathcal{P}	1
b_{sca}	Volumetric scattering coefficient	m^{-1}
d_i	Instantaneous footprint diameter of radiance measurements	m
f	Fractional value between [0,1]	1
f_{tr}	Fraction of truncated energy	1
g	Asymmetry parameter	1
l	Distance between lamp and reflectance panel	cm

l_0	Certified distance to the reflectance panel	cm
n	Order of the Legendre polynomials and moments	1
\vec{n}	Surface orientation of dA	1
\tilde{n}_i	Imaginary part of the refractive index	1
r	Reflectance	1
r_P	Reflectance of the panel	1
r_c	Cloud top reflectance	1
z	Altitude	m
z_{top}	Cloud top altitude	m
z_{base}	Cloud base altitude	m
A	Particle cross section / mean projected area	m^2
dA	Unit surface	m^2
C_{abs}	Absorption cross section	m^2
C_{ext}	Extinction cross section	m^2
C_{sca}	Scattering cross section	m^2
D	Maximum particle dimension	μm
E_{rad}	Radiant energy	W s
F	Irradiance	W m^{-2}
F_{act}	Actinic flux density	W m^{-2}
F_{λ}	Spectral irradiance	$\text{W m}^{-2} \text{nm}^{-1}$
$F_{\lambda,L}$	Spectral irradiance of a lamp	$\text{W m}^{-2} \text{nm}^{-1}$
F^{\downarrow}	Downwelling irradiance	W m^{-2}
F^{\uparrow}	Upwelling irradiance	W m^{-2}
$F_{\text{diff}}^{\downarrow}$	Diffuse downwelling irradiance	W m^{-2}
$F_{\text{dir}}^{\downarrow}$	Direct downwelling irradiance	W m^{-2}
F_{λ}^{\downarrow}	Spectral downwelling irradiance	$\text{W m}^{-2} \text{nm}^{-1}$
F_{λ}^{\uparrow}	Spectral upwelling irradiance	$\text{W m}^{-2} \text{nm}^{-1}$
G	Digital spectrometer signal	1
G_{fld}	Digital spectrometer signal measured in the field	1
G_{lab}	Digital spectrometer signal measured in the laboratory	1
I	Radiance	$\text{W m}^{-2} \text{sr}^{-1}$
I_{λ}	Spectral radiance	$\text{W m}^{-2} \text{sr}^{-1} \text{nm}^{-1}$
$I_{\lambda,S}$	Spectral radiance of integrating sphere	$\text{W m}^{-2} \text{sr}^{-1} \text{nm}^{-1}$
I_{dir}	Direct radiance	$\text{W m}^{-2} \text{sr}^{-1}$
I_{diff}	Diffuse radiance	$\text{W m}^{-2} \text{sr}^{-1}$
I_{λ}^{\downarrow}	Spectral downwelling radiance	$\text{W m}^{-2} \text{sr}^{-1} \text{nm}^{-1}$
I_{λ}^{\uparrow}	Spectral upwelling radiance	$\text{W m}^{-2} \text{sr}^{-1} \text{nm}^{-1}$
$K_{\lambda,P}$	Calibration factor (Panel)	$\text{W m}^{-2} \text{sr}^{-1} \text{nm}^{-1}$
$K_{\lambda,S}$	Calibration factor (Sphere)	$\text{W m}^{-2} \text{sr}^{-1} \text{nm}^{-1}$
K_T	Transfer calibration factor	1
$\frac{dN}{dD}$	Particle number size distribution	$\text{l}^{-1} \mu\text{m}^{-1}$
P_n	Legendre polynomials	1
R_{eff}	Ice Crystal / Particle effective radius	μm

S_0	Extraterrestrial solar irradiance	W m^{-2}
T_{int}	Integration time of a spectrometer scan	ms
V	Particle Volume	m^3
Z	Radar reflectivity	dBZ
ΔF	Radiative forcing	W m^2
ΔF^{IR}	Thermal IR radiative forcing	W m^2
ΔF^{net}	Net radiative forcing	W m^2
ΔF^{sol}	Solar radiative forcing	W m^2
\mathcal{P}	Scattering phase function	1
$\mathcal{P}_{d\text{HG}}$	Double Henyey-Greenstein scattering phase function	1
\mathcal{P}_{HG}	Henyey-Greenstein scattering phase function	1
$\langle \mathcal{P} \rangle$	Volumetric scattering phase function	1
$S\Delta F^{\text{sol}}$	Solar radiative forcing efficiency	W m^2
$FWHM$	Full Width at Half Maximum	nm
IWC	Ice Water Content	mg l^{-1}
IWP	Ice Water Path	g m^{-2}
LWC	Liquid Water Content	mg l^{-1}

List of Abbreviations

1D	one-dimensional
2D	two-dimensional
3D	three-dimensional
AIRTOSS	AIRcraft Towed Sensor Shuttle
ARM	Radiation Measurement Program Southern Great Plains (SGP)
ATC	Air Traffic Control
BOA	Bottom-Of-Atmosphere
CALIPSO	Cloud-Aerosol Lidar and Infrared Pathfinder Satellite Observation satellite
CIP	Cloud Imaging Probe
CIRCLE-2	CIRrus CLOUD Experiment-2
CCD	Charged-Coupled Device
CPI	Cloud Particle Imager
CRYSTAL-FACE	Cirrus Regional Study of Tropical Anvils and Cirrus Layers - Florida Area Cirrus Experiment
CRS	Cloud Radar System
DISORT	Discrete Ordinate Radiative Transfer solver
DFG	Deutsche Forschungsgemeinschaft (German Research Foundation)
DLR	Deutsches Zentrum für Luft- und Raumfahrt (German Aerospace Center)
DU	Dobson Unit
EM	electromagnetic
FIRE	First ISCCP Regional Experiment
FSSP	Forward Scattering Spectrometer Probe
GCM	Global Climate Model
GOES	Geostationary Operational Environmental Satellite
GPS	Global Positioning System
HG	Henry-Greenstein
ICP	Ice Crystal Parameterization
IfT	Leibniz-Institute for Tropospheric Research
INS	Inertial Navigation System
IPA	Independent Pixel Approximation
IR	Thermal Infrared wavelength range (here, 5–100 μm)
ISCCP	International Satellite Cloud Climatology Project
ITCZ	Intertropical Convergence Zone
LaMP	Laboratoire de Météorologie Physique

lidar	Light detection and ranging
<i>libRadtran</i>	Library for Radiative transfer
LUT	Lookup table
MAS	MODIS Airborne Simulator
MISR	MultianglE Imaging Spectroradiometer
MODIS	Moderate Resolution Imaging Spectroradiometer
MSG	Meteosat Second Generation
MYSTIC	Monte Carlo code for the physically correct tracing of photons in cloudy atmospheres
NASA	National Aeronautics and Space Administration
NIST	National Institute of Standards and Technology
NIR	Near InfraRed wavelength range (here, 700–3000 nm)
NIR	Spectrometer covering the wavelength range 900–2200 nm
OMI	Ozone Measurement Instrument
PC	Personal Computer
PDA	Photo-Diode Array
PGS	Plane Grating Spectrometer
radar	Radio detection and ranging
RTE	Radiative Transfer Equation
SGP	Southern Great Plains
SMART	Spectral Modular Airborne Radiation measurement system
SPARM	Stabilized Platform for Airborne Radiation Measurements
SSFR	Solar Spectral Flux Radiometer
TC ⁴	Tropical Composition, Cloud, and Climate Coupling experiment
TOA	Top-Of-Atmosphere
UTC	Universal Time Coordinated
UV	Ultra Violet wavelength range (here, 100–380 nm)
VIS	Visible wavelength range (here, 380–700 nm)
VIS	Spectrometer covering the wavelength range 390–1000 nm
WMO	World Meteorological Organisation

List of Figures

1.1	Heterogeneous freezing processes	2
1.2	Vertical profile of ice particle size and shape	4
2.1	Geometry to define radiance and irradiance	11
2.2	Imaginary part of refractive index of ice and single-scattering albedo	15
2.3	Scattering phase function of single ice crystals	16
3.1	SMART-Albedometer Setup during CIRCLE-2	23
3.2	Footprint of radiance optical inlet	24
3.3	Radiance calibration setup.	25
3.4	Calibration factors radiance measurements	26
3.5	Transfer calibration factors CIRCLE-2	27
3.6	Instrumentation of the German Falcon aircraft	29
3.7	Flight track on May 22, 2007	32
3.8	Lidar profile of probed cirrus on May 22, 2007	33
3.9	Photos of cirrus and land surface 22 May, 2007	34
3.10	Time series of I_{λ}^{\uparrow} on May 22, 2007	34
4.1	Spectral surface albedos	38
4.2	Measured and modelled clear sky upwelling radiance spectra	39
4.3	Ice crystal habits	40
4.4	Cloud top reflectance versus τ and R_{eff}	42
4.5	Schematic of cirrus retrieval method	42
4.6	Cloud retrieval solution space for P1	44
4.7	Cloud retrieval solution space for P2	44
4.8	Measured and modelled cloud top reflectance versus wavelength	45
5.1	Time series of retrieved τ and R_{eff} for P1 and P2	48
5.2	CPI images in uppermost in-cloud leg	49
5.3	Occurrence of crystal shapes	50
5.4	Spectral solar radiative forcing	54
5.5	Diurnal variation of ΔF^{sol}	56
5.6	Broadband solar radiative forcing	57
5.7	Diurnal variation of $S\Delta F^{\text{sol}}$ versus SZA	58
5.8	Spectral IR radiative forcing	60
5.9	Broadband net radiative forcing	62
6.1	Satellite Image of TC ⁴ cloud	66

6.2	TC ⁴ 3D input cloud	68
6.3	Schematic of Methodology applied in Section 6	70
6.4	Cloud retrieval solution space for the TC ⁴ case study	73
6.5	Time series of TC ⁴ input cloud τ and R_{eff} with retrieved values	76
6.6	Retrieved cirrus properties versus TC ⁴ input cloud values	77
6.7	Modelled r^{IPA} versus τ^{inp}	79
6.8	Ratio of modelled r^{IPA}	80
6.9	(a) Retrieved τ^{IPA} versus τ^{inp} and (b) $R_{\text{eff}}^{\text{IPA}}$ versus $R_{\text{eff}}^{\text{inp}}$	80
6.10	Time series of TC ⁴ retrieved τ and R_{eff} under different shape assumptions . .	81
6.11	Dependence of Γ and Ψ on different parameters	83
7.1	Tandem platform for cloud-radiation interaction studies	91

List of Tables

3.1	Spectrometer Characteristics	22
3.2	Uncertainties of radiance measurements.	28
3.3	Measurement flights CIRCLE-2	30
4.1	Particle habit mix	40
4.2	Notations for particle habits.	41
4.3	CIRCLE-2 case studies input to <i>libRadtran</i>	43
5.1	Uncertainties of retrieved τ and R_{eff}	46
5.2	Retrieved τ and R_{eff} for flight 22 May, 2007, P1	47
5.3	Retrieved τ and R_{eff} for flight 22 May, 2007, P2	47
5.4	Influence of wavelengths used in the retrieval	52
5.5	Broadband solar radiative forcing	55
5.6	Solar radiative forcing efficiencies	58
5.7	Broadband thermal IR radiative forcing	61
5.8	Broadband net radiative forcing	63
6.1	TC ⁴ input to <i>libRadtran</i>	72
6.2	Uncertainties of the TC ⁴ cirrus retrieval results	75
6.3	g and $\tilde{\omega}$ for different ice crystal habits	78
6.4	Retrieved τ and R_{eff} for the TC ⁴ case study	81

Curriculum vitae

Name Heike Kalesse, geb. Eichler
Date of birth 8 September, 1979
Place of birth Mühlhausen, Thüringen
Citizenship German
Current address Borkholderstr. 5
65203 Wiesbaden, Germany
Email: heike979 (at) web.de

Education

05/2006–04/2010 PhD student at the Johannes Gutenberg University, Mainz, Germany
03/2006 Graduation: Meteorology diploma with the overall grade
“passed with distinction” (1.0)
03/2005–03/2006 Diploma thesis *“Hygroscopic Behaviour and Simulation
of the Aerosol Extinction in South East China at Ambient Conditions”*
at Leibniz-Institute for Tropospheric Research (IfT), Leipzig
10/2000–03/2006 Student of meteorology at the University of Leipzig
08/1999–06/2000 Student at the College of Lake County, Grayslake, IL, USA
06/1999 High-school degree (“Abitur”) at a merit of 1.3
07/1997–08/1997 Pre-college summer school student (astronomy)
at the Johns Hopkins University, Baltimore, MD, USA
09/1992–06/1999 High school “Erwin-Strittmatter Gymnasium”, Spremberg, Germany
09/1986–06/1992 Primary school “Karl-Liebknecht OS”, Spremberg

Employments

05/2006–04/2010 Scientific employee at the Johannes Gutenberg University, Mainz
04/2006–09/2006 Scientific employee at the IfT, Leipzig
04/2003–03/2006 Student research assistant of Dr. B. Wehnert, IfT, Leipzig